Dist: A

REPORT DOCUMENTATION PAGE

Form Approved
OMB No. 0704-0188

1. AGENCY USE ONLY (Leave blank)	2. REPORT DATE	3. REPORT TYPE AND DATES COVERED
	2/8/95	Final Report 6/15/94 - 12/15/94

4. TITLE AND SUBTITLE
Electrochemical Impedance Pattern Recognition for Detection of Hidden Chemical Corrosion on Aircraft Components

5. FUNDING NUMBERS
Air Force SBIR Phase I
F49620-94-C-0043
3005/SS
65502F

6. AUTHOR(S)
A.F. Sammells and J.S. Bowers

7. PERFORMING ORGANIZATION NAME(S) AND ADDRESS(ES)
Eltron Research, Inc.
2830 Wilderness Place
Boulder, CO 80301

8. PERFORMING ORGANIZATION REPORT NUMBER
Final Report
Project 067
AFOSR-TR-95-0106

9. SPONSORING/MONITORING AGENCY NAME(S) AND ADDRESS(ES)
USAF Code FA9550
Air Force Office of Scientific Research/NC
110 Duncan Avenue, Suite B115
Bolling AFB, DC 20332-0001
Maj Erstfeld

10. SPONSORING/MONITORING AGENCY REPORT NUMBER
0002AA

11. SUPPLEMENTARY NOTES

12a. DISTRIBUTION/AVAILABILITY STATEMENT
Unlimited Distribution

12b. DISTRIBUTION CODE
A

13. ABSTRACT *(Maximum 200 words)*

This investigation addressed the need for diagnostic instrumentation compatible with performing the Nondestructive Evaluation (NDE) of hidden chemical corrosion with a high degree of accuracy, sensitivity and versatility on both titanium and aluminum alloys currently used in Air Force and commercial aircraft. The overall approach was directed towards development of pattern recognition schemes based upon the on-line data acquisition of Fast Fourier Transform Electrochemical Impedance Spectroscopy (FFTEIS) instrumentation from the suspect hidden chemical corrosion site. Resulting impedance patterns were then analyzed by application of a Neural Network pattern recognition scheme. The Neural Network Analysis (NNA) was then trained to both detect and grade the severity of hidden corrosion present on the aircraft metal substrate interface of interest. Neural Net Analysis of FFTEIS data was verified as a powerful diagnostic strategy for *in situ* hidden corrosion process identification, quantitative analysis and severity grading. Correlations between impedance measurements and corrosion depth were verified by subsequent SEM and EDX examination of the metal interfacial regions. The approach will also be powerful for gaining fundamental information into the nature of corrosion processes and conditions leading to their inception at hidden sites.

14. SUBJECT TERMS	15. NUMBER OF PAGES
Hidden Chemical Corrosion, Neural Networks, Detection, Electrochemical Impedance	87
	16. PRICE CODE

17. SECURITY CLASSIFICATION OF REPORT	18. SECURITY CLASSIFICATION OF THIS PAGE	19. SECURITY CLASSIFICATION OF ABSTRACT	20. LIMITATION OF ABSTRACT
Unclassified	Unclassified	Unclassified	None

TABLE OF CONTENTS

LIST OF FIGURES

APPENDIX - LIST OF FIGURES

I. INTRODUCTION

A. Program Background

This Phase I research and development effort addressed the need for diagnostic instrumentation compatible with performing the Nondestructive Evaluation (NDE) of hidden chemical corrosion with a high degree of accuracy, sensitivity and versatility on both titanium and aluminum alloys currently used in Air Force and commercial aircraft. The overall approach is directed towards development of pattern recognition schemes based upon the on-line data acquisition of Fast Fourier Transform Electrochemical Impedance Spectroscopy (FFTEIS) instrumentation from the suspect hidden chemical corrosion site. Resulting impedance patterns are then analyzed by application of a Neural Network pattern recognition scheme. The Neural Network Analysis (NNA) was then trained to both detect and grade the severity of hidden corrosion present on the aircraft metal substrate interface of interest. Work performed has demonstrated that this instrumentation approach can be handled by portable computer driven hardware and software, for the on-line determination of hidden corrosion processes on-site, for a given aircraft component. The approach will also be compatible with gaining fundamental information into the nature of corrosion processes and conditions leading to their inception at hidden sites. A schematic of how this instrumentation technology would be implemented for the detection of hidden corrosion on in-service aircraft components is shown in Figure 1.

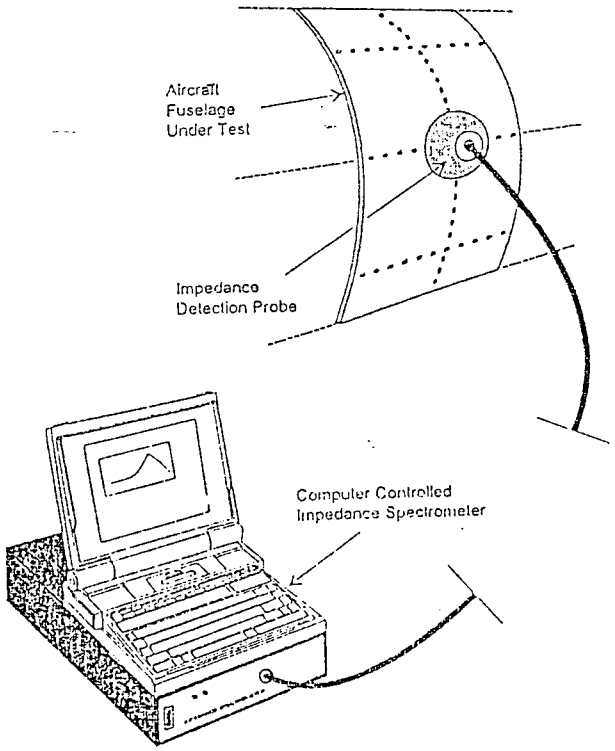

Figure 1. Schematic of instrumentation strategy being developed in this program for the Non-Destructive Evaluation of hidden corrosion on aircraft components.

Emphasis during Phase I was placed upon detecting hidden corrosion processes on the titanium alloy Ti 15-3 (15% V, 3% Cr, 3% Al, 3% Sn, balance Ti), commonly used as aircraft fuselage and wing box coverings, and the respective aluminum alloys 2024 (4.5% Cu, 1.5% Mg, 0.6% Mn, balance Al) and 7075 (5.6% Zn, 2.5% Mg, 1.6% Cu, 0.3% Cu, balance Al), frequently used as aircraft structural components. The detection of hidden corrosion associated with interface between titanium and aluminum alloys, as may occur at aircraft fastener regions, was emphasized in this program.

Since all corrosion phenomena are electrochemical in nature it was recognized in this approach that the most effective instrumentation strategy for achieving accurate detection of hidden chemical corrosion would be by definition electrochemically based. However, most previous work has applied only conventional electrochemical techniques to the detection or analysis to corrosion phenomenon at metal substrates. During such studies substrates under test have been frequently subjected to either voltage (potentiostatic) or current (galvanstatic) control which in many cases can result in producing a large perturbation in surface corrosion conditions under examination. Since application of such techniques frequently result in producing an irreversible change in surface corrosion conditions, inaccurate conclusions can frequently be drawn as to the original state of surface corrosion. As a consequence techniques which rely upon large induced signal perturbations can only be used to gain qualitative, rather than quantitative, insight into the nature of a hidden corrosion site.

In comparison Electrochemical Impedance Spectroscopy (EIS) techniques only require application of a small signal perturbation to the corrosion site under investigation so that all information correlating to that region can be retrieved for later analysis. Previous EIS measurements on stainless steels, titanium and aluminum alloys have demonstrated impedance elements having distinct RC time constants associated with corrosion related phenomenon.[1-4] Such corrosion processes analyzed by impedance measurements can be modeled using equivalent circuits of resistive, capacitive and inductive elements in either series or parallel configurations. For EIS measurements, where a series equivalent circuit represents the total (many site) corrosion process, a linear equation can be generated by summation of individual impedance components,[5] via for example:

$$Z(\textit{total circuit}) = Z1 + Z2 + Z3 + Z4 + \ldots \quad (1)$$

It is recognition of this fact which directed our attention during Phase I to apply NNA for transforming experimental impedance data into a form which can distinguish both the nature and severity of hidden chemical corrosion present on a given metal substrate.

During EIS measurements a small sinusoidal potential is applied to a working electrode substrate, where a hidden corrosion site may be present, over a wide range of frequencies and the resulting sinusoidal current phase shift measured. However one limitation of the EIS approach is that for acquisition of a complete impedance spectrum, large frequency ranges (10^6 Hz to 10^{-1} Hz) must usually be measured. This is often time consuming. Such an experimental protocol can be problematic when the system property under measurement changes with time, such as at a hidden corrosion site. An alternative EIS measurement strategy, which was adopted during performance of this program is to simultaneously perturb the suspect corrosion site with a large number of frequencies and subsequently measure impedance-time behavior.[6] Application of a Fourier transform is then used to

convert data obtained from the time domain to the frequency domain for subsequent analysis.[7-13] This technique has previously been applied to measurements performed at dropping mercury electrodes known as Fourier Transform Faradaic Admittance[14-18] where admittance corresponded to the reciprocal of impedance.

The EIS method like most small-amplitude time dependent measurement techniques is based upon defining the relationship between applied excitation[14] i.e. the time varying applied voltage V(t)) and the resulting time dependent system response (i.e. the time varying current I(t)). For excitation with voltages of sufficiently small amplitudes the relationship between the two time dependent parameters V(t), I(t) may be given by the general form of Ohms law:[5]

$$V(t) = Z(t)I(t) \tag{2}$$

where Z(t) is the measured time dependent impedance of the system under test.

Normally system impedance may be expressed in the frequency (f) domain by:

$$V(f) = Z(f)I(f) \tag{3}$$

Conversion between these two different representations may be easily accomplished by use of the respective Fourier transforms:

$$Z(f) = \int_{-\infty}^{\infty} Z(t) e^{2\pi i f t} dt \tag{4}$$

and

$$Z(t) = \int_{-\infty}^{\infty} Z(f) e^{-2\pi i f t} df \tag{5}$$

A subset of the general Fourier transform is known as Fast Fourier transform, whose major feature lies in processing speed. For example, with a data set of 10^6 data points the difference in speed between general Fourier transform and Fast Fourier transform is about a factor of 40,000. The Cooley-Tukey FFT algorithm is the approach used most often in the FFT technique.[19] Use of this algorithm however requires that the initial data array be in a mathematically acceptable form. The Cooley-Tukey FFT algorithm can only transform a discrete finite data record of time domain signals to a discrete finite data record of frequencies. The data record to be transformed must contain 2^n points. This requirement for FFT can be accommodated experimentally by adjusting either the data sampling rate or the data acquisition period.[20] These adjustable experimental parameters determined frequency domain spectra properties following the transform of time domain data. Here the reciprocal of the acquisition period was equal to the lowest frequency and determined signal resolution.

For example using a 0.1 sec data acquisition rate the lowest frequency available was 10 Hz with resolution being limited to this frequency. Sampling rate also determined the number of points in the frequency (or time) domain. Sampling theorems dictate that the highest frequency that can be completely characterized in terms of magnitude and phase are less than $\approx 1/2$ the sampling rate. Thus for acquisition of a 1024 point data array the highest frequency component measurable was less than (1024/2)*10 Hz or 5120Hz. Relatively wide bandwidth frequency domains could be sampled during Phase I using current electronics technology which permitted characterization of EIS data.

As discussed previously, the total impedance of a series-circuit may be given by the linear combination of individual impedances[5] as follows:

$$Z_{Total}=\sum_{i=1}^{n} Z_i \qquad (6)$$

This behavior permitted application of NNA to Fast Fourier transform impedance data matrices during performance of Phase I for subsequent pattern recognition on respective aircraft metal alloy interface subjected to specific corrosion environments. NNA used during Phase I was a form of Artificial Intelligence (AI) that trained computer software to recognize patterns which identified and determined the severity of hidden chemical corrosion at metal interfacial sites. The general approach was a first approximation at simulating pattern recognition processes that occur in the brain. This technology was used during Phase I for transferring abstract data (phase angles from electrochemical impedance data) into recognizable patterns corresponding to the detection of a real event i.e. for determining the presence and severity of corrosion on titanium and aluminum alloys and solid state interface between these materials.

The NNA system used during Phase I for EIS analysis consisted of 300 interconnected processing nodes operating in parallel and possessing several layers. The Neural Network used an input layer of nodes corresponding to electrochemical impedance data points. The corresponding output layer was trained to recognize the nature of surface corrosion effects and their degree of severity. Each nodal layer was connected into the next by a mathematic transformation corresponding to an iterated weight.

The Neural Network corrosion pattern recognition scheme was taught using a series of experimentally determined electrochemical impedance inputs corresponding to conditions where corrosion was present at a specific alloy interface. This permitted mathematical weights to be applied relating to the nature and severity of corrosion present, and this was performed using an algorithm called Probablistic Neural Net Architecture[21,22] which used two passes through the network for each mathematical iteration. In the first pass experimental data inputs proceeded through the network to generate an appropriate output. The difference between this output and the desired output corresponded to the error signal modified network weighting. The excitation source used in FFTEIS experiments was a pseudo-white noise signal consisting of discrete sine waves having a constant amplitude over a defined frequency range. Optimum frequency ranges were identified during Phase I for this excitation source and corresponded to between 10kHz and 0.01Hz.

After digital pseudo-white noise signal generation, the microcomputer loaded this signal into Static Random Access Memory (SRAM) chips. This memory was accessed directly by the Digital-to-Analog Converter (D/A) to increase processing speed, following which the pseudo-white noise signal was applied to the aircraft component corrosion sample under investigation. The resulting time dependent current was acquired by an Analog-to-Digital Converter (ADC) and subsequently stored in memory. To ensure that the experimental impedance data possessed acceptable signal-to-noise ratios, signal averaging was also used. The optimum amount of signal averaging necessary to obtain high signal-to-noise ratios with a minimum of data points was determined experimentally.

The averaged signal, containing impedance information relating to the corrosion process in the time domain, was processed by FFT conversion to obtain speed advantages inherent with such an approach. Following FFT conversion, the resulting frequency

domain impedance spectra from the chemical corrosion site was stored on a hard disk for later analysis by the Neural Network.

Performance of this program resulted in clarifying the principles behind this technology for eventual development during Phase II and III as field usable portable instrumentation compatible with achieving the nondestructive real-time, *in situ* detection of hidden chemical corrosion sites on aircraft components.

B. Comparison of FFTEIS with other Techniques for NDE Hidden Corrosion Detection

FFTEIS techniques are particularly appropriate for detecting and measuring hidden corrosion because, as discussed earlier, electrochemical methodologies best characterize such electrochemical corrosion processes. Furthermore this technology will facilitate obtaining fundamental information into the nature of corrosion at such hidden sites. Alternative corrosion flaw detection techniques currently being evaluated depend upon a buildup of remnant byproducts at hidden corrosion sites. For example, corrosion product volume is typically three times greater than for an original aluminum substrate. Present NDE techniques use resultant surface pillowing effects for detecting reduced metal thickness symptomatic of corrosion. Such alternative approaches include optical techniques such as electronic speckle pattern,[23] optical interferometry[24,25] and computer enhanced visual inspection.[26] These techniques detect outer metal surface distortions resulting from corrosion byproduct buildup within the structure. Skin thickness can however impose fundamental measurement limitations. Tensile metal deformation properties can diminish detectable outer surface topology changes. Also corrosion at stringer/bottom skin metal-to-metal interfaces, for single layers may be undetectable from the outer skin surface. Multiple layers resulting from doublers require corrosion to sequentially deform subsequent layers.

A second group of techniques currently being evaluated for NDE corrosion detection includes thermal wave imaging[27] and X-ray backscatter[28,29] which have many critical factors in common with ultrasonic,[30-33] scanning magnetometer,[34] and magnetic eddy current methods.[35,36] Each of these techniques determines the remaining metal thickness by signal analysis of the returned illumination from hidden corrosion thinned locations. Signal analysis determines corrosion related changes in substrate density or signal reflections from the metal/corrosion byproduct interface. Corrosion products will modify returned signals in ways which give insight into corrosion chemistry. Multiple layer structures however will pose technical problems for each technique. Except for X-ray backscattering, metal-to-metal interface can cause artificial signal reflections, thereby increasing analysis complexity and the possibility of inaccurate detection for hidden corrosion sites.

X-ray backscattering[28] will detect through fluorescence, only those corrosion product constituents not present in the original alloy. X-ray illumination of metal substrates can also be a safety hazard. However high X-ray intensities in this technique are required for two reasons. The first is a consequence of light elements involved in the corrosion process being only weakly excited by this radiation source. Resultant fluorescent X-rays have low energy thereby reducing the metal thickness which can be penetrated prior to absorption at the corrosion site. Corrosion at the stringer in multiple layer structures will require high

levels of fluorescent X-rays for detection of hidden corrosion. Secondly, emitted X-rays are radiated equally in all directions. Only those which reach the detector i.e. 1% of those emitted, can be analyzed to determine the presence and degree of hidden corrosion.

Identification of hidden corrosion related density changes by X-ray backscattering[29] will be less detectable because of decreased substrate density. This technique is based upon measuring a signal below background. The reduced return signal will consequently require extensive processing due to responses varying as a function of substrate thickness.

In comparison to the above approaches corrosion product constituents will only have a minor effect upon the reliability of FFTEIS based hidden corrosion detection. This measurement technique will be able to examine metal substrate structures from the edge of interfacial lap joints rather than from the top surface. The non-corroding FFTEIS probe solution required in instrumentation technology being developed in this program will reach the corrosion site via surface tension forces. As a consequence all corrosion sites will simultaneously respond to the impedance probe signal thereby providing a total measured response for the corrosion region being investigated. This approach will permit corrosion severity to be determined without limitation to site location in multiple layer structures. This will unambiguously detect hidden corrosion and avoid the above discussed disadvantages present with alternative techniques.

As will become evident in the next section, work performed during Phase I resulted in clarifying the utility of the originally proposed instrumentation technology for hidden corrosion detection. Commercial application during Phase II and III will result in portable field instrumentation compatible with achieving the nondestructive real-time, *in situ* detection of hidden chemical corrosion sites on both Air Force and FAA aircraft components.

II. PHASE I TECHNICAL OBJECTIVES

The overall objective of this program was to determine the feasibility of instrumentation compatible with detecting in real-time the presence of hidden chemical corrosion on selected metal aircraft components and grade their degree of severity. As will become evident this resulted in the identification of instrumentation compatible for commercialization during Phase II and III.

Specific program objectives addressed during Phase I to develop this technology was as follows:

- Identified preferred components incorporated into the subject FFTEIS instrument for detection of hidden chemical corrosion. This permitted electrochemical impedance measurements to be performed over the desired range of instrumentation parameters.

- Performed systematic electrochemical impedance measurements as a function of time on selected metal substrates, representative of metal aircraft component interface, which had been previously subjected to simulated atmospheric corrosion conditions.

- A Neural Network was trained to both detect and grade the severity of hidden chemical corrosion using introduced FFTEIS data.

- Fabricated prototype instrumentation, including both hardware and software, for achieving the *in situ* detection of hidden chemical corrosion.

III. WORK PERFORMED AND RESULTS OBTAINED

The overall objective of work performed during Phase I was to identify preferred hardware and software components compatible with determining the viability of instrumentation for unambiguously detecting both the presence and severity of hidden chemical corrosion in aircraft components. The detection strategy was based upon the experimental determination of impedance data obtained using Fast Fourier Transform Electrochemical Impedance Spectroscopy (FFTEIS) instrumentation. Resulting impedance data was subsequently analyzed by Neural Network based pattern recognition techniques for determining the presence and severity of hidden chemical corrosion.

Experimental work performed during Phase I initially obtained representative electrochemical impedance spectra from metal substrates subjected to systematically selected corrosion conditions. Impedance spectra obtained from intentionally corroded titanium and aluminum alloys together with their solid state interface were used to train a Neural Network to both detect and determine the severity of hidden corrosion.

The Phase I experimental program was performed by completing the following four tasks.

Task 1 Fabrication of Laboratory FFTEIS Instrumentation Incorporating Preferred Components

Task 2 Perform FFTEIS Measurements on Relevant Metal Substrates Subjected to Hidden Chemical Corrosion

Task 3 Develop and Train Neural Networks for Unambiguously Detecting and Determining the Severity of Hidden Chemical Corrosion on Metal Substrates

Task 4 Fabrication and Performance Testing of Prototype Instrumentation

Specific work performed during Phase I each task will now be discussed.

Task 1 Fabrication of Laboratory FFTEIS Instrumentation Incorporating Preferred Components

The objective of this task was to select and fabricate hardware necessary for developing Fast Fourier Transform Electrochemical Impedance Spectroscopy (FFTEIS) instrumentation. Figure 2 shows a schematic block diagram of instrumentation fabricated during this task illustrating essential components used for both probing the hidden corrosion site of interest, and for retrieving and analyzing the resulting impedance signal. Features incorporated into individual components, developed during Phase I, are described in the following subtasks.

a) Generation of Pseudo-White Noise Signal during Phase I as an Excitation Source for Impedance Measurements at Hidden Corrosion Sites

A computer generated pseudo-white noise excitation source was used for the

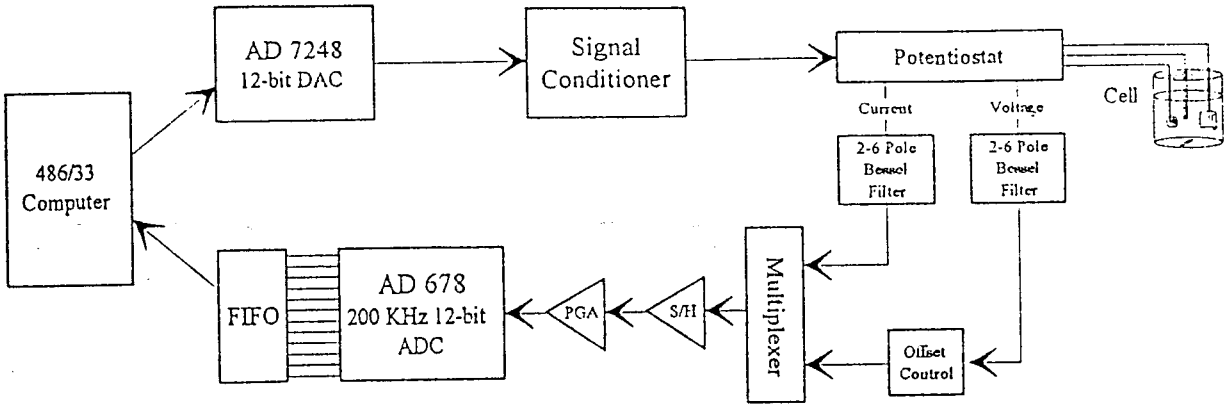

Figure 2. Block diagram of components incorporated into Fast Fourier Transform Electrochemical Impedance Spectrometer fabricated and performance tested during this Phase I program.

instrumentation system under evaluation. A combined software and hardware approach was used to achieve this goal. This was performed by initially writing a program in a high level language (Pascal) for signal generation. A 2K memory array for adding individual discrete sine waves was created. These possessed the form:[6,10,11,14]

$$\sin(2\pi ft + \phi) \tag{7}$$

where f was the signal frequency, t was time, and ϕ corresponded to a random phase number needed to produce the pseudo-white noise which was subsequently stored in a temporary file. This file was used to apply the pseudo-white noise to the D/A circuit and then to the electrochemical impedance cell. Identification of the optimum signal frequency range necessary for these measurements depended upon the simulated aircraft component metal substrate being studied and corrosion conditions to which it had been previously exposed. The frequency range found most appropriate for this instrumentation in work performed during Phase I, corresponded to between 0.01Hz and 10kHz.

When the test signal was applied, controlling software allowed signal application and measurement of electrochemical impedance frequency response to be achieved. This was performed by feeding the pseudo-white noise signal into the D/A board to give a digital waveform test signal followed by conversion back to the original analog waveform. By this means we verified the utility of the D/A board for achieving both digital-to-analog and analog-to-digital conversion of this input signal. During Phase I three hundred different frequencies, ranging from 0.01Hz to 10kHz, were selected. The low frequency limit was selected to measure the impedance phase angle shift related to hidden corrosion phenomenon at metal aircraft component substrates under test, while the upper frequency limit was controlled by the Analog-to-Digital Conversion(ADC) speed.

The lowest frequency waveform was Fourier transformed into the base frequency, with higher values being generated as integral multiples of this frequency. Since each frequency value possessed associated harmonics, prime numbers were chosen as frequency multipliers. This prevented the harmonics of one wave from interfering with another. The pseudo-white noise signal used in the subject instrumentation was as a result a summation of these frequencies.

As a consequence of digitally created waveforms, the D/A board gave a small step function output rather than a smooth sine wave. A schematic of the instrumentation strategy developed during Phase I for pseudo-white noise signal generation is shown in Figure 3. Because these step functions could contain false high frequencies, circuitry was also designed and fabricated (Figure 4) incorporating Bessel low-pass filters which possessed linear phase shift and frequency cut offs near the sampling frequency of interest. Since low-pass filters do not exist which have an infinite cutoff we used frequencies less than one quarter of the sampling frequency. Using this technique, smooth electrochemical impedance patterns were obtained for frequency ranges between 0.01Hz and 10kHz.

Completion of work in this section provided a fully evaluated anti-alaised pseudo-white noise source for application as an excitation source to the electrochemical impedance cell.

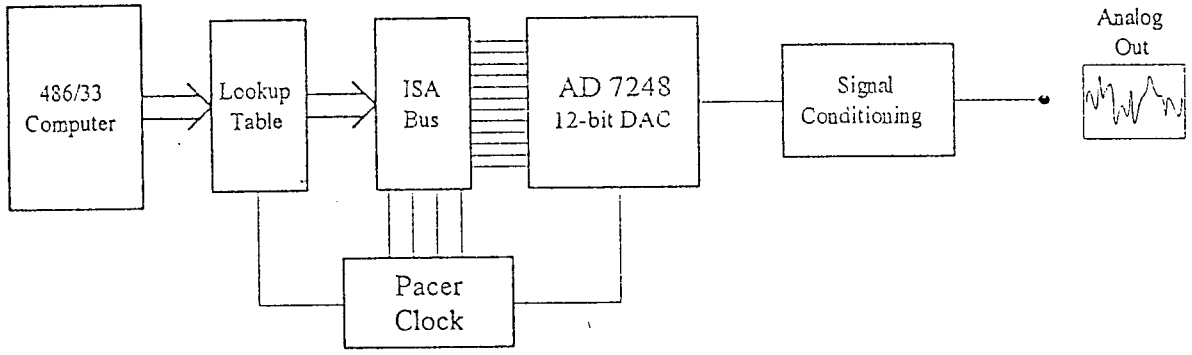

Figure 3. Block diagram of instrumentation strategy developed during Phase I for pseudo-white noise signal generation.

b) Analog-to-Digital Conversion

Circuitry used during Phase I for conversion of analog time domain impedance measurements from hidden corrosion sites on metal substrates to digital frequency domain impedance measurements is shown in Figure 5. Overall implementation of FFTEIS instrumentation involved application of a data acquisition and control card installed in a 486-33MHz MS-DOS based computer, a potentiostat, and the previously discussed custom signal conditioning circuit. Current and voltage signals were acquired and stored as an array in a hard disk file. Appropriate timing for the control program was performed through an interrupt service routine.

An ADA3100 Real Time Devices data acquisition and control card (installed in a 486-33MHz computer) was used to acquire current and voltage signals from electrochemical impedance measurements being performed at hidden corrosion sites. Specifications for the ADA3100 included an 8-channel multiplexer, programmable gain amplifier, sample-and-hold, 200kHz throughput successive approximation A/D, a pacer clock capable of generating interrupts, and two D/A's with settling times of 5 μs. Also included in the ADA3100 card was an 8K First In First Out (FIFO) memory module required for sampling rates greater than 20kHz.

A custom signal conditioning circuit was used to interface the ADA3100 to the impedance cell circuitry via the potentiostat. This circuit converted electrochemical impedance current and voltage signals from the 6-pole low pass Bessel filters previously

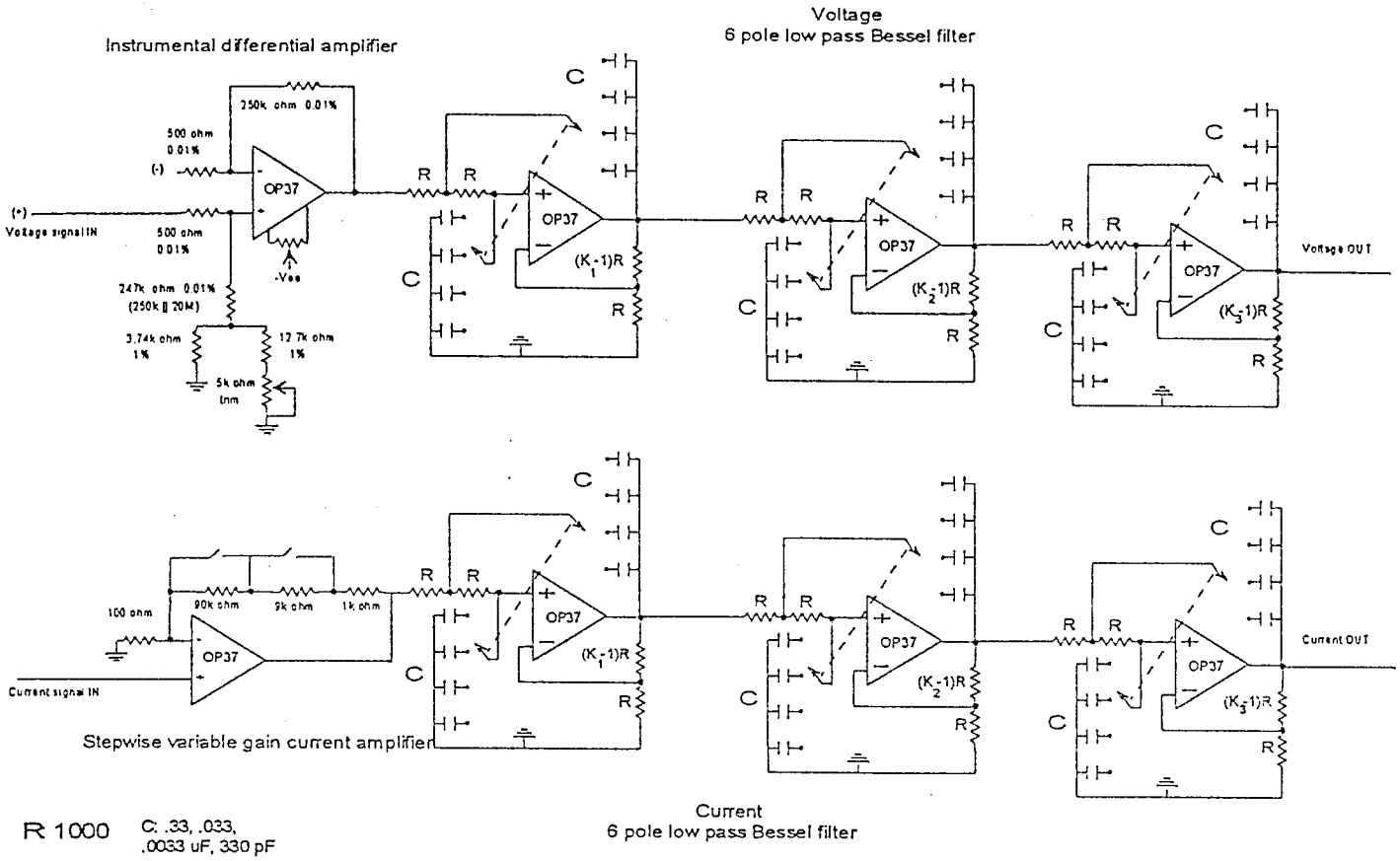

Figure 4. Amplification and filtering circuit designed and fabricated during Phase I for removal of false high frequencies from generated pseudo-white noise excitation signal.

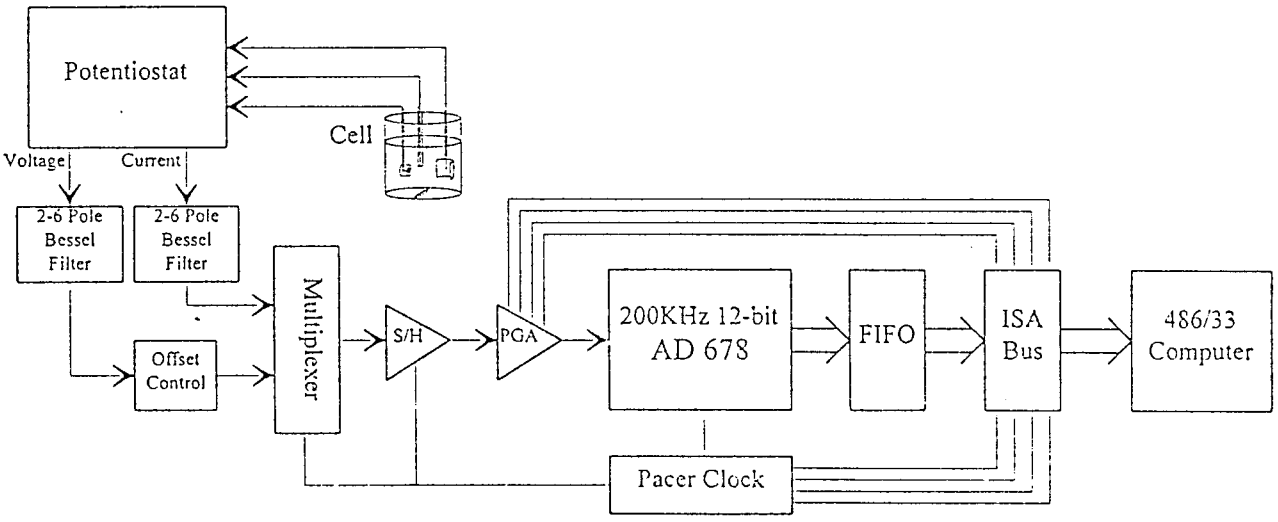

Figure 5. Block flow diagram of circuitry used during Phase I for A/D conversion of current and voltage waveforms resulting from electrochemical cell pseudo-white noise excitation.

shown in Figure 4 to approximately 10 volt peak to peak signals for A/D conversion. Voltage and current signals were then stored in a hard disk file. Control software performed this acquisition and conversion by means of an interrupt service routine initiated by a timing circuit on the ADA3100 board. Each time the interrupt service routine was called it would take a pair of current and voltage readings from the impedance cell. Voltage and current readings were amplified to $\pm$ 5V and digitized followed by storage in a FIFO memory. These readings were transferred to hard disk for storage.

Completion of this Analog to Digital process provided current and voltage data for subsequent FFT processing to be discussed next.

c) Fast Fourier Transform (FFT)

FFT conversion to transform the time domain impedance signal acquired by ADC circuitry to the frequency domain was performed using a Cooley-Tukey algorithm[19] software approach. Current and voltage data from the output file created by the A/D conversion was processed by the FFT program. Frequency versus impedance magnitude and phase angle resulted. Real and imaginary impedance components were obtained. These results were stored on a hard disk for subsequent Neural Network Analysis.

Successful completion of this task resulted in selecting a preferred laboratory instrumentation configuration for acquisition of FFTEIS patterns at respective aluminum and titanium alloy interface exposed to representative chemical corrosion conditions during Task 2. Verification of acceptable performance from impedance instrumentation was achieved by comparison with a slower commercially available EIS system. Direct correlation between measured impedance signals and hidden corrosion was achieved by performing systematic Scanning Electron Microscopy (SEM) measurements on hidden corrosion sites. Resulting impedance patterns were used to train the Neural Network during Task 3 for achieving the unambiguous real-time detection of hidden corrosion and grading its severity on aircraft components. This led to the fabrication and successful testing of prototype instrumentation during Task 4.

Task 2 Perform FFTEIS Measurements on Relevant Metal Substrates Subjected to Hidden Chemical Corrosion

a) Approach

This task was directed towards collecting FFTEIS patterns on relevant metal substrates possessing intentionally created hidden interfacial sites where corrosion could be induced. These measurements were performed using laboratory instrumentation developed in the previous task. Metal substrates ($1cm^2$ and 0.16cm thick) were initially prepared for corrosion testing. In particular, samples consisted of solid state junctions between either similar or dissimilar alloys. Representative metal alloy interface Al 2024/Al 2024; Al 7075/Al 7075; Ti 15-3/Ti 15-3; Al 20204/Al 7075; Al 2024/Ti 15-3, and Al 7075/Ti 15-3 were subjected to intentional corrosion.

Corrosion at these interfacial regions proceeded in both 0.1M HNO_3 and 0.1M H_2SO_4.

These aqueous solutions were selected to closely imitate relevant corrosion conditions to which aircraft components might be exposed. Since SO_x and NO_x atmospheric emissions, from combustion processes, lead to the accumulation of both nitric and sulfuric acid within clouds, metal aircraft components, and particularly interfacial regions between both similar and different components, would be vulnerable to hidden chemical corrosion effects accelerated by the presence of such species. The test sample configuration used in this work is schematically shown in Figure 6.

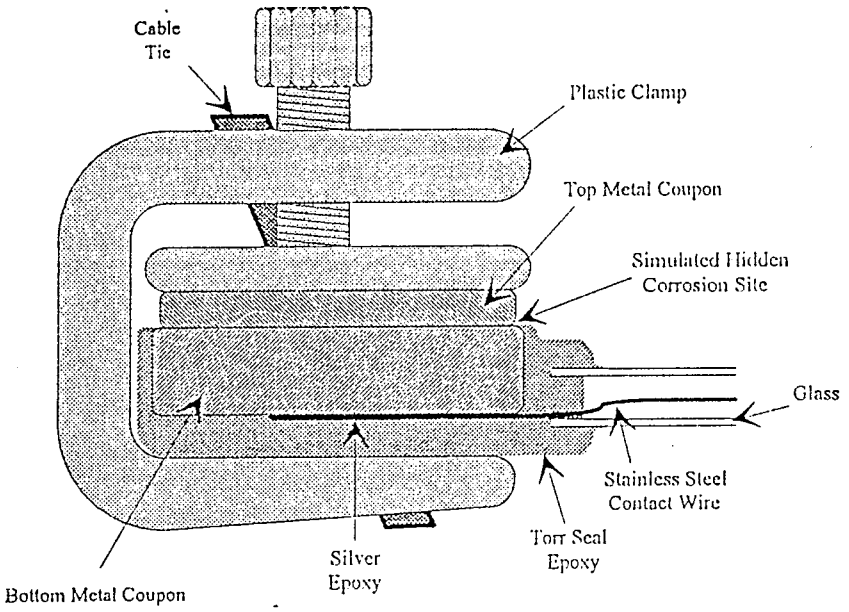

Figure 6. Schematic of hidden corrosion sample configuration used during Phase I.

Corrosion measurements on the metal interfacial region of interest were performed by initially removing test samples from the corrosion environment and immersing in 0.1M KNO_3 using the test cell shown schematically in Figure 7. FFTEIS measurements were performed by subjecting corrosion sample interface to a pseudo-white noise excitation signal over the frequency range 0.01 to 10kHz. During these measurements the metal interfacial region under test was exposed to an applied overpotential variation of $\pm$10mV from its initial electrochemical rest potential. Measurements were performed for all of the above discussed metal interfacial regions.

b) Summary of FFTEIS Measurements Performed on Hidden Corrosion Sites

During this task these general types of corrosion were observed on representative aircraft components. These corresponded to: 1) metal removal resulting in surface roughening, 2) crevices initiating and propagating along mating surfaces at metal/metal interfaces, labeled as "Simulated Hidden Corrosion Site" in Figure 6, and 3) pitting in the faying surfaces and on exposed vertical coupon regions, immediately above the "Simulated Hidden Corrosion Site." Ubiquitous corrosion products accumulated in pits and in crevices

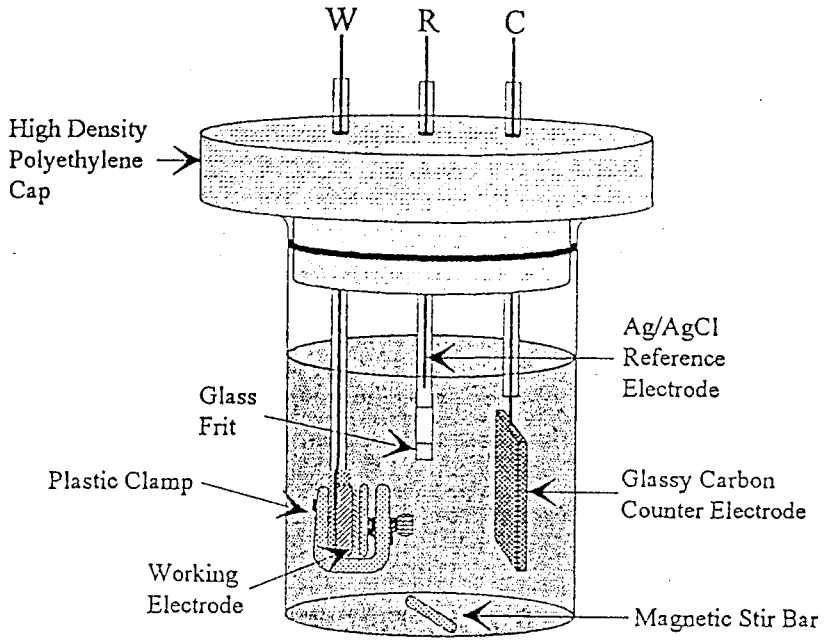

Figure 7. Schematic of electrochemical impedance cell configuration used during Phase I for monitoring hidden corrosion on metal substrate electrode test coupons.

but otherwise formed thin layers over all exposed coupon surfaces.

Generalized coupon metal dissolution proceeded on the exposed metal surface at constant rates throughout each experiment. Upon initial sample exposure to the acidic corrosion environment its surface became roughened thereby increasing the EIS measured area as reflected in EIS phase angle data. These changes in impedance phase angle data were only small. At the inception of crevice or pitting corrosion however large changes in area gave more significant changes in impedance phase angle data. Impedance changes relating to surface roughening were found to reach a plateau value after $\simeq$200 hours, whereas crevice or pitting corrosion progressively increased with time.

Coupon alloy interface and acid exposure experimental configurations were chosen to simulate aircraft exposure conditions as discussed earlier. In the following discussion FFTEIS and physical measurements of hidden corrosion for seven representative alloy/alloy interface and acid electrolyte environments will be reported. Results found during Phase I can be illustrated by considering measurements on the respective interface Al 7075/Al 2024, Al 7075/Ti 15-3 and Al 2024/Ti 15-3 exposed to 0.1M H_2SO_4 and 0.1M HNO_3. An asymmetrical experimental configuration was required to eliminate corrosion of the current collection wire. As shown in Figure 6 all sides of the top coupon and one face of the bottom coupon were exposed to the corrosion environment. Inverse specimen configurations were also evaluated to determine if any differences in corrosion severity could be attributed to this asymmetry. This was performed on the Al 2024/Ti 15-3 configuration wherein the aluminum/titanium order was reversed so as to expose the entire titanium coupon to the corrosion environment. Table 1 summarizes interfacial configurations and corrosion environments being discussed here. Over twenty interface were studied during performance of this program.

FFTEIS corrosion measurements were taken at logarithmically increasing time intervals

TABLE 1.
Representative Experimental Sample Configurations and Corrosion Environments used during Phase I for FFTEIS Measurements

Sample #	Top Coupon	Bottom Coupon	Corrosion Environment	Time (Hrs.)
1	Al 7075	Al 2024	HNO_3	1308
2	Al 7075	Al 2024	H_2SO_4	1342
3	Al 7075	Ti 15-3	H_2SO_4	1353
4	Al 2024	Ti 15-3	H_2SO_4	426.5
5	Ti 15-3	Al 2024	H_2SO_4	289.5
6	Ti 15-3	Al 7075	HNO_3	1412
7	Ti 15-3	Al 2024	HNO_3	1358

until approximately 1300 hours cumulative exposure to the environment of interest was achieved. For samples shown in Table 1 there were however two exceptions to this: 1) sample 5 in Table 1 (Ti 15-3/Al 2024 in H_2SO_4), developed a leak in the insulating Torr Seal which permitted acid to reach the current collecting stainless steel wire, and 2) sample 4 (Al 2024/Ti 15-3 in 0.1M H_2SO_4), was removed from the corrosion environment to physically compare with the inversely configured sample (Sample 5). Scanning Electron Microscopy (SEM) and Energy Dispersive X-ray Analysis (EDX) measurements were performed to physically characterize corrosion interfacial sites after dissambly. Both a Cambridge Stereoscope 250 Mark II SEM and an in house JEOL-T-200 Scanning Electron Microscope with a Princeton Gamma Tech Energy Dispersive X-ray Analysis System were used. Physical corrosion measurements were performed after final FFTEIS measurements. Corrosion severity could be correlated with phase angle data whereas impedance magnitude data was found to be relatively insensitive to sample exposure time in the corrosion environment. This is illustrated for sample 1 (Table 1) corresponding to Al 7075/Al 2024 interface, following exposure to 0.1M HNO_3 in Figure 8 (A-F) by phase angle vs. frequency data and Figure 9 (A-F) impedance magnitude vs. frequency plots. The phase angle data became clearly differentiated at long exposure times, as seen in Figure 8 D, E and F. In comparison impedance magnitude was found to change little as shown in Figure 9 D, E and F. As a consequence of these experimental observations phase angle data was selected for both corrosion detection and severity determination. This will be applicable for the detection of aircraft hidden corrosion sites following exposure to atmospheric corrosion for long times.

In order to identify preferred impedance data parameters both magnitude and phase angle shift data were examined. As is well documented impedance magnitude and phase angle are mathematically related but independently measure electrochemical impedance behavior. The experimental impedance magnitude data were fit with two exponential curves (Figure 9) and phase shift angle data with two log-normal curves (Figure 8).

Narrative Continues on Page 20

A)

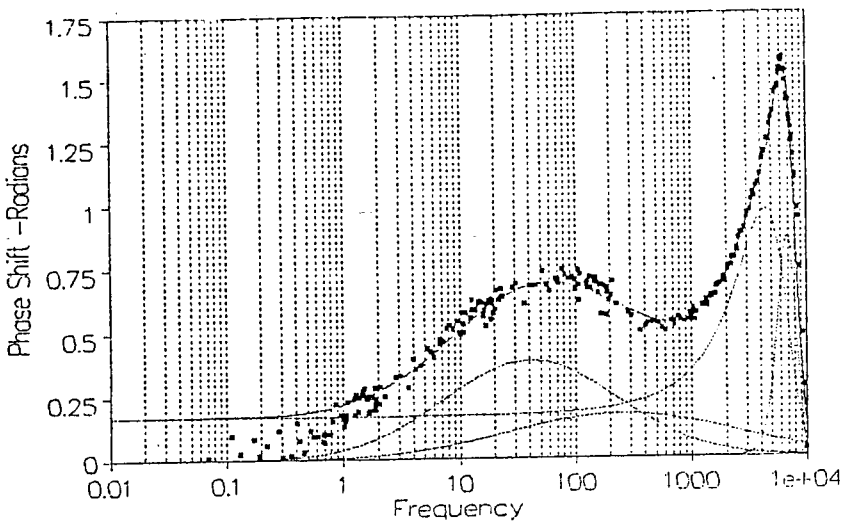

B)

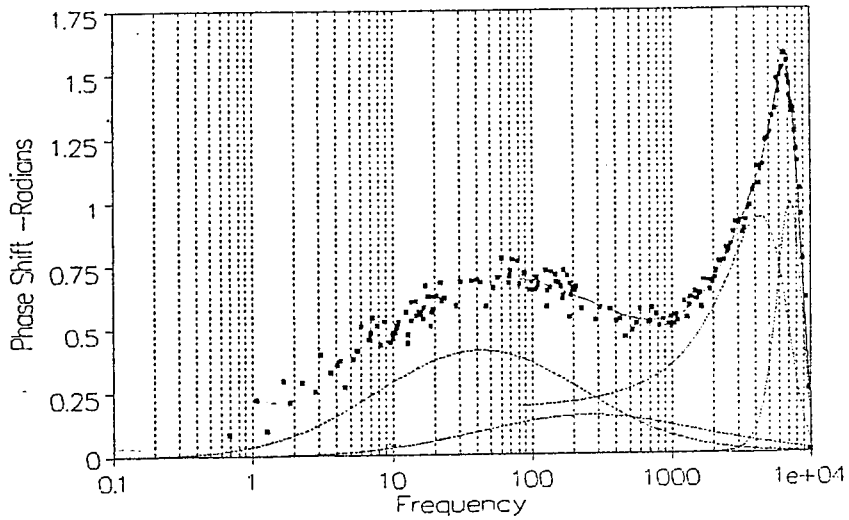

C)

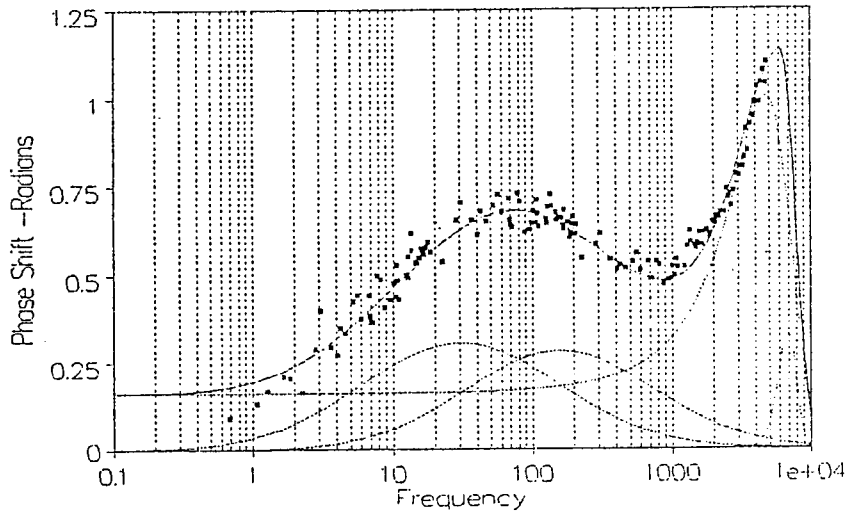

Figure 8 (A, B and C).

FFTEIS measured phase angle dependency on frequency for Al 7075/Al 2024 interface exposed to 0.1M HNO_3 after A) 74 hours, B) 99.5 hours, and C) 144.5 hours. Best fit log-normal curves shown over 0.1 to 1000 Hz range.

D)

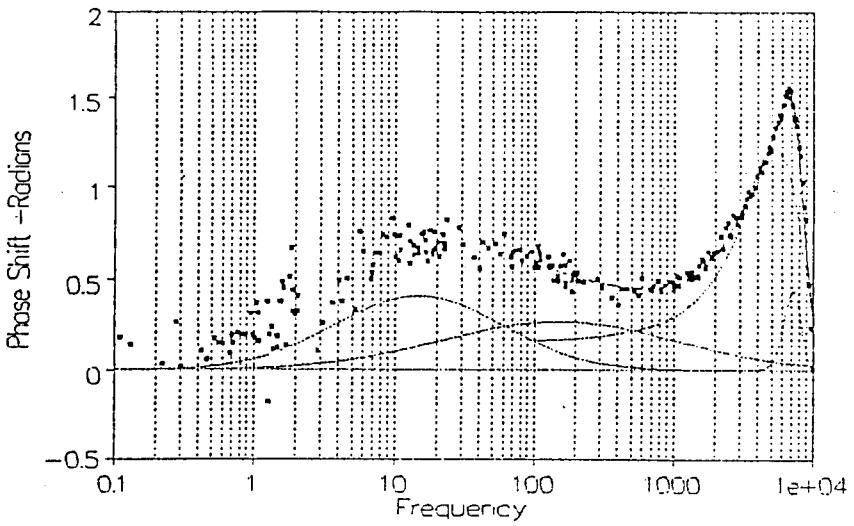

E)

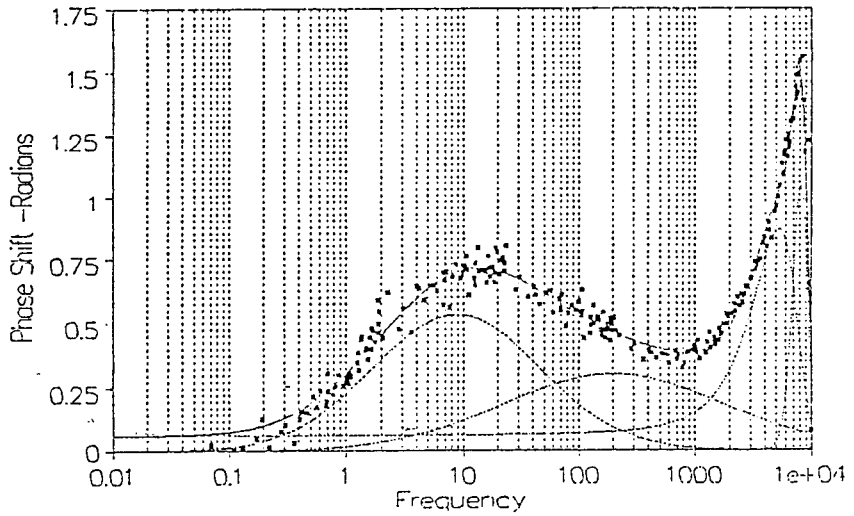

F)

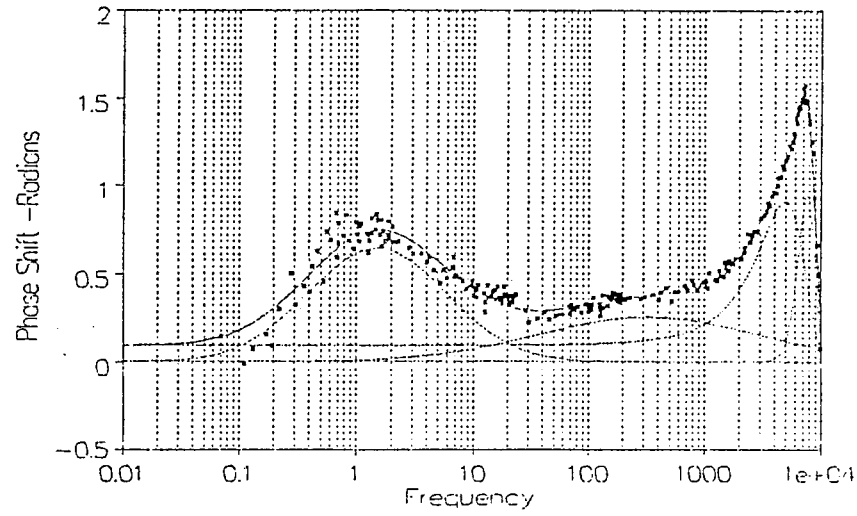

Figure 8 (D, E and F).
FFTEIS measured phase angle dependency on frequency for Al 7075/Al 2024 interface exposed to 0.1M HNO_3 after D) 265.5 hours, E) 471.5 hours, and F) 1308 hours. Best fit log-normal curves shown over 0.1 to 1000 Hz range.

A)

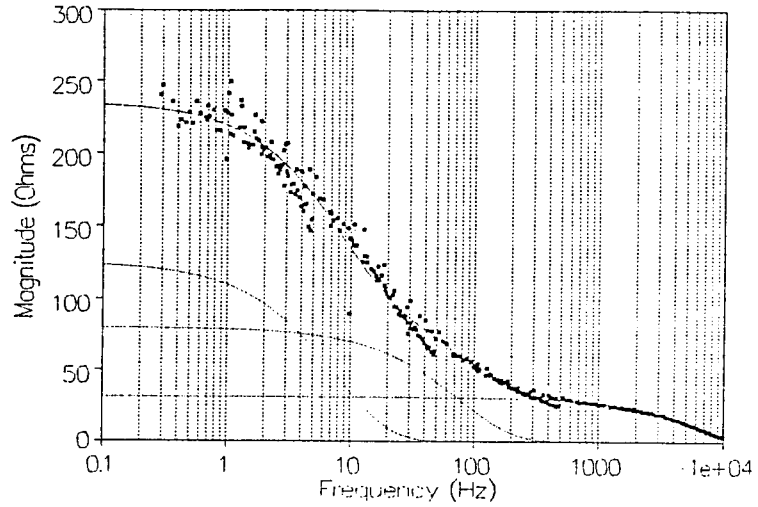

B)

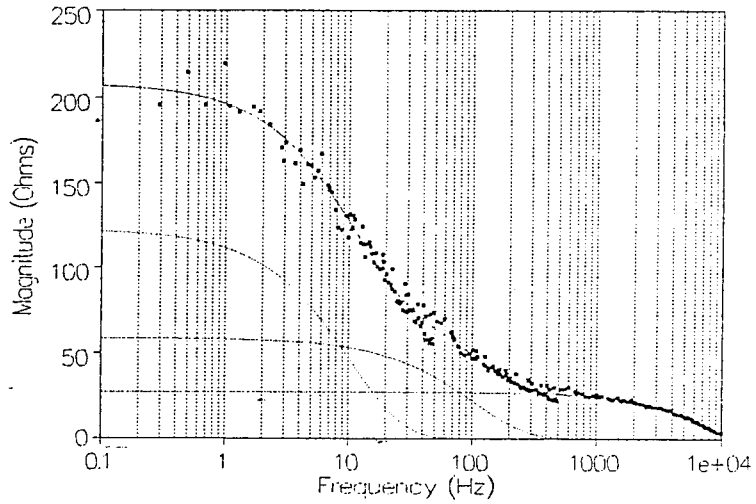

C)

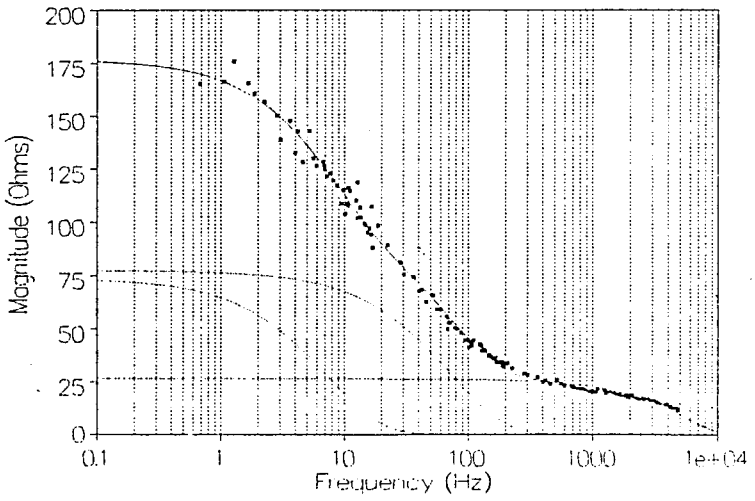

Figure 9 (A, B and C).

FFTEIS measured phase angle dependency on frequency for Al 7075/Al 2024 interface exposed to 0.1M HNO_3 after A) 74 hours, B) 99.5 hours, and C) 144.5 hours. Best fit log-normal curves shown over 0.1 to 1000 Hz range.

D)

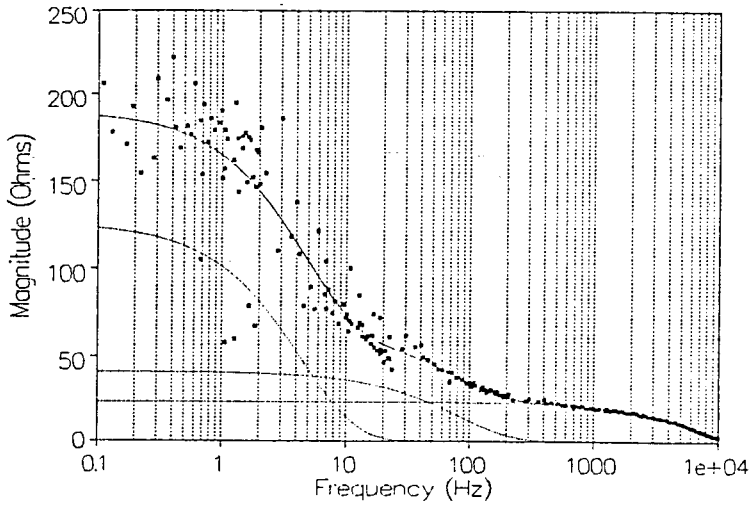

E)

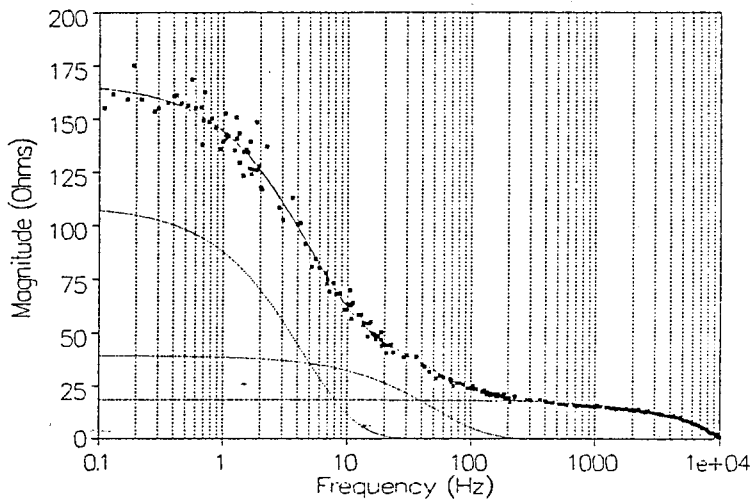

F)

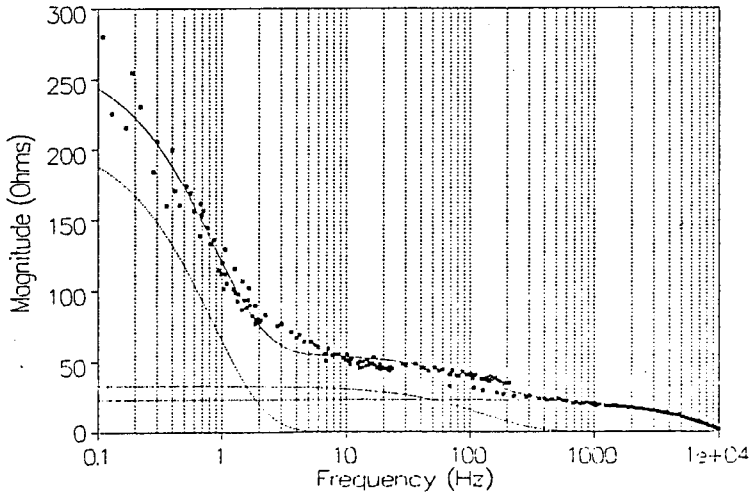

Figure 9 (D, E and F).
FFTEIS measured phase angle dependency on frequency for Al 7075/Al 2024 interface exposed to 0.1M HNO_3 after D) 265.5 hours, E) 471.5 hours, and F) 1308 hours. Best fit log-normal curves shown over 0.1 to 1000 Hz range.

Phase shift angle data, as typified in Figure 8 A-F required two log-normal functions for optimal curve fit because two distinct corrosion processes were being simultaneously measured. The first process resulted in an initial phase angle log-normal peak centroid at approximately 300 Hz. This centroid position changed with exposure time to the corrosion environment as shown in Figure 10. In the second process the phase angle centroid changed position as a function of corrosion time, as illustrated in Figure 11.

The corrosion process detected from the first phase angle centroid resulted from initial surface roughening corrosion attack on all coupon regions exposed to the corrosion environment. This surface roughening corrosion would not be detected on aircraft components because anodization is included in the manufacturing process. Therefore initial surface roughening corrosion is an artifact since anodization was absent from experimental samples used in this task. This was an expedient used in this program to increase susceptibility to the inception of hidden corrosion.

Pitting and crevice corrosion which developed with time were detected and measured using the second phase angle peak, and subsequently confirmed by SEM examination. From this data hidden corrosion severity was correlated with impedance phase angle as a function of frequency.

Corrosion severity for coupon interface configurations in this program can then be determined through geometrical modeling of pits and crevices. Three dimensional pit and crevice shape parameters correspond to increased surface area following corrosion exposure. For the Al 7075/Al 2024 corrosion sample (Sample 1) SEM examination of interfacial aluminum surfaces identified plateau structures (Figure 12) which were compatible for modelling as rectangular trenches produced at the interface of each alloy as schematically illustrated in Figure 13. Surface area for the crevice corrosion trench was given by:

$$\text{Surface Area (trench)} = (2 \text{ X depth} + \text{width}) \text{ X trench length} \qquad (8)$$

Figure 14 reveals pits in the surface at the coupon edge, originally 0.16 cm thick. These

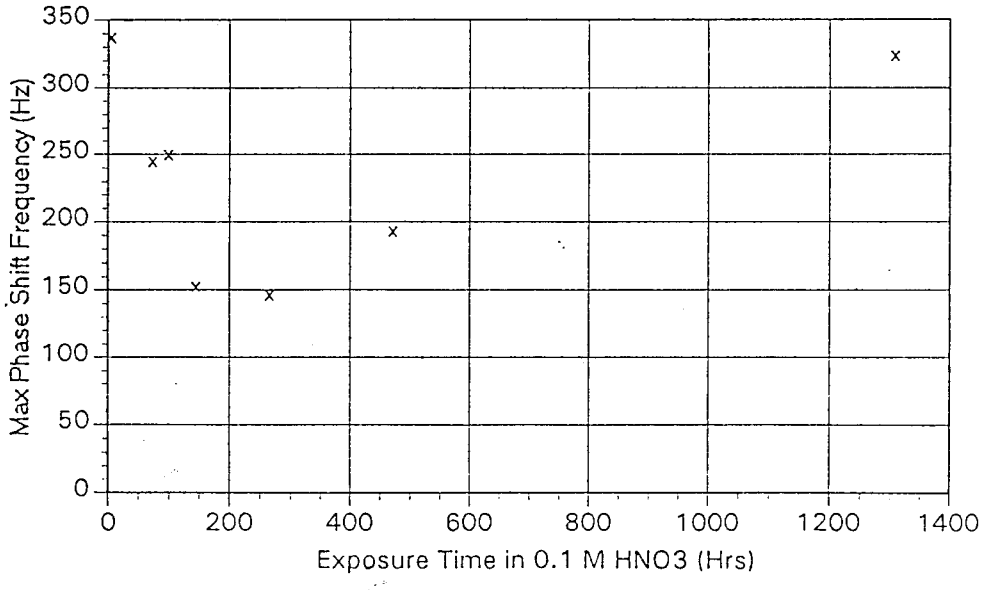

Figure 10. Position change of first log-normal peak centroid as a function of exposure time in 0.1M HNO_3 for Al 7075/Al 2024 coupons.

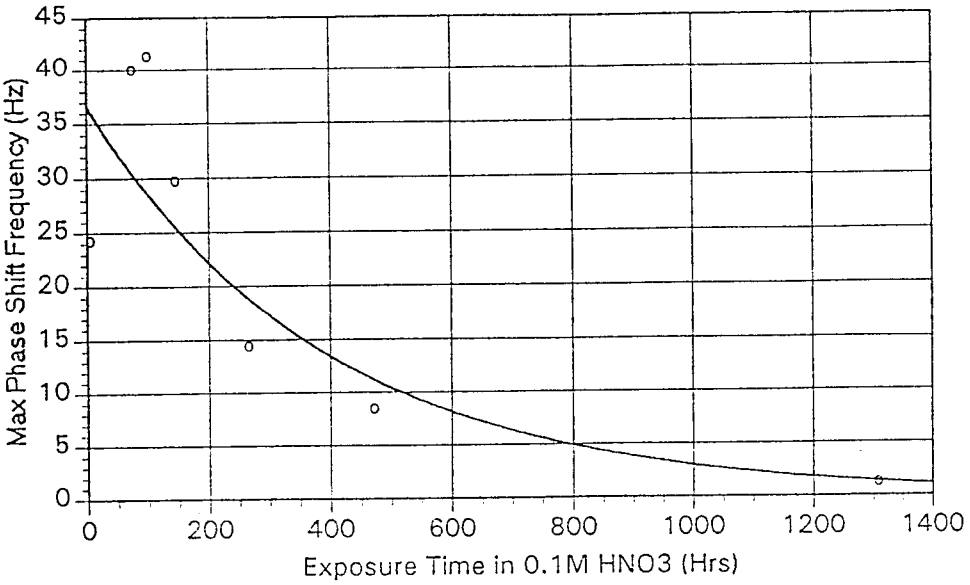

Figure 11. Position change of first Log-normal peak centroid as a function of exposure time in 0.1M HNO_2 for Al 7075/Al 2024 coupons.

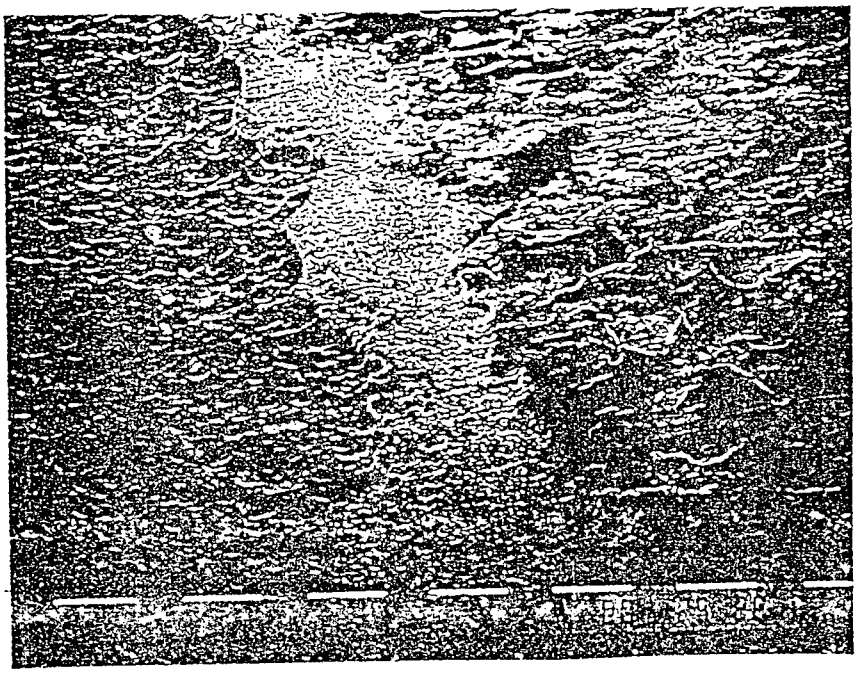

Figure 12. Scanning Electron Micrograph of Al 7075 coupon after exposure to 1308 hours in 0.1M HNO_3 at Al 7075/Al 2024 interface. Plateau structures are typical of crevice corrosion attack and modeled as rectangular trenchs cut into each alloy at the interface as shown in Figure 13. Dimension shown = 100 microns.

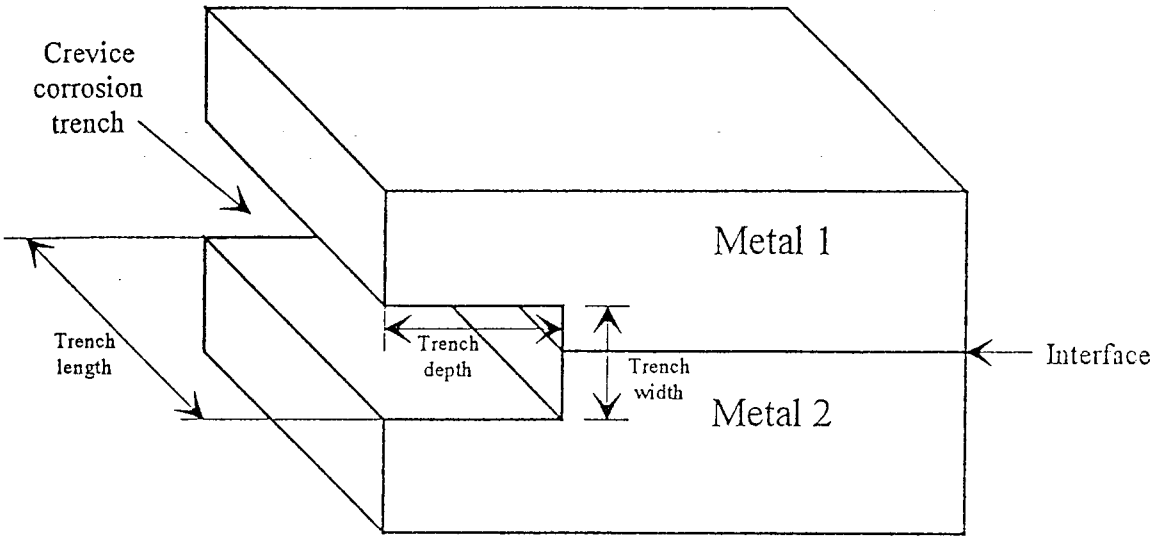

Figure 13. Schematic illustration of crevice corrosion at metal alloy interface. To a first approximation, the crevice can be represented as a rectangular trench. In general, corrosion will attack each metal alloy at different rates.

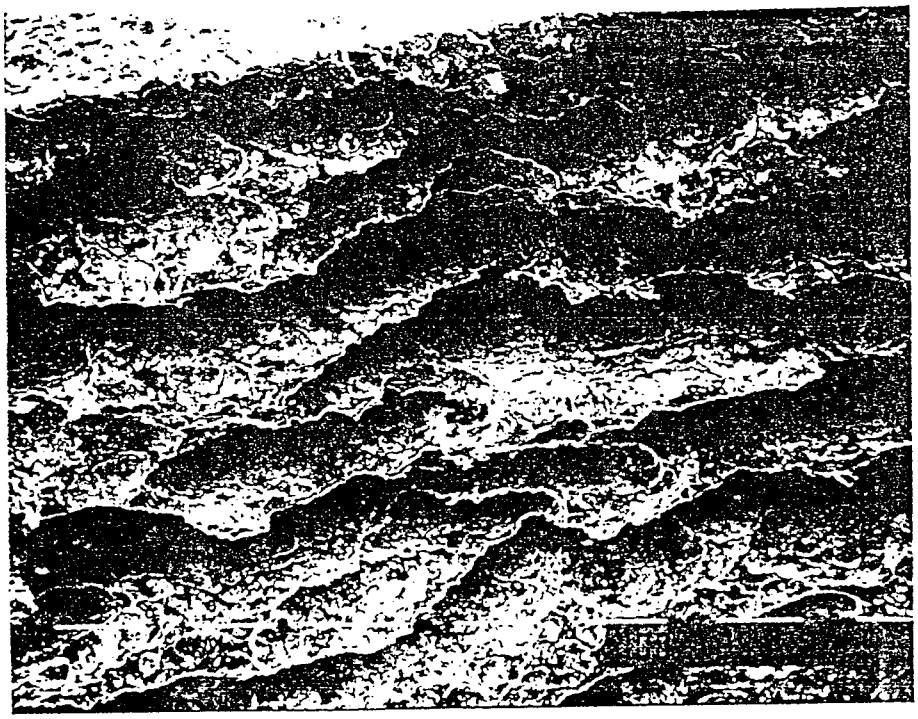

Figure 14. Scanning Electron Micrograph of Al 7075 coupon after exposure to 1308 hours in 0.1M HNO_3 at vertical edge originally 0.16cm thick. These pits are ellipsoidal in cross section and modeled by spheroids. Dimension shown = 100 microns.

pits were ellipsoidal in cross section and could be modeled as prolate spheroids. Corrosion pit surface area illustrated in Figure 15 was given by:

$$surface\ area\ (spheroid) = 2\pi b^2 + 2\pi \frac{ab}{\epsilon} \sin^{-1} \epsilon \qquad (9)$$

where a and b were semi-major and -minor axes, and ϵ was the eccentricity given by:

$$\epsilon = \frac{\sqrt{a^2 - b^2}}{a} \qquad (10)$$

A large number of similar pits are shown in Figure 14 for the Al 7075 coupon thereby increasing the effective area measured by FFTEIS. This capacitive area increase measured by FFTEIS provides information on both corrosion depth and rate for these aircraft alloy hidden corrosion sites and contribute fundamental insight into the nature of corrosion propagation through geometrical modelling previously discussed.

As will become evident in this Final Report, experimental results obtained and developed procedures were shown compatible for simultaneously detecting multiple corrosion processes at a given hidden corrosion site. Corrosion mechanisms and rates were non-destructively quantified using this *in situ* measurement technique and parameterized to the corrosion environment. As a consequence of these findings work performed in this task resulted in identifying preferred impedance parameters for detection of specific hidden corrosion mechanisms. These parameters were then incorporated into NNA during Task 3 for correlating hidden corrosion severity as a function of time.

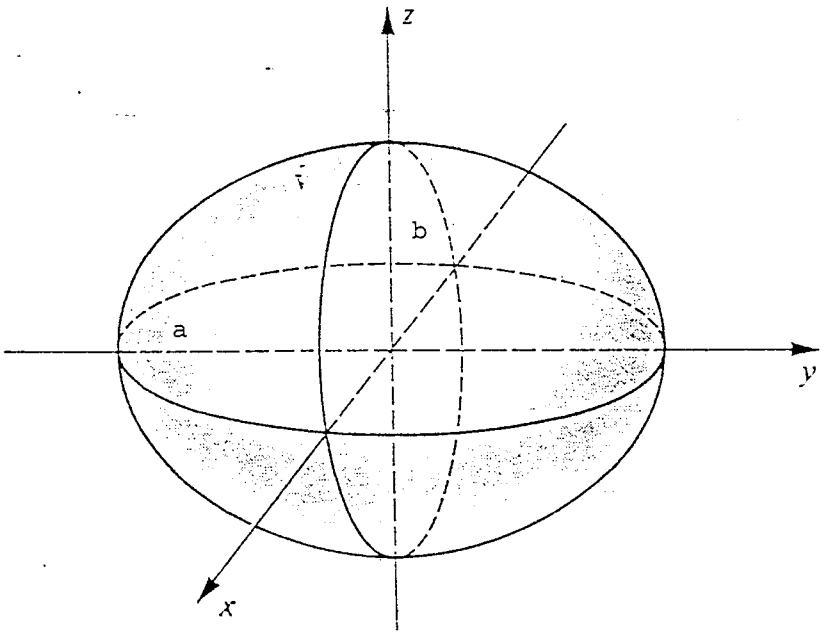

Figure 15. Prolate spheroid surface for modelling the corrosion found in Al 7075 alloy possessing one half the surface area shown in equation 9.

c) Specific Experimental Results Obtained on Corrosion Samples Investigated during Performance of this task

In this section specific experimental results for representative corrosion samples shown in Table 1 are discussed. This will emphasize: 1) Scanning Electron Micrographs for revealing the physical consequences of hidden corrosion at defined times, 2) energy dispersive X-ray analysis for detecting corrosion products, 3) impedance phase angle peak centroids as a function of time for hidden corrosion processes, and 4) phase angle data at defined times. For reference, SEMs of uncorroded Al 2024 and Ti 15-3 coupons are respectively presented in Figures 16 and 17 which illustrate original surface topography. **For the convenience of reading this document from now on figures in this section have been incorporated into an Appendix.**

Specific results obtained will now be discussed for defined interface and corrosion exposure times on samples investigated in this task.

Sample 1) Al 7075/Al 2024 in 0.1M HNO_3 - Total Exposure 1308 Hours

Scanning Electron Micrographs of interfacial crevice corrosion on the Al 7075 coupon illustrate plateaus measuring 40 μm in height as shown earlier in Figures 12 and 14. The amorphous scale observed at the right of Figure 12 was the corrosion product. Energy dispersive X-ray analysis (EDX) identified this as corresponding to aluminum and copper nitrates. Figure 14 illustrates pitting attack having an average width and depth in from the original surface, of 400 and 200 μm respectively. At this surface edge the coupon thickness was reduced to approximately 10% from its original value.

Al 2024 coupon crevice corrosion, illustrated in Figures 18 and 19, shows effective average "trench" depths corresponding to 2000 and 800 μm respectively for different coupon interfacial regions. The right edge of Figure 19 shows a rounded corner caused by surface roughening which progressed throughout corrosion exposure. Micrometer measurements performed on the coupon width at the interface surface determined the coupon was 480 μm narrower than originally. Optical microscope examination identified the coupon to be trapezoidal in cross section.

This trapezoidal cross section provided critical evidence to explain the first log-normal phase angle peak centroid position change found as a function of time, previously shown in Figure 10. The initial coupon surface roughening, prior to substantial crevice or pitting formation, increased the capacitive area being detected by impedance measurements. This resulted in decreasing the first peak centroid frequency in Figure 10. This corrosion attack began to round off coupon corners, allowing exposure of more metal to the corrosion environment. Figure 20 schematically illustrates this process. As the corner was exposed to attack from top and side, rounding accelerated, exposing more side metal and simultaneously beveling the corner, resulting in reducing the effective area. This was because two nearly perpendicular sides were replaced by one beveled side represented by the hypotenuse of the original triangle. Corrosion at the Torr Seal/metal corner slowed as the bevel angle approached an asymptotic value. This surface roughened area was measured by FFTEIS, as reflected in the first log-normal peak position.

FFTEIS phase angle peak centroids for hidden corrosion have previously been shown

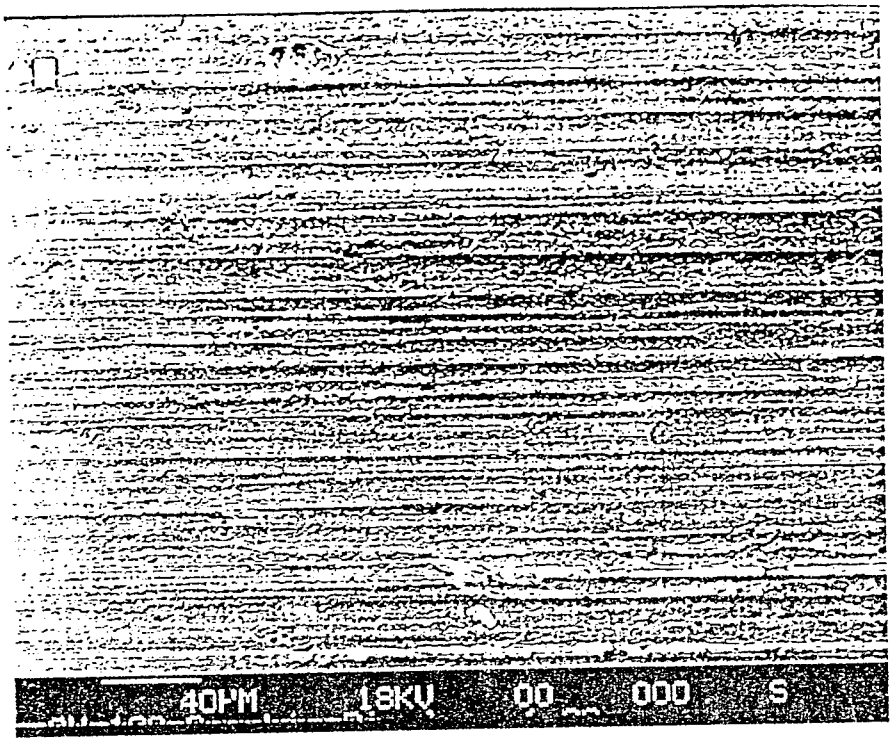

Figure 16. Scanning electron micrograph of Al 2024 coupon prior to corrosion exposure. Dimension shown = 40 microns.

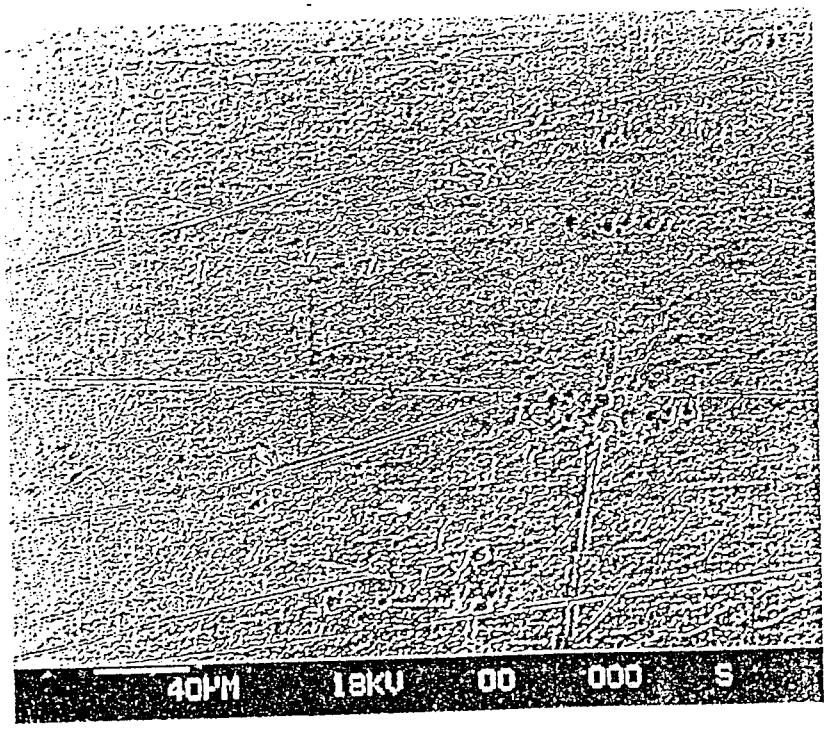

Figure 17. Scanning electron micrograph of Ti 15-3 coupon prior to corrosion exposure. Dimension shown = 40 microns.

in Figure 11. As discussed earlier experimental data for initial exposure times resulted from surface roughening corrosion. Therefore, hidden corrosion phase angle results shown in Figure 21 included peak centroids only after 50 hours of exposure. Peak centroid positions were obtained by optimally adjusting curve fitting parameters given by the log-normal equation:

$$phase\ shift = a_0 \exp\left[-0.5\left(-\frac{ln\left(\frac{X}{a_1}\right)}{a_2}\right)^2\right] \qquad (10)$$

where a_0 = amplitude, a_1 = centroid, a_2 = width and X was the measuring frequency.

Sample 2) Al 7075/Al 2024 in 0.1M H_2SO_4 - Total Exposure 1342 Hours

SEM's of pits and corrosion product in Al 7075 and Al 2024 alloy interfacial surfaces are presented in Figures 22 and 23 respectively. Corrosion pits were found to be approximately the same size and 50 μm deep. Corrosion product accumulated adjacent to the Al 7075 pit as shown at the upper right of Figure 22. Visually this corrosion appeared black. In comparison white corrosion product was found evenly distributed across the Al 2024 alloy pit, accounting for the relatively smooth appearance of Figure 23. For this latter sample where holes occurred in the corrosion by-product, the underlying roughened metal texture was observed. Figures 24 and 25 show EDX analysis of these by-products which indicate that sulfur (presumably as sulfate) was present in both regions. However the Al 2024 corrosion product contained six times more sulfur than the Al 7075 coupon.

Figures 26 and 27 for Al 7075 and Figure 28 for Al 2024 show micrographs of each respective coupon vertical edge. Figure 27 reveals the width and depth of the large pit shown in Figure 26 to be 500 and 250 μm respectively with a surface area of 70 mm^2. Measurement of pitting width across this vertical edge identified a 50% reduction in thickness. As seen in Figure 28, alloy Al 2024 was highly roughened but not deeply pitted.

Impedance phase angle peak centroids for hidden corrosion following exposure for 50 hours in this environment are shown in Figure 29. Figure 30 (A-F) show the FFTEIS phase angle vs. frequency data and optimal log-normal curve fit for each exposure time. Only a single log-normal curve fit was found after 4 hours cumulative corrosion exposure because of the predominant initial surface roughening process.

Sample 3) Al 7075/Ti 15-3 in 0.1M H_2SO_4 - Total Exposure 1353 Hours

SEM's of the Al 7075 interfacial surface identified the shallow 15 μm crevice corrosion plateau shown in Figure 31. Three distinct corrosion regions were observed, 1) a recessed area of attacked metal seen on the micrograph left side, 2) unattacked metal with fine grain corrosion product in the center, and 3) a thick cracked corrosion product on the far right side. EDX analysis revealed substrate constituents identical to that shown in Figure 24 for these corrosion products. The vertical exposed edge of the Al 7075 coupon is shown in Figure 32. In this figure uniformly distributed small pits are seen with 35 μm average width. Pit depth was also 35 μm on average, therefore the remaining coupon thickness was greater than 90% following corrosion. SEM corrosion analysis of the titanium coupon

revealed infrequent and widely spaced metal attack, shown in Figure 33 as horizontal shallow pit lines. These metal dissolution sites were located opposite crevice corrosion recesses on the Al 7075 coupon. Dark areas at the micrograph top were identified as residual corrosion product from the aluminum coupon since they had the composition of the thick cracked material seen in Figure 31 and analyzed in Figure 24.

Phase angle peak centroids for hidden corrosion, following exposure to this environment for 50 hours are shown in Figure 34. Figure 35 (A-F) shows the FFTEIS phase angle vs. frequency data and the optimal log-normal curve fit for each exposure times between 40 hours and 1353 hours. At later exposure times only the second log-normal phase angle peak was found to be significant for detecting hidden corrosion.

Sample 4) Al 2024/Ti 15-3 in 0.1M H_2SO_4 - Total Exposure 426.5 Hours

SEM's for the aluminum interfacial surface revealed, in Figures 36 and 37, only a few small pits. Figure 36 is a 30 X magnification micrograph of the interfacial surface. Pits are indicated by dark spots in the lower left corner. Plateau structures typical of crevice corrosion were not observed. Figure 37 is a 200 X magnification examination of a 70 μm wide pit also revealing the degree of surface roughness resulting from initial corrosion. The vertical coupon edge seen at the left side of Figure 36 has a roughened surface and few deep pits. One group of pits was discovered on the vertical edge of the Al 2024 coupon, shown in Figure 38 and enlarged in Figure 39. The pits extend for 950 μm parallel to the 1 cm^2 coupon faces with respective width 80 μm and depth 50 μm. The coupon thickness was again reduced to 90% of its original value. The roughened titanium coupon surface opposite the pits shown in Figure 36 was examined at 500 X magnification and illustrated in Figure 40.

Phase angle peak centroids for hidden corrosion following exposure after 25 hours are shown in Figure 41. Figure 42 (A-E) shows the FFTEIS phase angle vs. frequency data and optimal log-normal curve fits for each corrosion exposure time between 27 and 426.5 hours. At 27 hours cumulative corrosion exposure phase angle data had a single dominant log-normal peak as previously observed, corresponding to the initial surface roughening process.

Sample 5) Ti 15-3/Al 2024 in 0.1 M H_2SO_4 - Total Exposure 289.5 Hours

The micrograph shown in Figure 43 shows a 1600 μm broad and 300 μm deep pit at the Al 2024 coupon interfacial surface. Corrosion product at the pit was analyzed by EDX and found to contain sulfur as expected. Comparison of Al 2024 alloy composition before and after corrosion exposure is shown in Figures 44 and 45. Metal thickness was reduced to 80% of its original value. In addition to the presence of sulfur in Figure 45 the relative concentration of copper increased 100% as revealed from larger Cu peak amplitudes. Interfacial Ti 15-3 coupon surfaces were found to have parallel regions of metal dissolution 25 μm wide and 20 μm deep, as shown in Figure 46. Titanium composition did not change following 289 hours exposure to 0.1M H_2SO_4.

Phase angle peak centroids for hidden corrosion following corrosion for 25 hours are shown in Figure 47. Figure 48 (A-E) consists of FFTEIS phase angle data and includes log-normal peaks shown in Figure 47.

Sample 6) Ti 15-3/Al 7075 in 0.1M HNO_3 - Total Exposure 1412 Hours

As previously discussed surface roughening corrosion attacked the embedded aluminum coupon resulting in metal dissolution at the Torr Seal metal interface. The exposed aluminum coupon interfacial surface dimension was reduced 6% from 1 cm to 0.94 cm resulting in a trapezoidal coupon cross section. Crevice corrosion was observed in SEM's of interfacial surfaces as shown in Figures 49 and 50. Corrosion dissolution was determined to be 200 μm deep in two steps. At the left of Figure 49 unattacked metal is shown adjacent to the first step with a depth of 50 μm, followed by a second step of 150 μm deep at the right. Figure 50 reveals this second corrosion step in greater detail.

Visual examination of the titanium coupon interfacial region identified a copper colored corrosion product. Ti 15-3 coupon SEM examination is shown in Figures 51 through 53. The upper two thirds of the Figure 51 micrograph represent the interfacial area. Dark and light regions are present as shown in Figures 52 and 53. Texture other than in the lower left of Figure 52 resulted from surface roughening. Texture in Figure 53 corresponded to the corrosion product. In Figure 54, EDX analysis at the Figure 53 location revealed Al and Cu in addition to the expected Ti and V. The large central EDX peaks corresponded to Ti and V, with smaller peaks located at 1.5 and 8 KeV corresponding to Al and Cu respectively. Corrosion processes resulted in removing material from the Al 7075 coupon and redeposited it on the Ti 15-3 coupon.

Phase angle peak centroids for hidden corrosion following exposure after 50 hours are shown in Figure 55. Figure 56 (A-F) consists of the FFTEIS phase angle data and includes log-normal peaks shown in Figure 55.

Sample 7) Ti 15-3/Al 2024 in 0.1M HNO_3 - Total Exposure 1358 Hours

For the aluminum coupon at a heavily corrosion attacked edge, thickness was reduced to 20% of original due to pits from 400 μm to 1.3 mm wide and 1 mm deep. Crevice corrosion was observed in SEM's of Al 2024 coupon interfacial surfaces, as shown in Figures 57 and 58. The micrograph shown in Figure 57 indicates roughening in a 6 mm X 2.6 mm X 1 mm deep Ti 15-3/Al 2024 interfacial pit. The breadth and shallowness of these pits prevented convenient SEM presentation due to the minimum 35 X magnification used. Corrosion products seen at the right side of Figure 58 were analyzed with EDX revealing the presence of aluminum and copper nitrates. A crevice corrosion plateau was revealed in the upper right of Figure 59. Coupon metal thickness was reduced to 30% of its original value.

SEM examination of the Ti 15-3 coupon interfacial region shows scratches and corrosion product in Figure 60. Corrosion product EDX analysis again identified aluminum and copper, as had been found on the prior specimen.

Phase angle peak centroids for hidden corrosion following exposure after 40 hours are shown in Figure 61. Figure 62 (A-F) consists of the FFTEIS phase angle data and includes the log-normal peaks shown in Figure 61.

The increasing presence of hidden corrosion at metal interfacial sites was manifested by a progressive impedance phase angle shift to lower frequencies. This was consistent with the expectation that as the hidden corrosion depth increased the phase angle for measured capacitance moved to lower frequencies. Successful completion of this task resulted in the

ability to directly correlate electrochemical impedance data to the presence and degree of hidden corrosion at metal alloy interface present in aircraft components. This data was then used for the subsequent training of Neural Networks for hidden corrosion severity prediction in the next task.

Task 3 Develop and Train Neural Networks for Unambiguously Detecting and Determining the Severity of Hidden Chemical Corrosion on Metal Substrates

The objective of this task was to develop a Neural Network that could both detect corrosion occurring on the surface of aircraft metal components and grade its severity. As a pattern recognition strategy for classification of corrosion type and severity on aircraft components, impedance patterns experimentally obtained from intentionally corroded metal substrates during Task 2 were used to train the Neural Network.

NeuroShell 2, a commercially available Neural Network program, was used for NNA of experimental impedance data. Backpropagation architecture was used with three layers, each interconnected only to adjacent layers. Backpropagation supported up to five layers of interconnection with sequential, jump and recurrent interconnections between layers. Backpropagation was deemed particularly appropriate for corrosion classification because it excelled in processing time series data. As previously discussed, the phase angle moved to lower frequencies as corrosion exposure time of the metal/metal interface increased. Input data features detected by the Neural Net were accounted for and fed back to input layer nodes via the hidden layer. The input layer required 202 nodes, with each being represented with one frequency. The phase angle, in radians, was input for each frequency. Experimental performance was determined to require 104 hidden nodes. Two output nodes corresponded to i) sample corrosion exposure time, and ii) the corrosion induced phase angle shift peak centroid. These outputs characterized corrosion as previously shown in Figure 11.

Neural Network pattern recognition of each alloy interfacial site was achieved by training with certain impedance data sets, which were characterized by output parameters. Data shown in Figure 8 typifies both the training and testing sets presented to the Neural Net. Recognition capability was evaluated by comparison of the NNA with that output derived from unlearned data sets. If variance from known values was greater than 45%, the Neural Net weights were modified by test results and additional training was performed.

Steps involved in NNA training and pattern recognition leading to the diagnosis of hidden corrosion sites may be summarized as follows:

- Select phase angle FFTEIS data collected during Task 2 for representative corrosion environments and relevant metal substrates shown in Table 1 as a function of their corrosion exposure time.

- Process input impedance data into the Neural Network by transforming and normalizing into a useful form.

- Present the processed impedance data to the Neural Network and assign desired

outputs for each pattern. Outputs reflected both the time and severity of hidden chemical corrosion on aircraft components in the corrosion environment.

- Impedance data were run through the Neural Network and results compared with the desired outputs.
- Adjustments were made to weights associated with each node and impedance data run through the Neural Network again. This step was repeated until the output of the Neural Network was reasonably close to the desired output, symptomatic of the presence or absence of hidden chemical corrosion on representative aircraft components.
- When the network was incapable of giving desired outputs, then the network architecture, configuration or number of inputs were changed. A primary modification required fewer hidden nodes and layers.
- The utility of the fully trained Neural Network was evaluated by testing predicted outputs with data from sets previously unknown to the network.

The above steps were applied to impedance phase angle shift data for samples previously shown in Table 1.

Sample 1) Al 7075/Al 2024 in 0.1M HNO_3 - Total Exposure 1308 Hours

In Figure 63, the Neural Network predicted phase angle peak centroids for hidden corrosion were incorporated with previous results shown in Figure 11. NNA results were obtained using experimental data after 50 hours exposure time due to initial surface roughening corrosion. A curve fit of FFTEIS phase angle peak and NNA predicted centroid positions are shown as solid and dashed lines respectively. These results showed that agreement between experimentally determined log-normal peak centroids and those predicted from NNA were found to be within 10% as shown in Figure 63.

Sample 2) Al 7075/Al 2024 in 0.1M H_2SO_4 - Total Exposure 1342 Hours

In Figure 64, Neural Network predicted phase angle peak centroids for hidden corrosion were incorporated with results shown in Figure 29. NNA results were obtained for exposure times greater than 50 hours due to initial surface roughening corrosion. A curve fit of FFTEIS phase angle peak and NNA predicted centroid positions are shown as solid and dashed lines respectively. NNA data were again within 10%.

Sample 3) Al 7075/Ti 15-3 in 0.1M H_2SO_4 - Total Exposure 1353 Hours

In Figure 65, Neural Network predicted phase angle peak centroids for hidden corrosion were incorporated with results shown in Figure 34. NNA results were obtained without considering FFTEIS cumulative exposure times less than 40 hours due to initial surface roughening corrosion. A curve fit of FFTEIS phase angle peak and NNA predicted centroid positions are shown as solid and dashed lines respectively. The NNA predicted

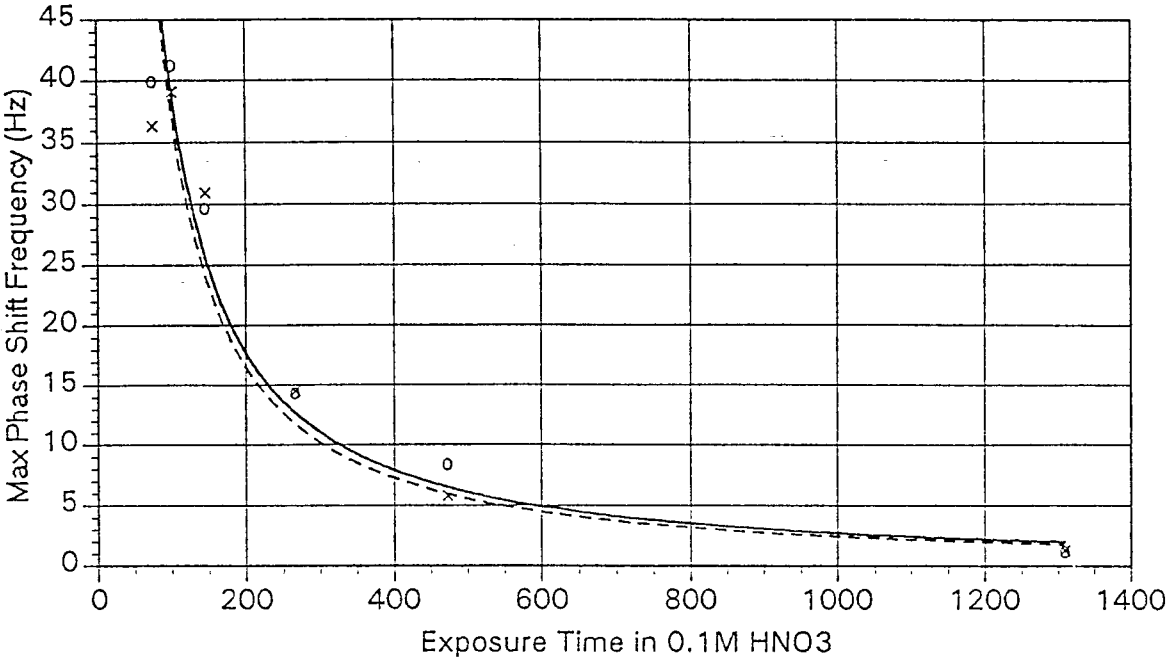

Figure 63. Comparison of experimental and NNA (dashed line) predicted position change of second log-normal peak centroid as exposure time increased for Al 7075/Al 2024 coupons in 0.1M HNO_3.

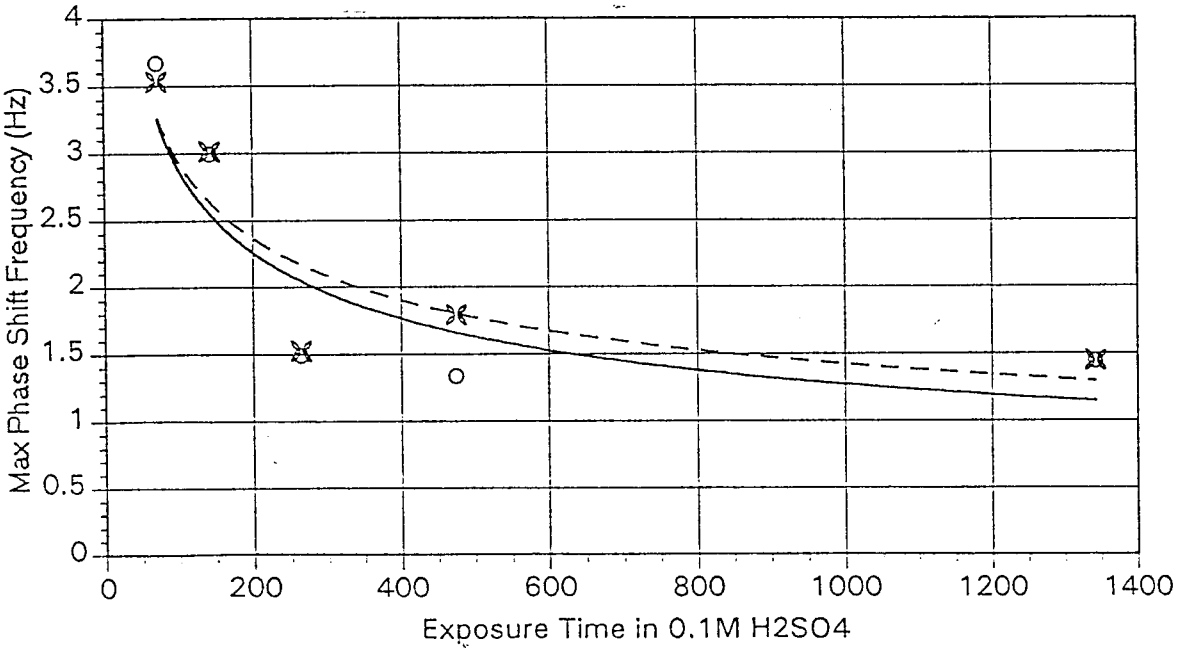

Figure 64. Comparison of experimental and NNA (dashed line) predicted position change of second log-normal peak centroid as exposure time increased for Al 7075/Al 2024 coupons in 0.1M H_2SO_4.

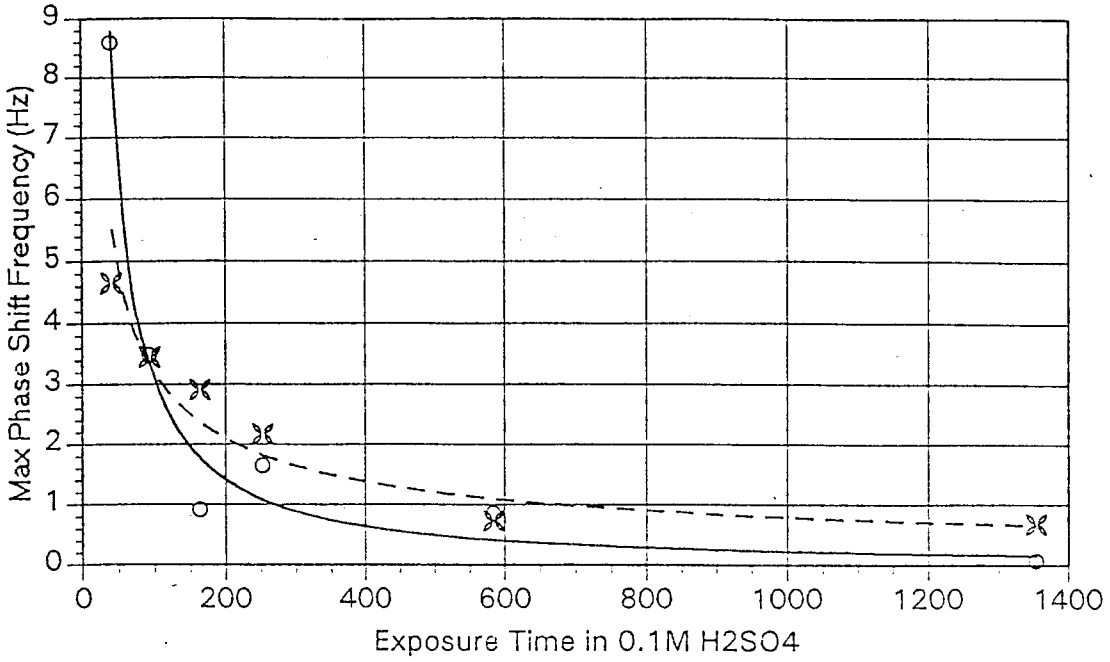

Figure 65. Comparison of experimental and NNA (dashed line) predicted position change of second log-normal peak centroid as exposure time increased for Al 7075/Al 2024 coupons in 0.1M H_2SO_4.

result was found to be in good agreement with experimental impedance data even though relatively large discrepancies in two data points in this figure the NNA identified a phase angle centroid position vs. time dependance which is common with all other data sets.

Sample 4) Al 2024/Ti 15-3 in 0.1M H_2SO_4 - Total Exposure 426.5 Hours

In Figure 66, Neural Network predicted phase angle peak centroids for hidden corrosion were incorporated with results shown in Figure 41. NNA results were obtained for FFTEIS cumulative exposure times greater than 25 hours due to initial surface roughening corrosion. A curve fit of FFTEIS phase angle peak and NNA predicted centroid positions are shown as solid and dashed lines respectively. NNA data were within experimental error at most time intervals.

Sample 5) Ti 15-3/Al 2024 in 0.1 M H_2SO_4 - Total Exposure 289.5 Hours

In Figure 67, Neural Network predicted phase angle peak centroids for hidden corrosion were incorporated with results shown in Figure 47. NNA results were obtained utilized FFTEIS cumulative exposure times greater than 25 hours due to initial surface roughening corrosion. A curve fit of FFTEIS phase angle peak and NNA predicted centroid positions are shown as solid and dashed lines respectively and are within 10%.

Sample 6) Ti 15-3/Al 7075 in 0.1M HNO_3 - Total Exposure 1412 Hours

In Figure 68, neural network predicted phase angle peak centroids for hidden corrosion were incorporated with results from Figure 55. NNA results were obtained using FFTEIS cumulative exposure times greater than 50 hours due to initial surface roughening corrosion previously discussed. A curve fit of FFTEIS phase angle peak and NNA predicted centroid

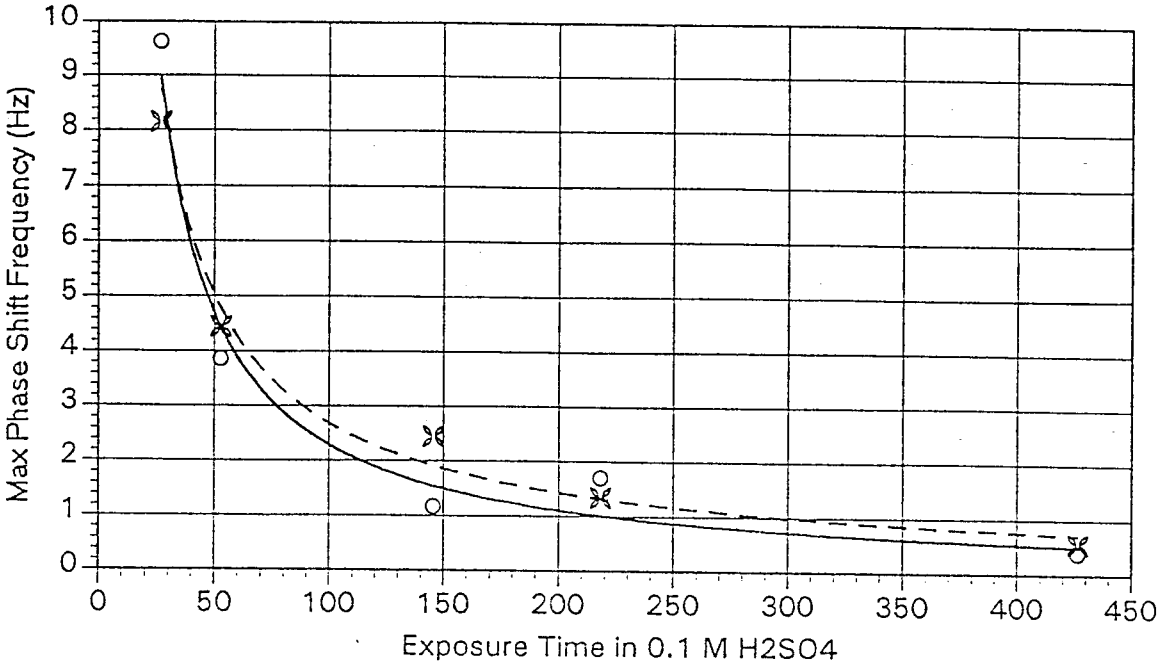

Figure 66. Comparison of experimental and NNA (dashed line) predicted position change of second log-normal peak centroid as exposure time increased for Al 2024 coupons in 0.1M H_2SO_4.

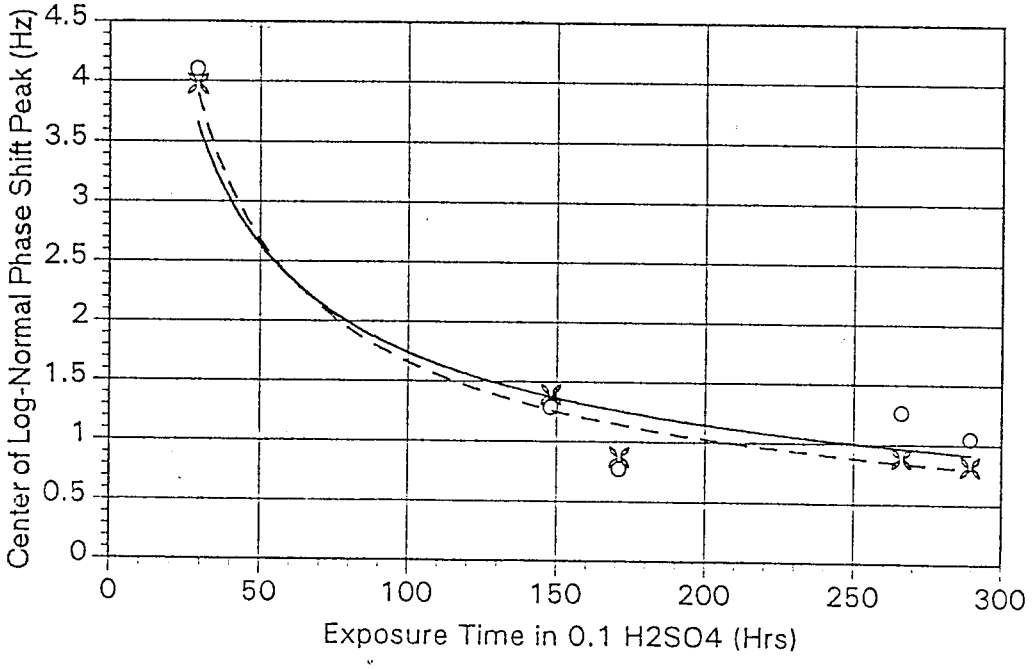

Figure 67. Comparison of experimental and NNA (dashed line) predicted position change of second log-normal peak centroid as exposure time increased for Ti 15-3/Al 2024 coupons in 0.1M H_2SO_4.

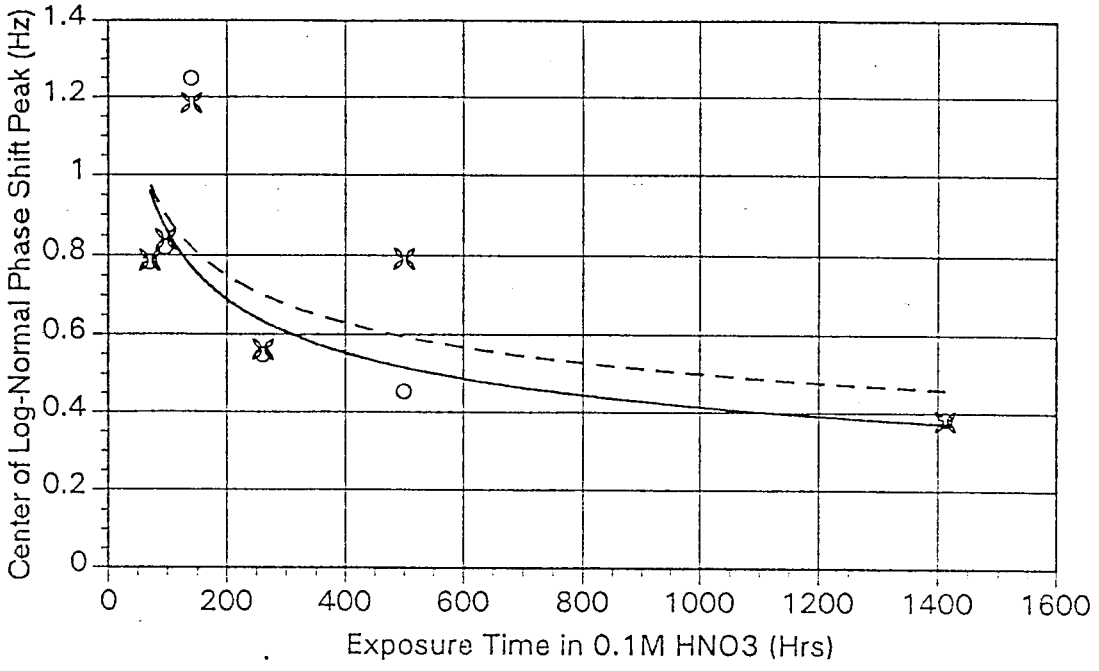

Figure 68. Comparison of experimental and NNA (dashed line) predicted position change of second log-normal peak centroid as exposure time increased for Ti 15-3/Al 7074 coupons in 0.1M HNO_3.

positions are shown as solid and dashed lines respectively. With the exception of one data point the NNA predicted phase angle peak centroid data clearly correlated to experimentally determined values.

Sample 7) Ti 15-3/Al 2024 in 0.1M HNO_3 - Total Exposure 1358 Hours

In Figure 69, neural network predicted phase angle peak centroids for hidden corrosion were incorporated with results from Figure 61. NNA results were obtained using FFTEIS cumulative exposure times greater than 40 hours due to initial surface roughening corrosion. A curve fit of FFTEIS phase angle peak and NNA predicted centroid positions are shown as solid and dashed lines respectively. As can be seen from this figure excellent agreement was found between experimental and predicted values.

An unequivocal correlation was observed between known and predicted values of impedance phase angle peak centroid shift as a function of corrosion exposure time for all samples evaluated. Each shows a progressive reduction in phase angle centroid frequency as hidden corrosion increased at the metal/metal interface. Differences between curves 63-69 reflect details of interfacial corrosion. Significant pitting was clearly indicated in Figure 63, 66 and 69 by the sharp change in phase angle peak centroid for early corrosion times. Significantly less hidden corrosion occurred for those samples represented by Figure 64, 65, 67, and 68. This was subsequently corroborated by SEM and EDX measurements.

Since backpropagation architecture was sensitive to the number of training sets used, agreement between known and predicted values was encouragingly close considering that only six data sets were used for each initial training set.

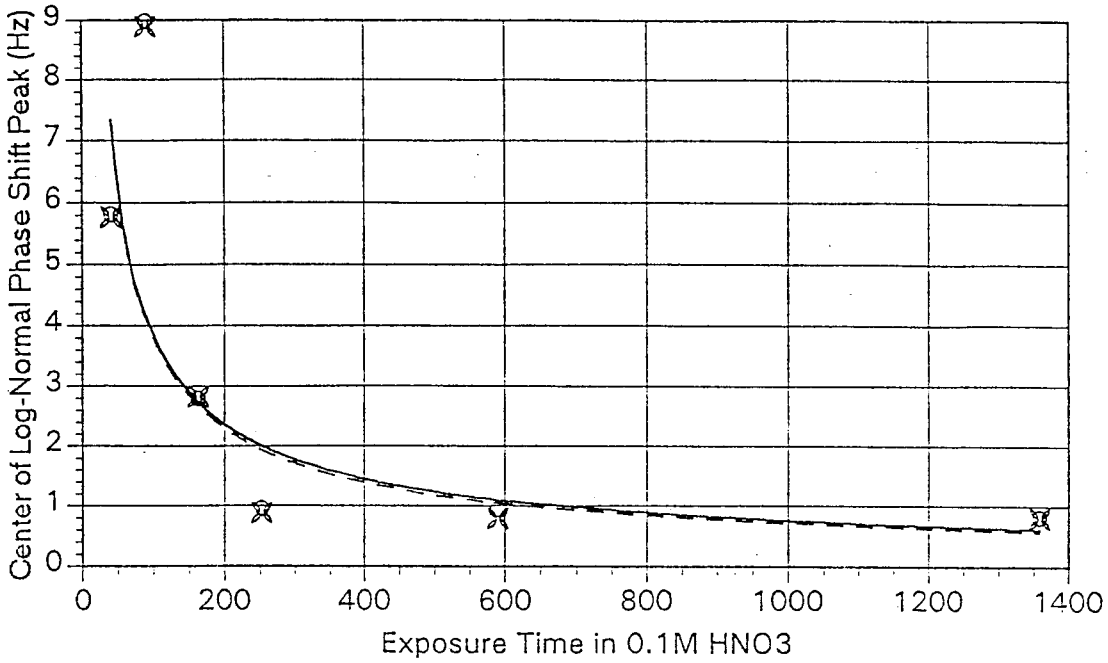

Figure 69. Comparison of experimental and NNA (dashed line) predicted position change of second log-normal peak centroid as exposure time increased for Ti 15-3/Al 7074 coupons in 0.1M HNO_3.

Task 4 Fabrication and Performance Testing of Prototype Instrumentation

The goal of this task was to integrate information gained and instrumentation developed in the previous three tasks into components of a prototype hardware and software system compatible with the reliable detection of hidden chemical corrosion. Overall implementation of prototype FFTEIS instrumentation involved a data acquisition and control card installed in a 486-33MHz MS-DOS based computer, a custom built potentiostat, and a custom signal conditioning circuit (schematically shown in Figure 70). A software control program was developed to coordinate hardware and acquire impedance data from corrosion samples, as previously shown in Figure 8. Hardware coordination proceeded by development and application of the pseudo-white noise signal through the potentiostat to the corrosion cell. Current and voltage signals were acquired by the control program through the potentiostat by means of the data acquisition card. Subsequent FFT of the time domain signals developed phase angle shifts as a function of frequency. NNA operated on those results to learn and predict corrosion severity at metal/metal interface under study.

An ADA3100 Real Time Devices data acquisition and control card (installed in the 486-33MHz computer) was used to apply the pseudo-white noise signal and to acquire resulting current and voltage signals. A custom potentiostat, designed and built at Eltron Research, Inc. (Eltron) provided three input lines. Two of these had active low-pass filters and one was buffered and thereby unrestricted by frequency response. The pseudo-white noise excitation signal was applied to one of those inputs and converted from 10V peak to peak to 10mV peak to peak and then applied to the electrochemical impedance cell. The

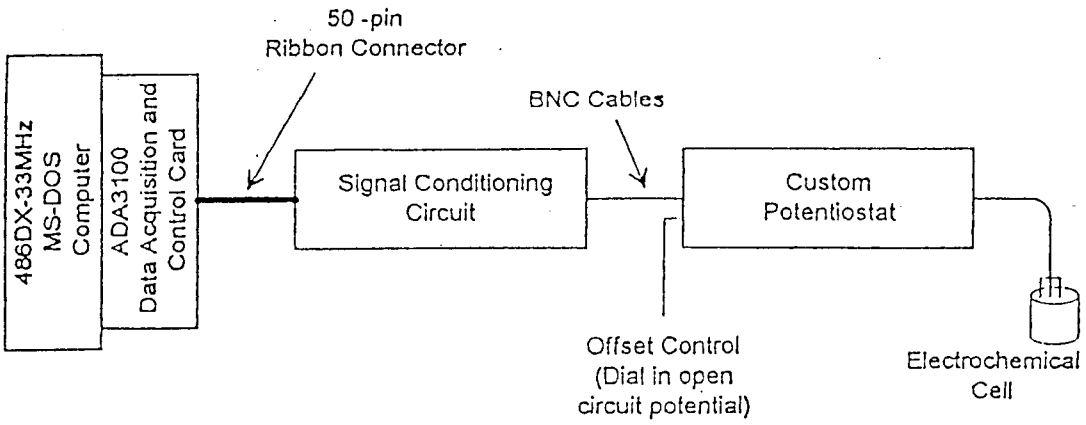

Figure 70. Schematic overall implementation of prototype FFTEIS instrumentation performed during Phase I for detection of hidden corrosion and grading its severity.

other input was used to apply a DC offset, approximately equal to the rest potential voltage of the electrochemical impedance cell. Current preamplification was controlled by digital lines from the ADA3100 board. The electrochemical impedance cell time domain response was defined by the potentiostat and provided to the data acquisition board. Current and voltage signals from the potentiostat were interfaced to the custom signal conditioning circuit.

The current signal was first amplified and then passed through the 6 pole low pass Bessel filter. The Bessel filter design was chosen for its linear phase characteristics and designed to provide four cut off frequencies. The voltage signal was also amplified and in addition the DC offset introduced earlier was subtracted through a precision differential amplifier. This voltage signal was passed through the previously discussed 6 pole low pass Bessel filter. Current and voltage signals were read by the ADA3100 board.

Overall fabrication of FFTEIS instrumentation was in components. These consisted of i) the computer installed ADA3100 data acquisition card, ii) signal conditioning circuit, iii) the Eltron built potentiostat, and iv) appropriate component to component interface.

The general procedure used for operating this instrumentation will now be discussed. The control program generated and stored a lookup table for the pseudo-white noise. Initial conditions for the ADA3100 timing circuit established DC offset voltage and appropriate voltage and current ranges. The interrupt service routine was then initialized and started by the timing circuit. Each time the interrupt service routine was called, a value from the lookup table was selected and applied to the D/A. After a few microseconds a pair of current and voltage readings were acquired and stored in the FIFO memory. The interrupt service routine was allowed to continue until the whole set of pseudo-white noise data was used for excitation of the hidden corrosion site. FIFO memory was transferred to computer memory away and subsequently processed through the FFT subroutine. Results were plotted on screen and saved in a hard disk file. This data was later retrieved and passed through a Neural Network program for pattern recognition of potential hidden corrosion sites where the presence and severity of corrosion were predicted. The general processing sequence for prototype instrumentation developed during Phase I is shown in Figure 71.

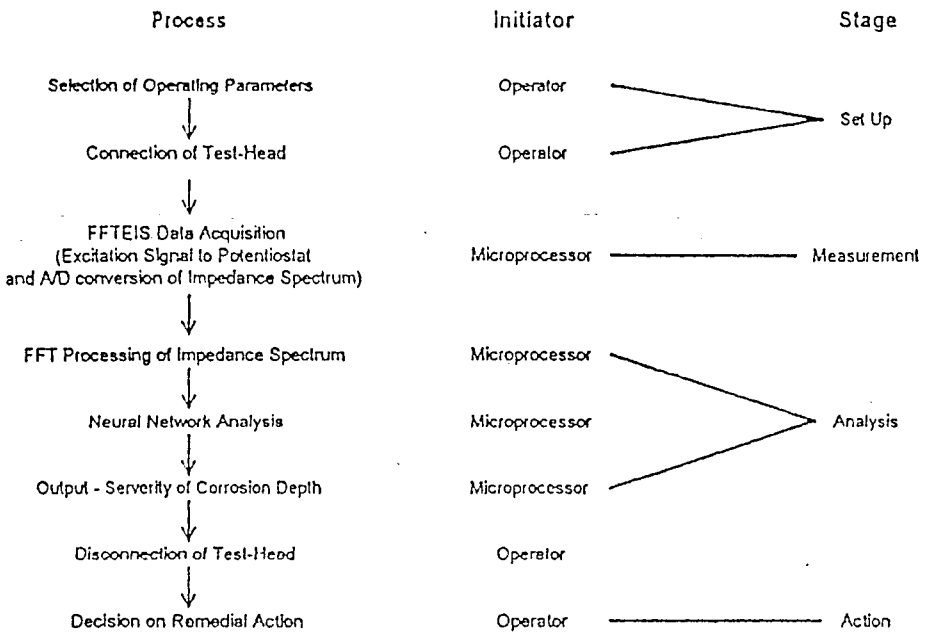

Figure 71. Prototype instrumentation processing sequence applied during Phase I for hidden corrosion detection and determination of corrosion severity.

Work performed in this task resulted in fabrication, assembly, test and performance verification of a prototype instrument component system for both the detection of hidden corrosion and predicting severity on simulated aircraft substrates. Feasibility demonstration has shown that this technology will be applicable to in-service aircraft corrosion maintenance for Air Force and FFA applications.

IV. ESTIMATES OF TECHNICAL FEASIBILITY

Work performed during this Phase I program unequivocally demonstrated that the simultaneous application of FFTEIS and subsequent analysis of impedance patterns by NNA pattern recognition schemes was particularly powerful for detecting the presence and grading the severity of hidden corrosion present on the aircraft metal substrate interface of interest. Furthermore since all corrosion phenomenon are electrochemical in nature it is recognized that this technique will also facilitate fundamental insights into the nature of corrosion processes at such sites and into their origin. The intrinsic features of instrumentation characterized in this program compatible with performing the NDE of hidden chemical corrosion with a high degree of accuracy, sensitivity and versatility on both titanium and aluminum alloys currently used in Air Force and commercial aircraft has previously been enumerated in the Introduction, Section B (page 6).

Work performed in this Phase I program which supports technical feasibility for this technology may be summarized as follows:

- Preferred Fast Fourier Transform Electrochemical Impedance Instrumentation hardware and software was demonstrated compatible for non-destructive, *in situ* time

dependent, quantitative and qualitative analysis of hidden corrosion processes which included:

1) Identification of and distinguishing between corrosion mechanisms.

2) Determination of corrosion rates.

3) Effect of materials, configurations and environments at the microscale.

- Preferred instrumentation hardware and software components were identified and incorporated into a Fast Fourier Transform Electrochemical Impedance Spectrometer compatible for the real-time unambiguous detection and quantification of hidden chemical corrosion in aircraft components.

- Electrochemical impedance spectra were obtained from selected metal substrate interface subjected to representative hidden corrosion environments.

- Clear correlations were found between exposure time to corrosion media and measured electrochemical impedance phase angle peak centroids which were shifted to lower frequencies for increased hidden corrosion severity.

- Clear correlations between impedance measurements and corrosion depth were verified by subsequent SEM examination of the hidden corrosion interfacial regions.

- Neural Net Analysis of FFTEIS data was verified as a powerful diagnostic strategy for *in situ* hidden corrosion process identification, quantitative analysis and severity grading.

- The approach was also shown to be compatible with gaining fundamental information into the nature of corrosion processes and conditions leading to their inception at hidden sites.

- Instrumentation components designed and developed during this program were combined into a prototype hardware and software system and their performance verified for the subject application.

- The original viability of this instrumentation for the on-site *in situ* detection of hidden corrosion on aircraft substrates for lifetime prediction was unequivocally determined.

IV. REFERENCES

1. N.J.E. Dowling, M. Franklin, D.C. White, C.H. Lee and C. Lundin, Corrosion/89, Paper #187.
2. N.J.E. Dowling, E.E. Stansbury, D.C. White, S.W. Borenstein and J.C. Danko, Microbial Corrosion, 1988 Workshop Proceedings, p. 5-17, Palo Alto, CA (1988).
3. F. Mansfeld, C.H. Tsai, H. Shih, B. Little, R. Ray and P. Wagner, Corrosion/90.
4. F. Mansfeld, H. Shih, J. Electrochem. Soc., 135, 1171 (1988).
5. P. Horowitz and W. Hill, The Art of Electronics, Cambridge University Press, NY (1989).

6. D.E. Smith, Crit. Rev. Anal. Chem., 2, 247 (1971).
7. F. Mansfeld and W.J. Lorenz, Electrochemical Impedance Spectroscopy (EIS): Application in Corrosion Science and Technology, 12, 581 in Techniques for Characterization of Electrodes and Electrochemical Processes, Edited by R. Varma and J.R. Selman, John Wiley & Sons, Inc. (1991).
8. G. Doetsch, Anleitung zum prakitschen Gebrauch der Laplace-Transformation. Oldenburg-Verlag, München-Wien (1967).
9. O. Föllinger, Laplace-und Fourier-Transformation. AEG-Telefunken, Berlin-Frankfurt (1982).
10. S.C. Creason and D.E. Smith, J. Electroanal. Chem. 36, Appl. 1 (1972).
11. S.C. Creason, J.W. Hayes, and D.E. Smith, J. Electroanal. Chem. 47, 9 (1973).
12. C. Gabrielli, F. Huet, M. Keddam, and J.F. Lizee, J. Electroanal. Chem. 138, 201 (1982).
13. N.D. Cogger, The Measurement of Low Amplitude Signals Resulting from the Study of Electrochemical Phenomena, Tech. Rep. No. 012/84. Solartron Instrument Group, Solartron Schlumberger, Farnborough, U.K.
14. D.E. Smith, Anal. Chem., 48, 221A (1976).
15. R.J. Schwall, A.M. Bond, R.J. Loyd, J.G. Larsen and D.E. Smith, Anal. Chem., 49, 1797 (1977).
16. R.J. Schwall, A.M. Bond and D.E. Smith, Anal. Chem., 49, 1805 (1977).
17. R. DeLevie, J.W. Thomas and K.M. Abbey, J. Electroanal. Chem., 62, 111 (1975).
18. J. Ühlken, R. Waser and H. Wiesl, Ber. Bunsenges, Phys. Chem., 92, 730 (1988).
19. J.W. Cooley and J.W. Tuckey, Math. Comput., 19, 297 (1965).
20. S.C. Creason, J.W. Hayes and D.E. Smith, J. Electroanal. Chem., 9, 47 (1973).
21. J.C. Hubert and D. Hubert, Circuit Cellar Ink, February/March (1990), p. 21-29.
22. J. Bittman, Dr. Dobb's Journal, May, 30 (1991).
23. W.P. Jones and J. Hoskins, Byte, Oct., 155 (1987).
24. M. Valley, J. Genin, and W. Xu, Coherent Optical Based Inspection of Aging Aircraft, June (1993).
25. S. Krishnaswamy, B. Pouet, and T. Chatter, Robust Optical Interferometers for Nondestructive Evaluation of Disbonds in Adhesively Bonded Structures. Draft Interim Report, January (1993).
26. L.D. Favro, P.K. Kuo, R.L. Thomas, T. Ahmed, X. Han, and X. Wang, Progress in the Development of Pulse-Echo Thermal Wave Imaging for NDE.
27. D. Thompson and D. Chimenti Review of Progress in Quantitative NDE, Vol. 13, (eds), Plenum Press, to be published.
28. J. Ting, T. Jensen, and J.N. Gray, Quantitative Determination of Material Composition of Composites Using Energy Sensitive X-Ray Measurements. Review of Progress in Quantitative Nondestructive Evaluation, Vol. 11b, D.O. Thompson and D.E. Chimenti (eds) Plenum Publishing Co., p.1499, (1992).
29. L. Lawson, Measurement of Layered Corrosion with Compton Backscatter. Review of Progress in QNDE, Vol. 12, D.O. Thompson and D.E. Chimenti (eds) Plenum, New York, p.1971, (1993).
30. D.K. Hsu, M.S. Hughes, and T.C. Patton, Ultrasonic Scans Using Low Frequency Unresolved Echoes, Review of Progress in Quantitative Nondestructive Evaluation, Vol. 12, D.O. Thompson and D.E. Chimenti (eds) Plenum Press, New York, p.1595-1602, (1993).

31. D.K. Hsu and T.C. Patton, Development of Ultrasonic Inspection for Adhesive Bonds in Aging Aircraft, Material Evaluation, Vol. 15, No. 12, December (1993).
32. T.C. Patton, Low Frequency Ultrasonic Nondestructive Inspection of Aluminum/Adhesive Fuselage Lap Splices, Master's Thesis, Iowa State University, Ames, Iowa, December (1993).
33. I.N. Komsky and J.D. Achenbach, Application of a Self-Calibrating Ultrasonic Technique to the Detection of Fatigue Cracks by the Use of Lamb Waves. Review of Progress in NDE, D.O. Thompson and D.E. Chimenti (eds) Vol. 12B, pp.2167-2174, Plenum Press, (1993).
34. A.D. Hibbs and R. Chung, Evaluation of High-Sensitivity Magnetic Imaging for the Detection of Hidden Corrosion, Draft Final Report, Contract No. DTRS-ST-92-C-00095, September (1993).
35. S. Mitra, P. Urali, E. Uzal, J.H. Rose, and J.C. Moulder, Eddy Current Measurements of Corrosion-Related Thinning in Aluminum Lap Splices, Review of Progress in Quantitative NDE, D.O. Thompson and D.E. Chimenti (eds) Vol. 12b, Plenum, New York, 2003 (1992).
36. D.K. Thome and G.L. Fitzpatrick, Detection and Quantification of Subsurface Corrosion Using Improved Magneto-Optic/Eddy-Current Imaging and Image Processing, Final Report, Contract DTRS-57-93-C-0006, February, (1993).

VI. APPENDIX
SEM, EDX and Impedance Measurements Performed on Samples During this Program

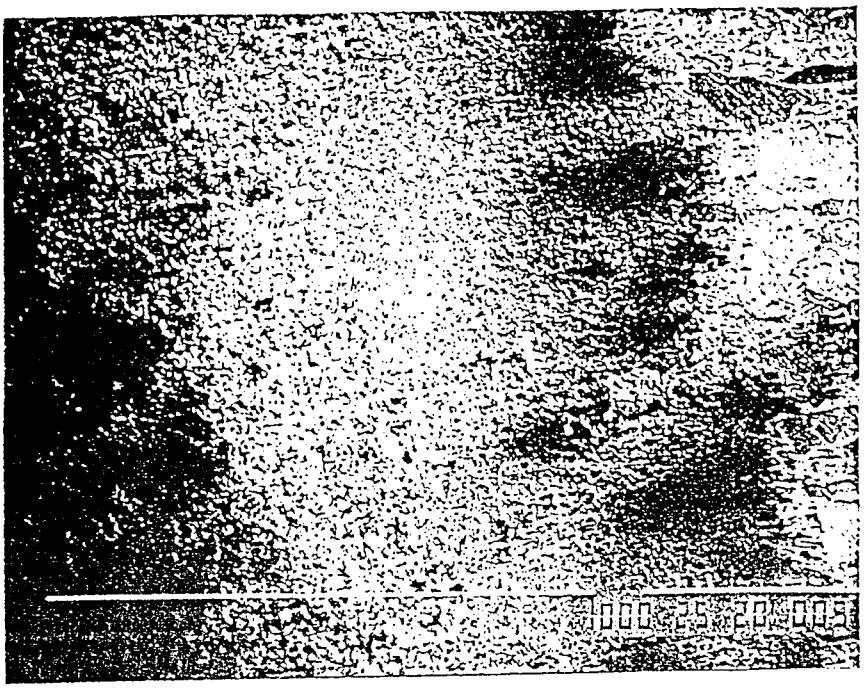

Figure 18. Scanning electron micrograph of Al 2024 coupon after exposure to 1308 hours in 0.1M HNO_3 at Al 7075/Al 2024 interface. Plateau structures are typical of crevice corrosion attack. Corrosion product shown at the right consisted of nitrates. Dimension shown = 1000 microns.

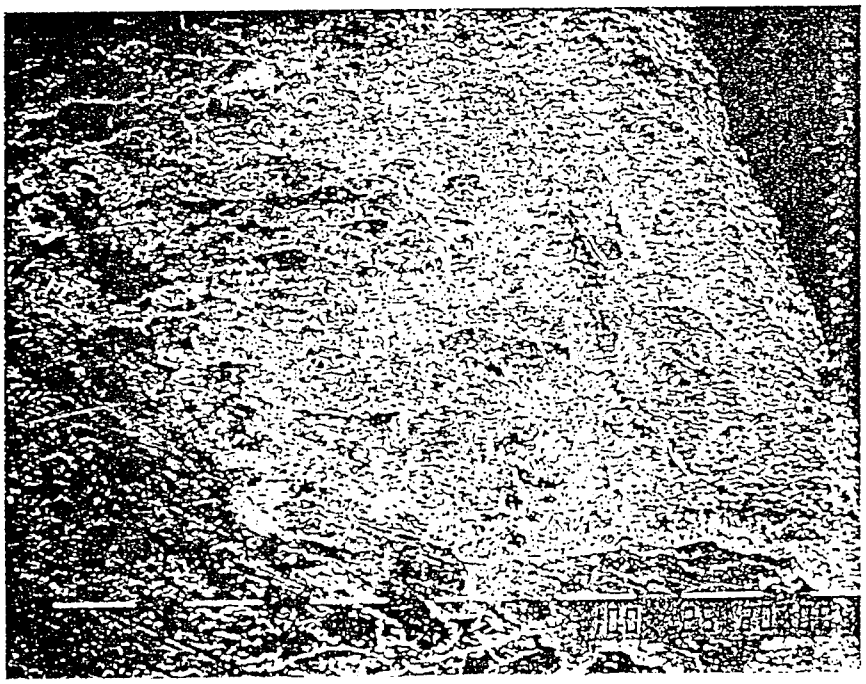

Figure 19. Scanning electron micrograph of Al 2024 coupon after 1308 hours exposure to 0.1M HNO_3 at Al 7075/Al 2024 interface and at Al 7075/Al 2024 interface and at the Al 2024/Torr Seal interface. Edge rounding at the Al 2024/Torr Seal interface shown at right side of Figure. Dimension shown = 100 microns.

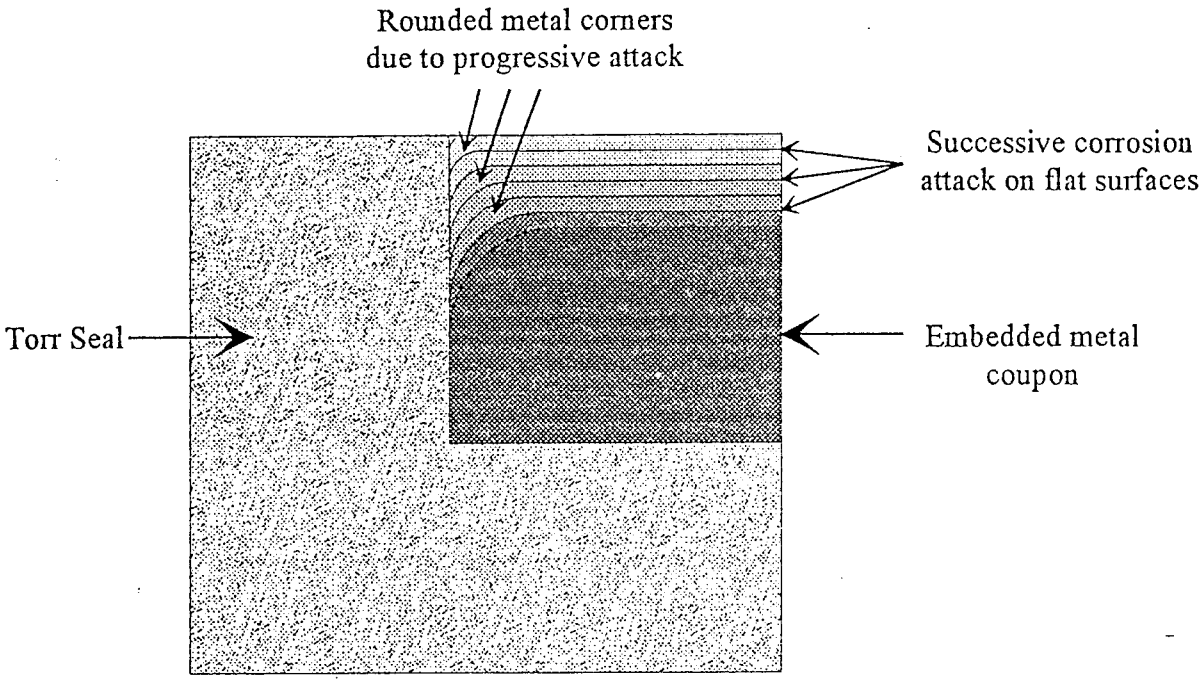

Figure 20. Schematic illustration of rounding at the Torr Seal/coupon interface due to progressive attack from corrosion solution.

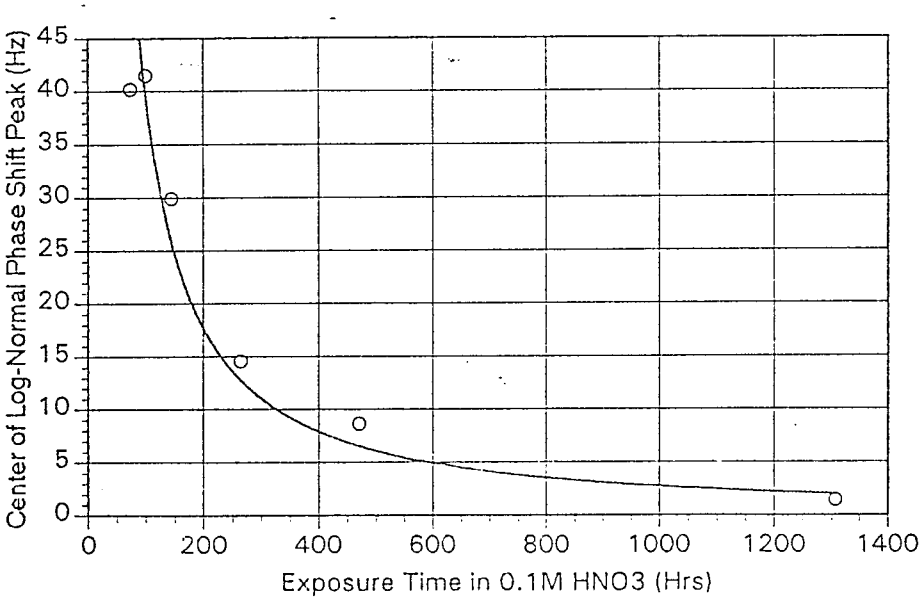

Figure 21. Position change of log-normal peak centroid as a function of exposure time in 0.1M HNO_3 for Al 7075/Al 2024. Only data from time intervals after 50 hours included.

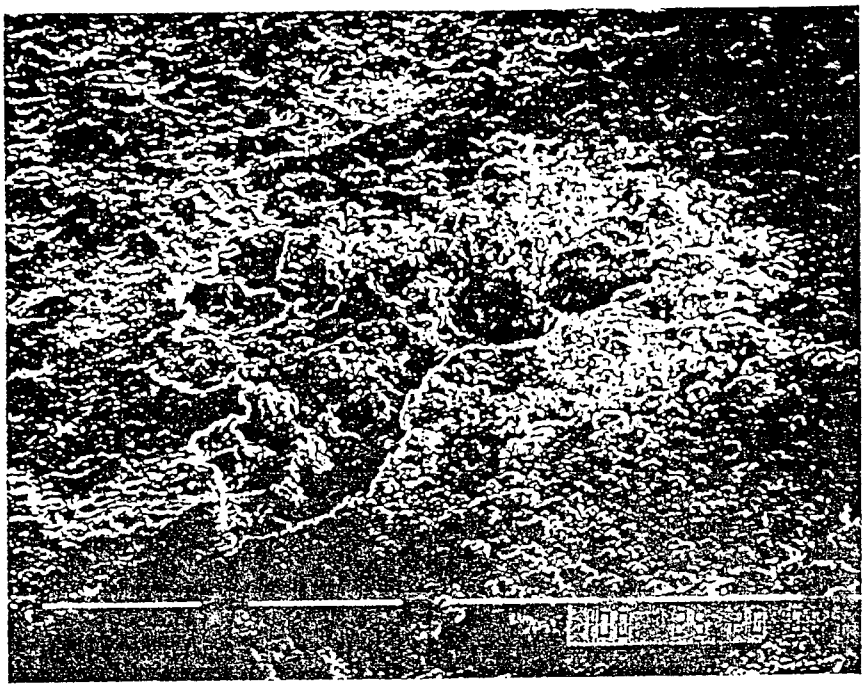

Figure 22. Scanning electron micrograph of Al 7075 coupon after 1342 hours exposure in 0.1M H_2SO_4 at Al 7075/Al 2024 interface. Surface roughening and corrosion product respectively observed at left and right of central pit. Dimension shown = 100 microns.

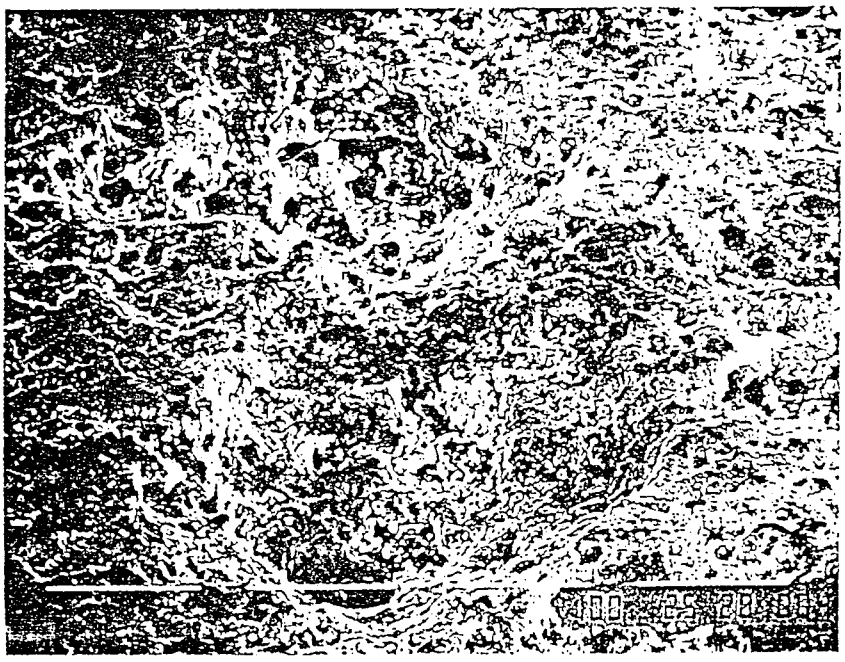

Figure 23. Scanning electron micrograph of Al 2024 after 1342 hours exposure in 0.1M H_2SO_4 at Al 7075/Al 2024 interface. Corrosion product obscured the roughened surface in the region of this pit. Dimension shown = 100 microns.

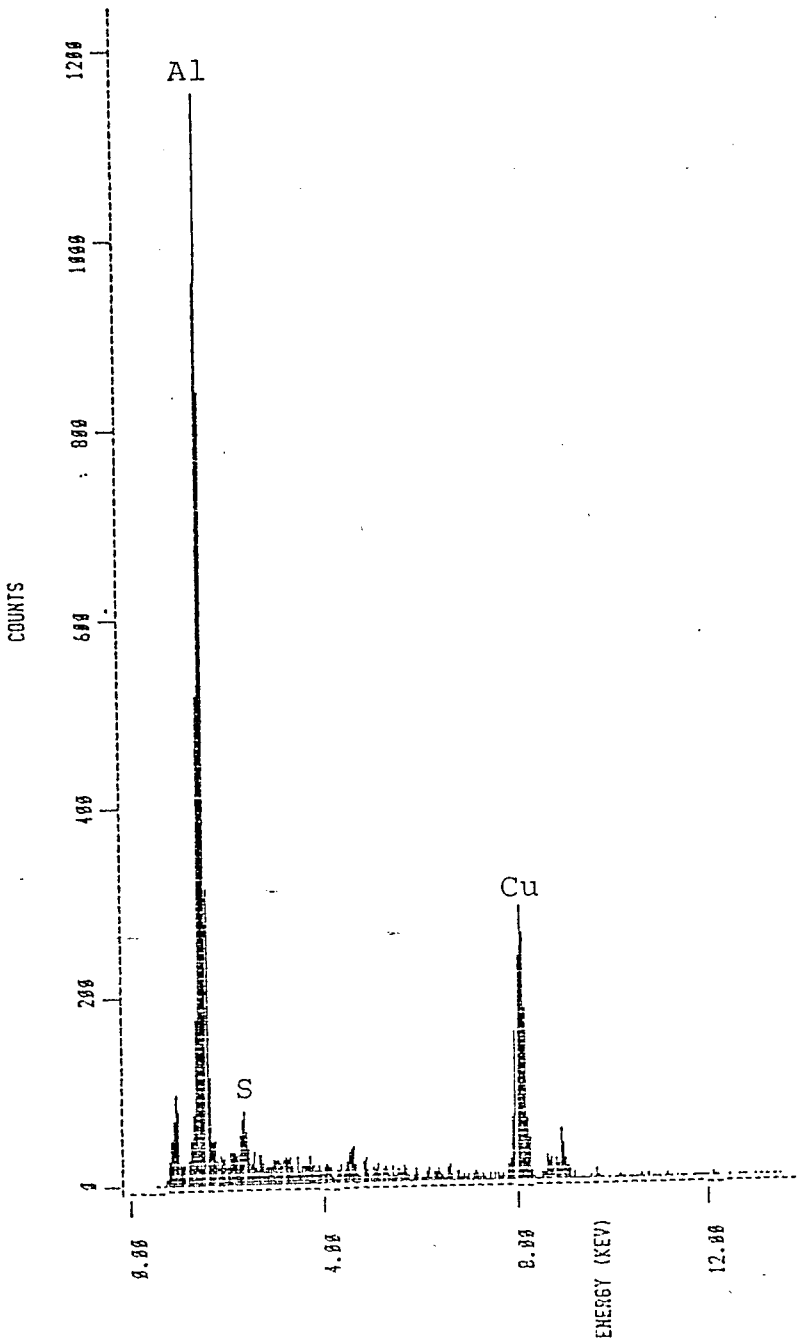

Figure 24. EDX spectrum of corrosion product on Al 7075 coupon after 1342 hours exposure in 0.1M H_2SO_4 at Al 7075/Al 2024 interface. SEM of corrosion product shown in Figure 22.

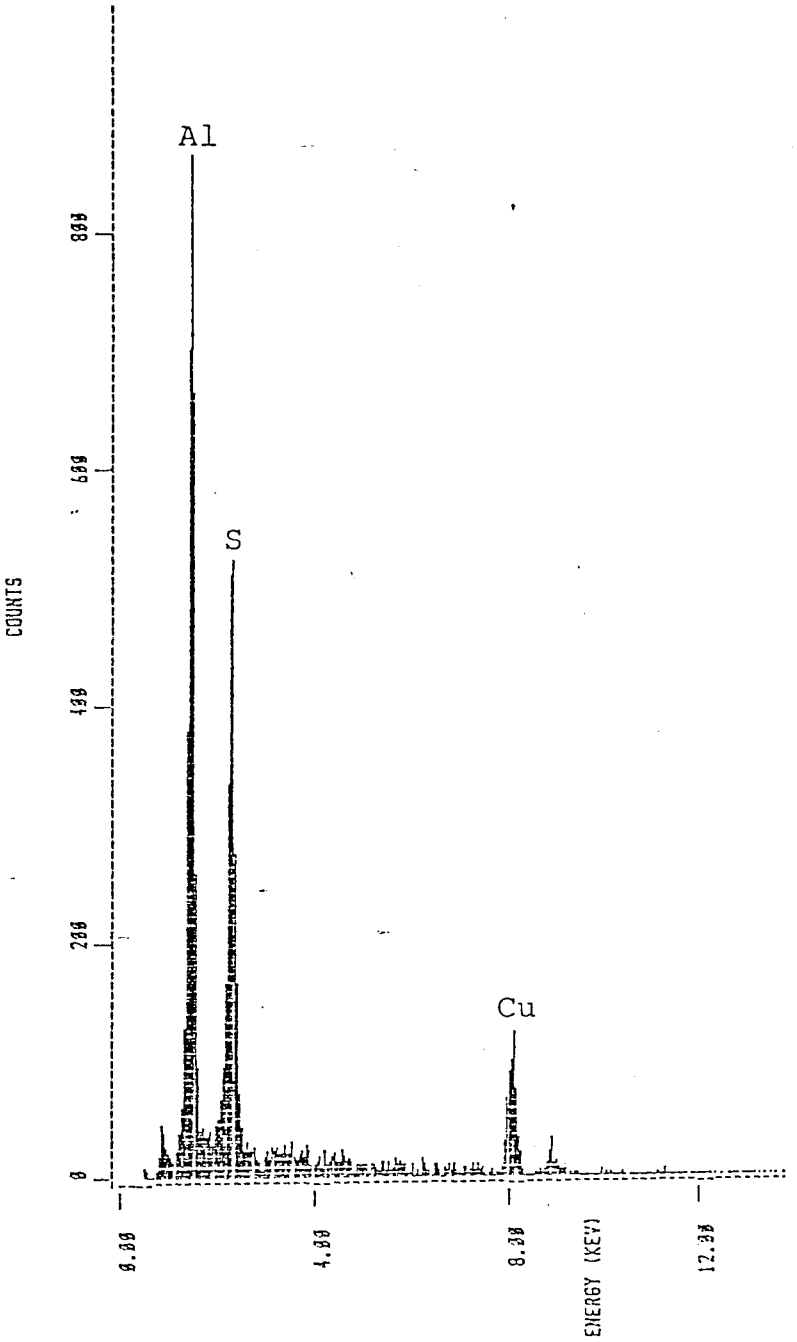

Figure 25. EDX spectrum of corrosion product on Al 2024 coupon after 1342 hours exposure in 0.1M H_2SO_4 at Al 7075/Al 2024 interface. SEM of corrosion product shown in Figure 23.

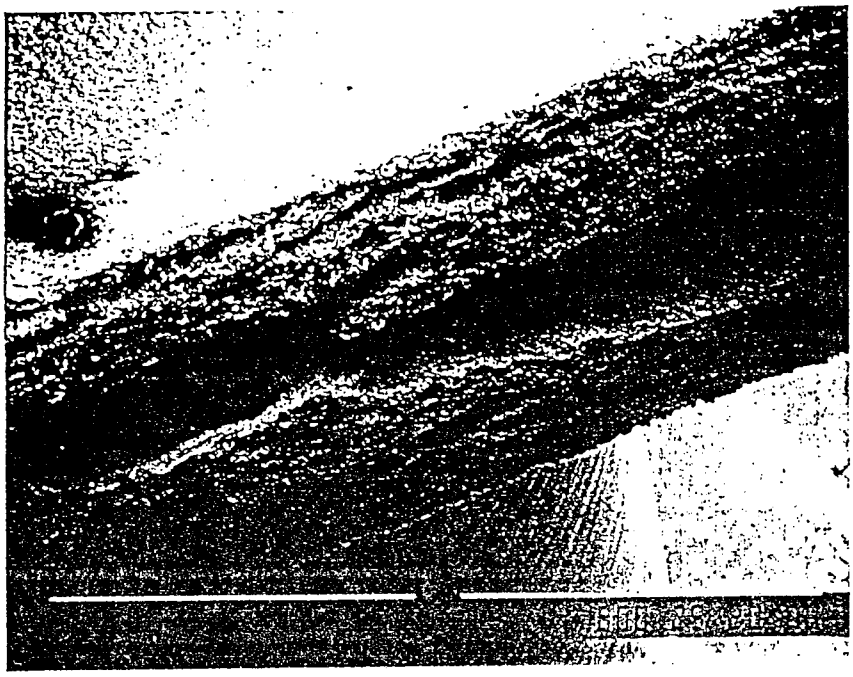

Figure 26. Scanning electron micrograph of Al 7075 coupon after 1342 hours exposure in 0.1M H_2SO_4 to vertical edge, originally 0.16 cm thick. The large pits parallel to the interfacial surfaces reduce coupons thickness to 50%. Dimension shown = 1000 microns.

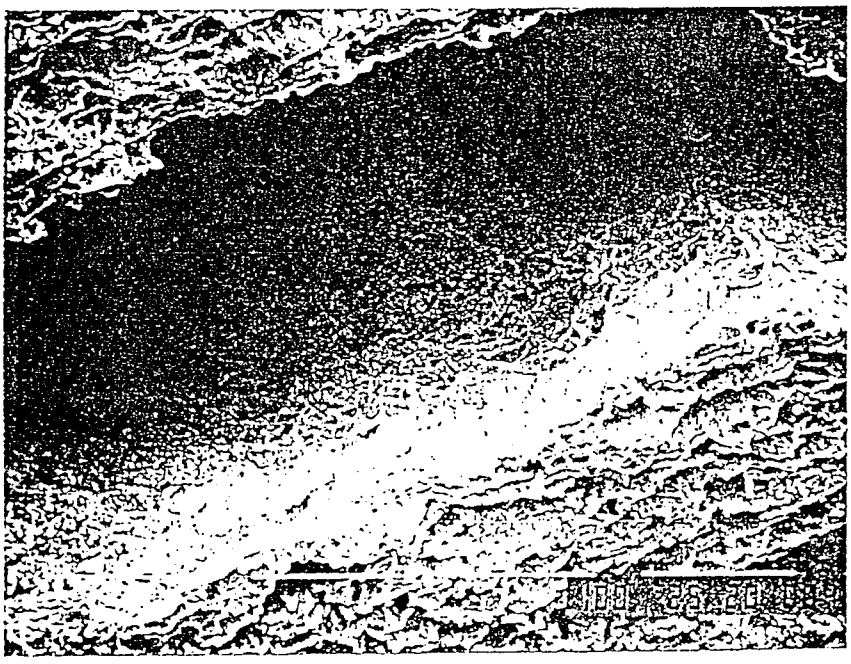

Figure 27. Scanning electron micrograph of Al 7075 after 1342 hours exposure to 0.1M H_2SO_4 to vertical edge. Width of pit in this enlargement of Figure 26 was 500 microns. Dimension shown = 100 microns.

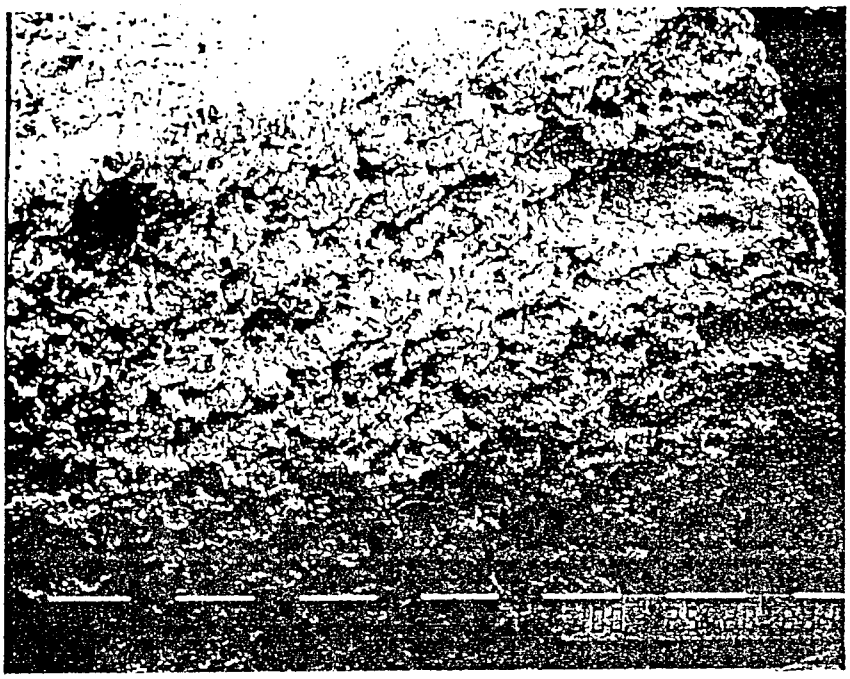

Figure 28. Scanning electron micrograph of Al 2024 coupon after 1342 hours exposure to 0.1M H_2SO_4 at vertical edge, originally 0.16 cm thick. Dimension shown = 100 microns.

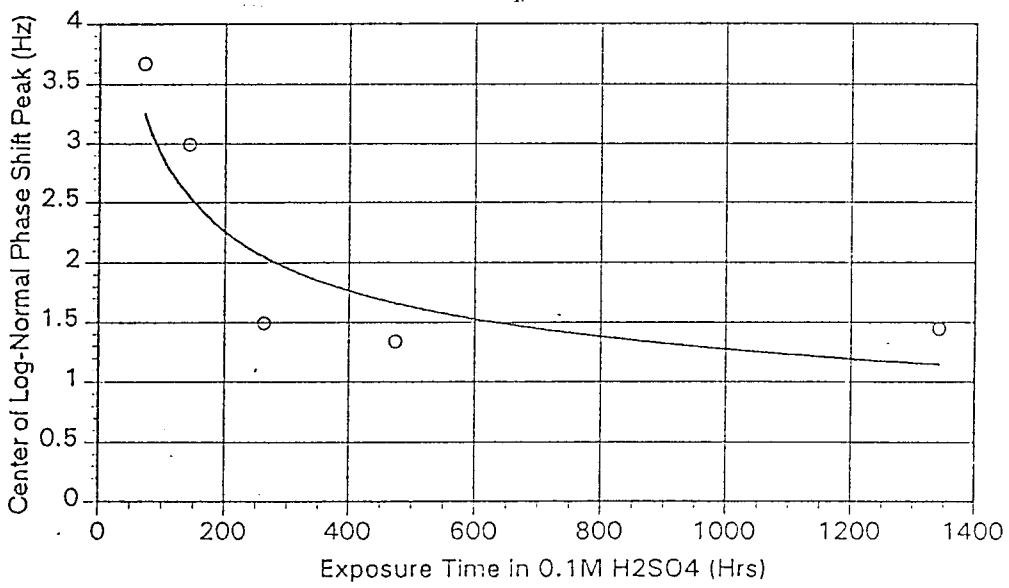

Figure 29. Position change of log-normal peak centroid as a function of exposure time in 0.1M H_2SO_4 for Al 7075/Al 2024. Only data from time intervals after 50 hours included.

A)

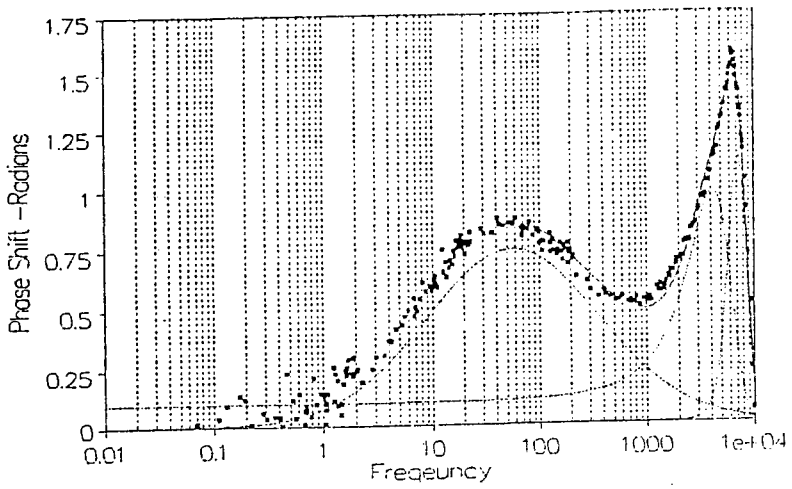

B)

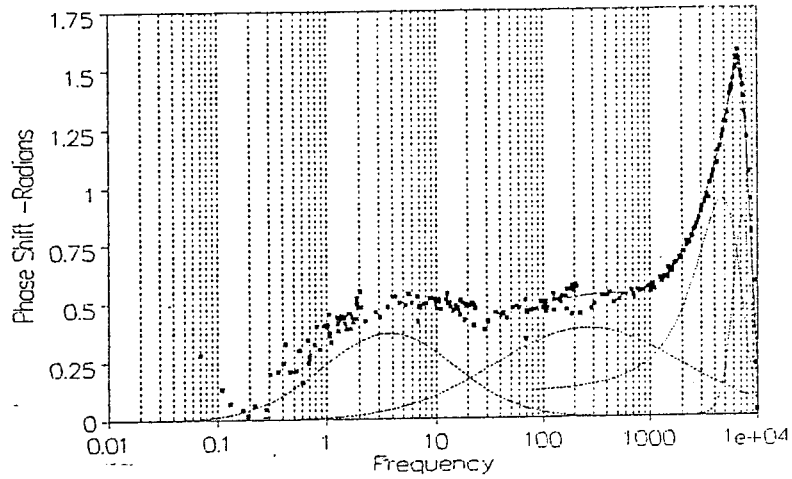

C)

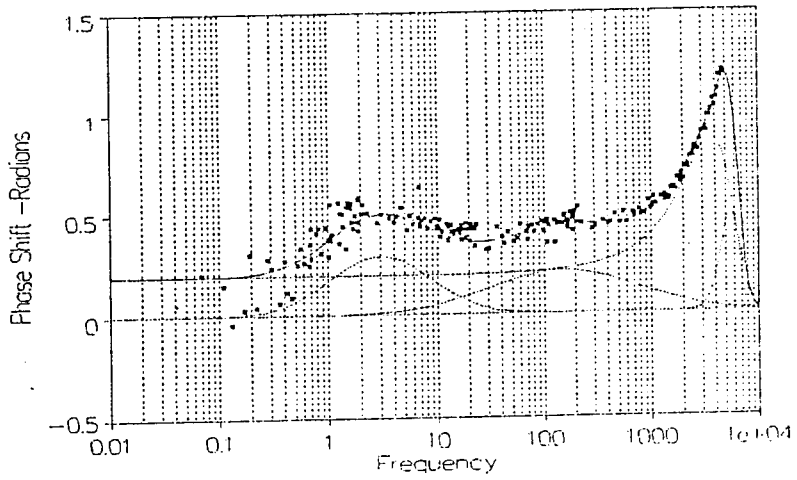

Figure 30 (A, B and C).
FFTEIS measured phase angle dependency on frequency for Al 7075/Al 2024 interface exposed to 0.1M HNO_3 after A) 4 hours, B) 72 hours, and C) 143 hours. Best fit log-normal curves shown over 0.1 to 1000 Hz range.

D)

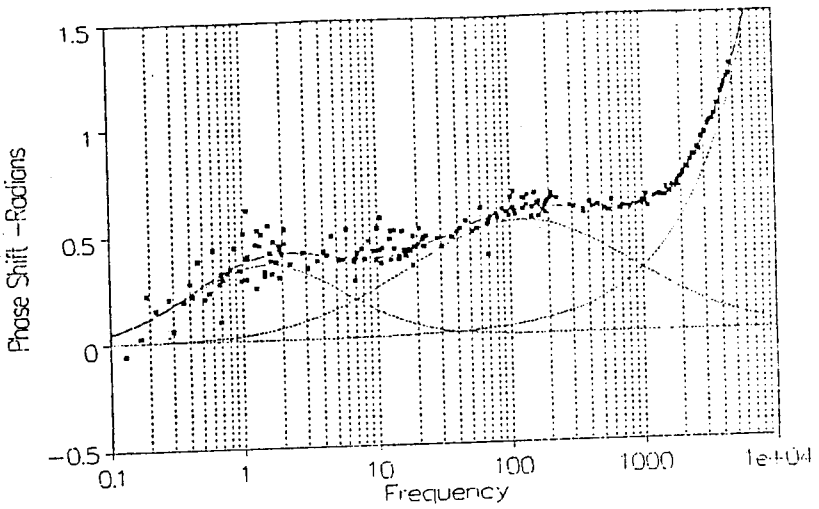

E)

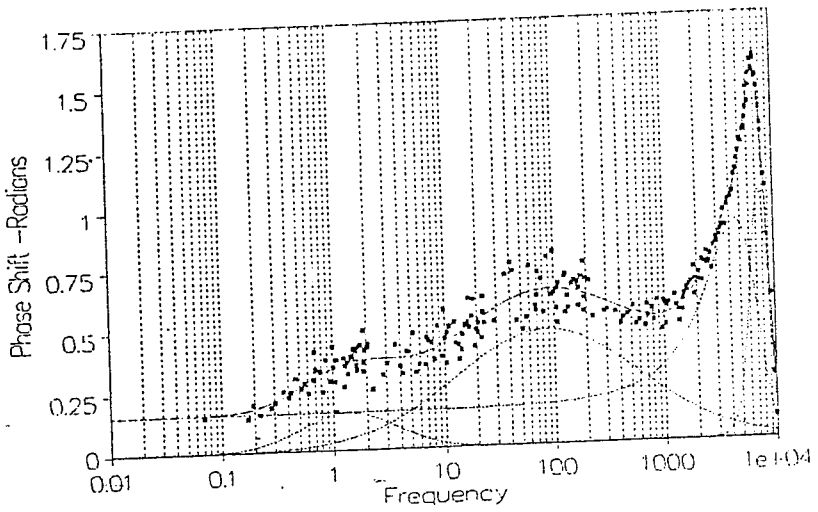

F)

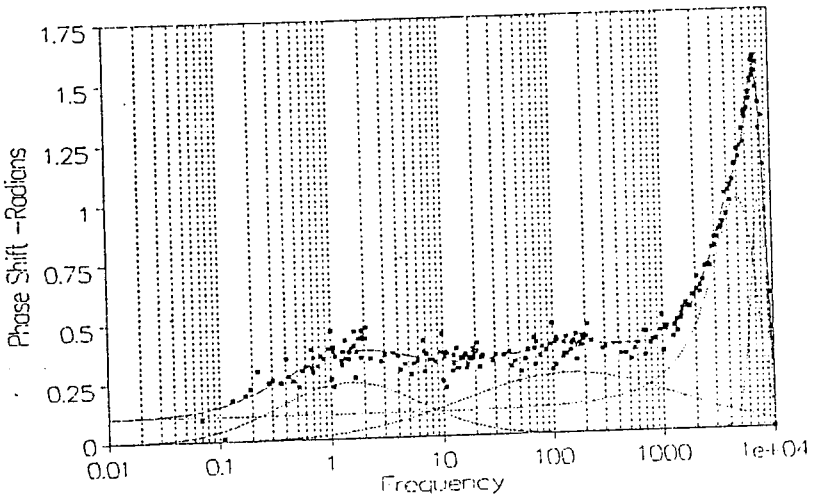

Figure 30 (D, E and F).

FFTEIS measured phase angle dependency on frequency for Al 7075/Al 2024 interface exposed to 0.1M HNO_3 after D) 263.5 hours, E) 474.5 hours, and F) 1342 hours. Best fit log-normal curves shown over 0.1 to 1000 Hz range.

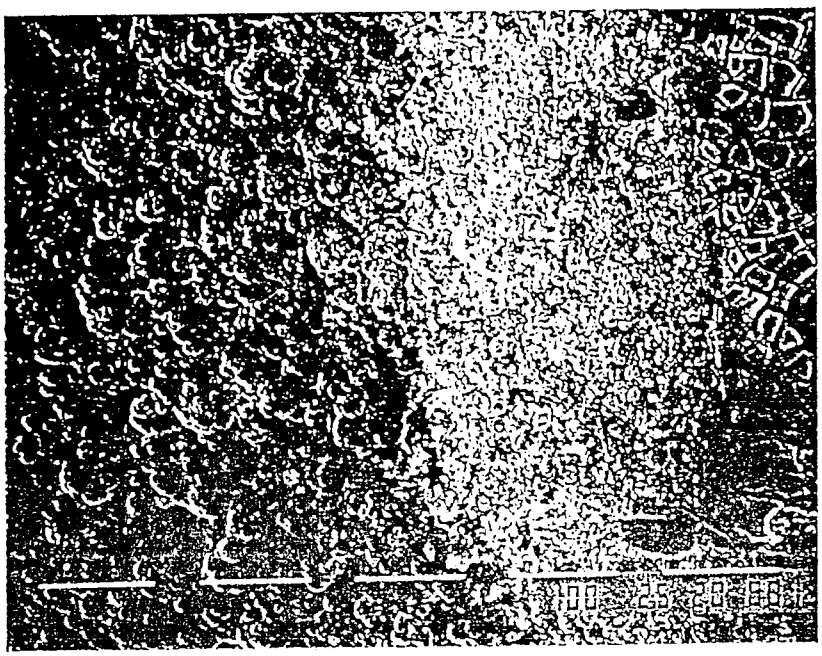

Figure 31. Scanning electron micrograph of Al 7075 coupon after 1353 hours exposure to 0.1M H_2SO_4 at Al 7075/Ti 15-3 interface. Metal removed on left, metal roughened in center and corrosion product at right of Figure. Dimension shown = 100 microns.

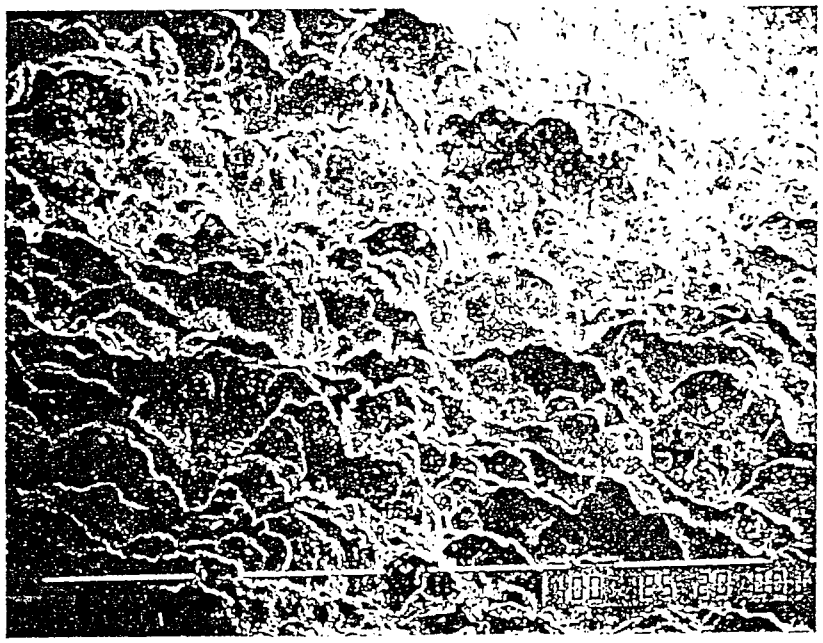

Figure 32. Scanning electron micrograph of Al 7075 after 1353 hours exposure to 0.1M H_2SO_4 at vertical edge, originally 0.16cm thick. Average pit size in 35 microns. Dimension shown = 100 microns.

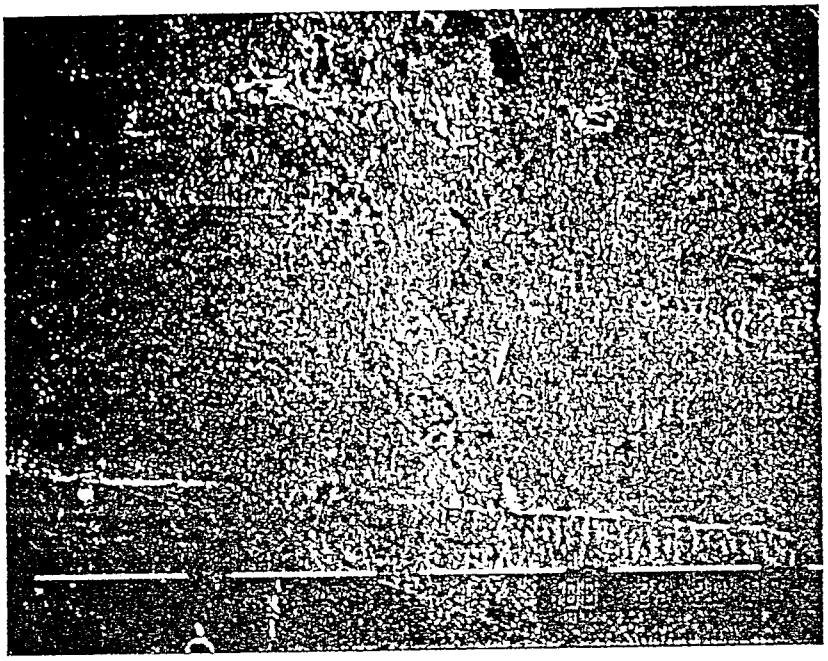

Figure 33. Scanning electron micrograph of Ti 15-3 coupons after 1353 hours exposure to 0.1M H_2SO_4 at Al 7075/Ti 15-3 interface. Few pits and corrosion products found.

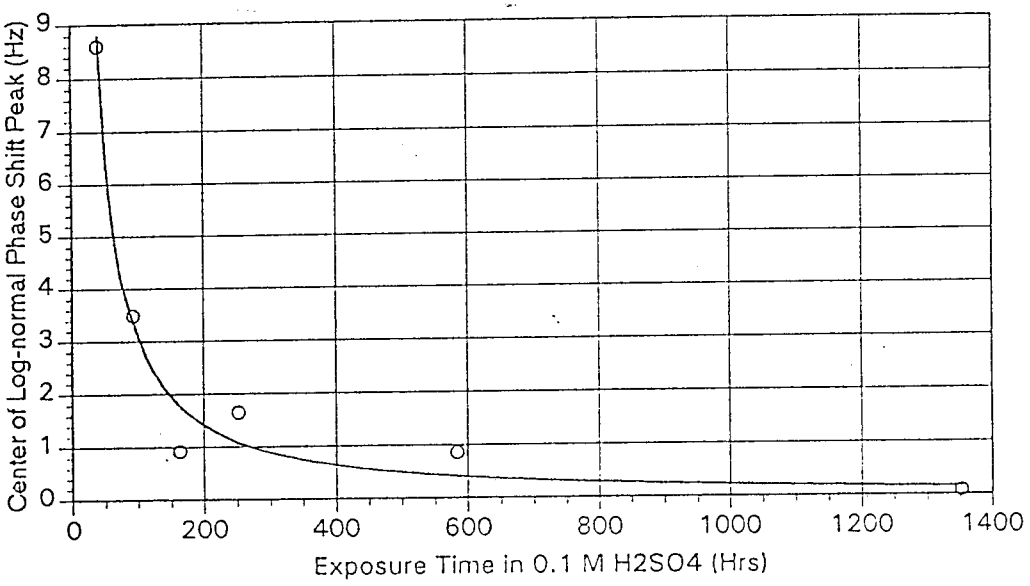

Figure 34. Position change of log-normal peak centroid as a function of exposure time in 0.1M H_2SO_4 for Al 7075/Ti 15-3 coupon. Only data from time intervals after 40 hours included.

A)

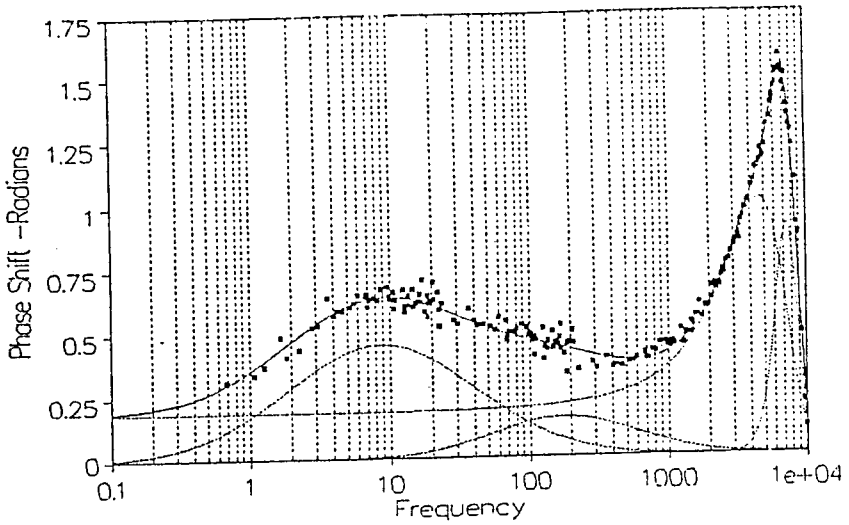

B)

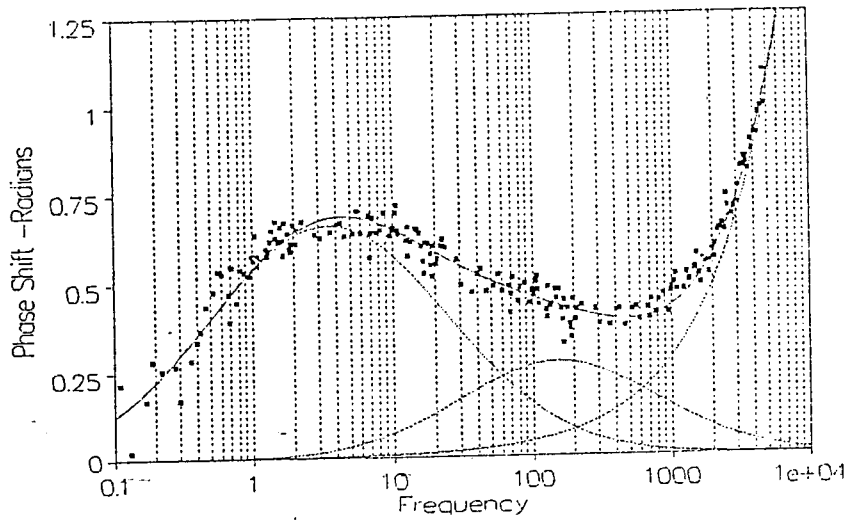

C)

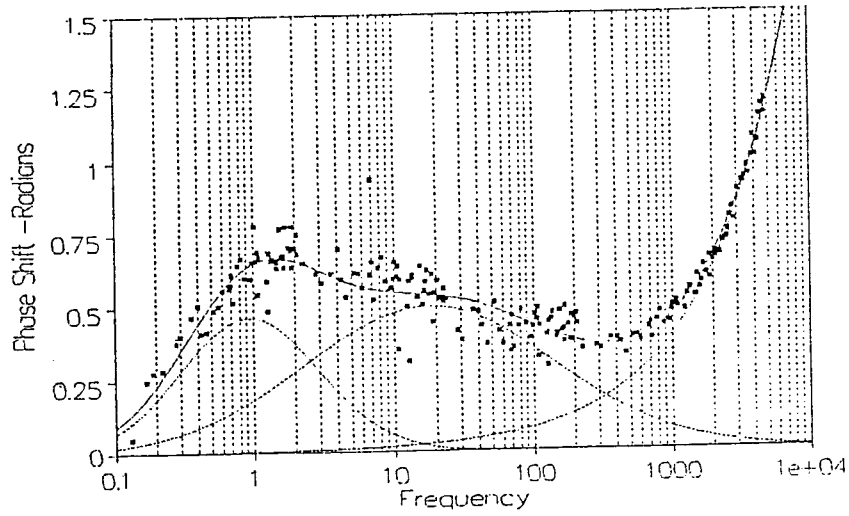

Figure 35 (A, B and C).
FFTEIS measured phase angle dependency on frequency for Al 7075/Al 2024 interface exposed to 0.1M HNO_3 after A) 40.5 hours, B) 93 hours, and C) 164 hours. Best log-normal curves shown over 0.1 to 1000 Hz range.

D)

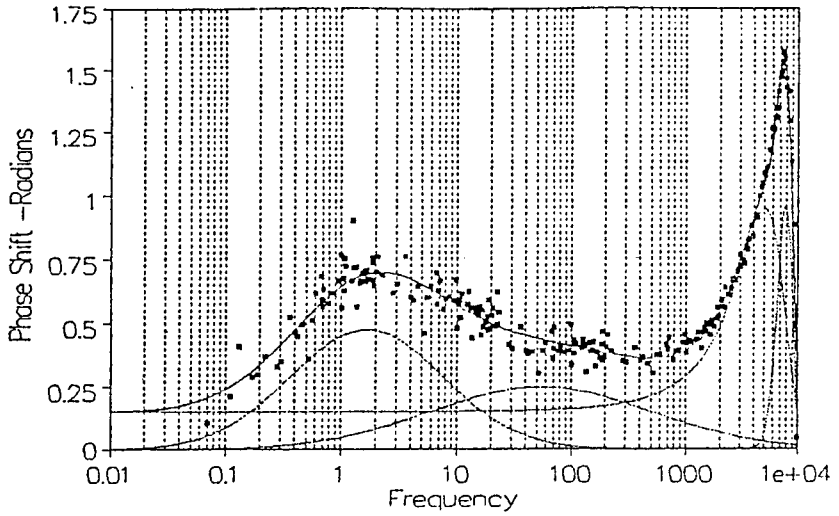

E)

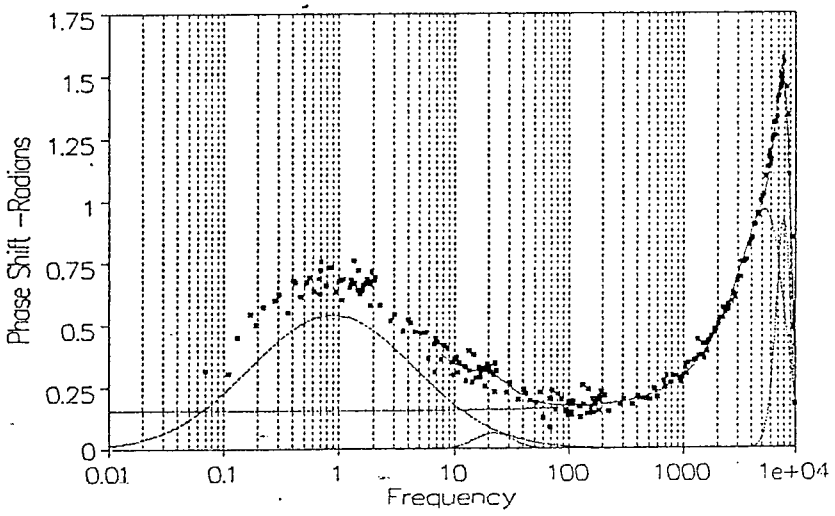

F)

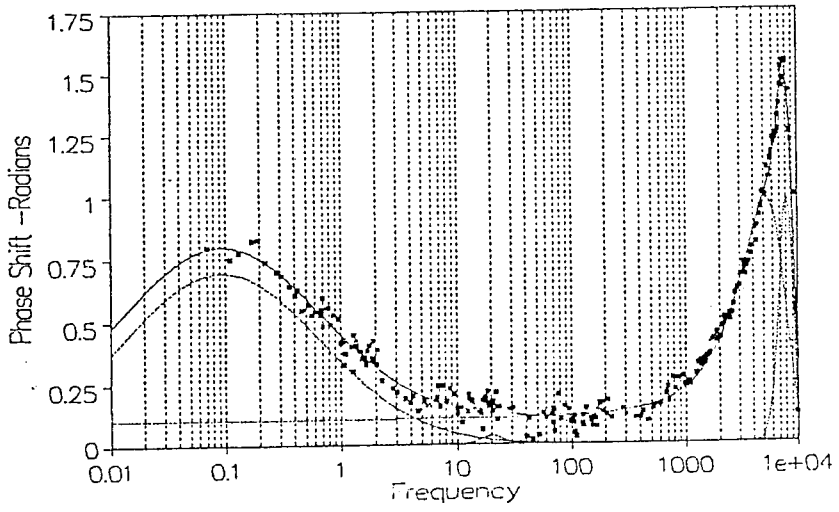

Figure 35 (D, E and F).

FFTEIS measured phase angle dependency on frequency for Al 7075/Ti 15-3 interface exposed to 0.1M HNO_3 after D) 252.5 hours, E) 584 hours, and F) 1353 hours. Best log-normal curves shown over 0.1 to 1000 Hz range.

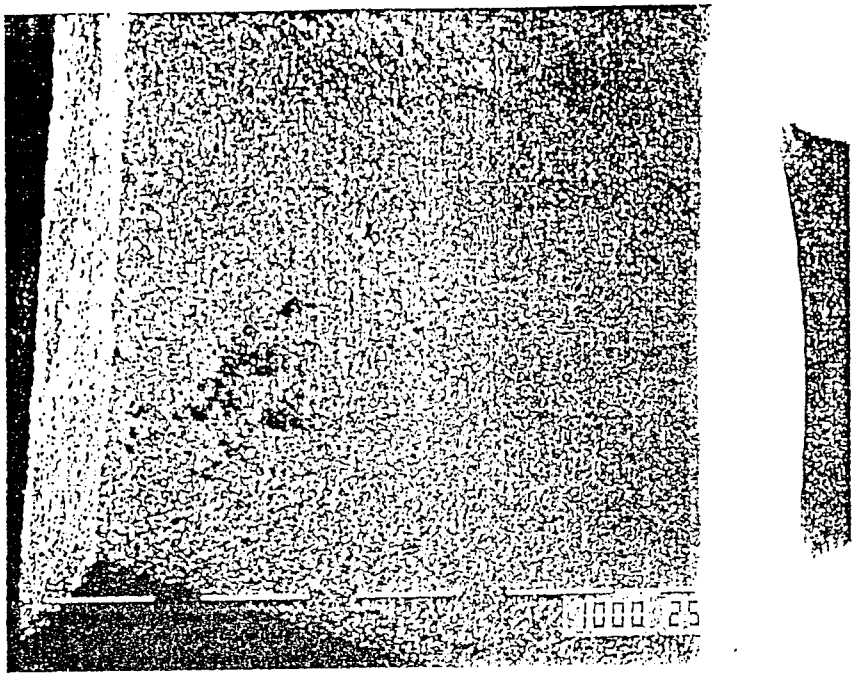

Figure 36. Scanning electron micrograph of Al 2024 coupon after 426.5 hours exposure to 0.1M H_2SO_4 at Al 2024/Ti 15-3 interface. Dark spots are small pits in the interfacial surface. At Figure left, vertical coupon edge will be shown in Figures 38 and 39. Dimension shown = 1000 microns.

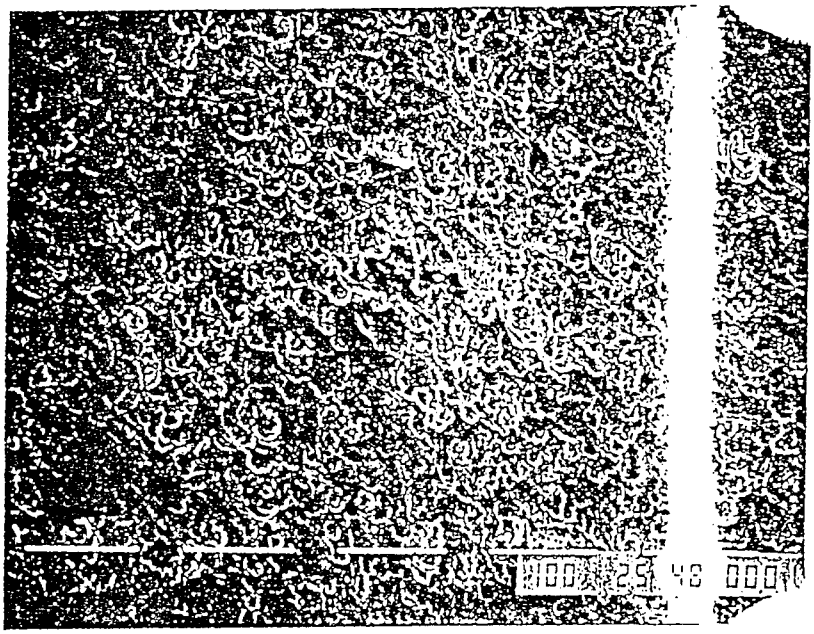

Figure 37. Scanning electron micrograph of Al 2024 coupon after 426.5 hours exposure to 0.1M H_2SO_4 at Al 2024/Ti 15-3 interface. One small pit revealed in Figure 36 is shown enlarged. Dimension shown = 100 microns.

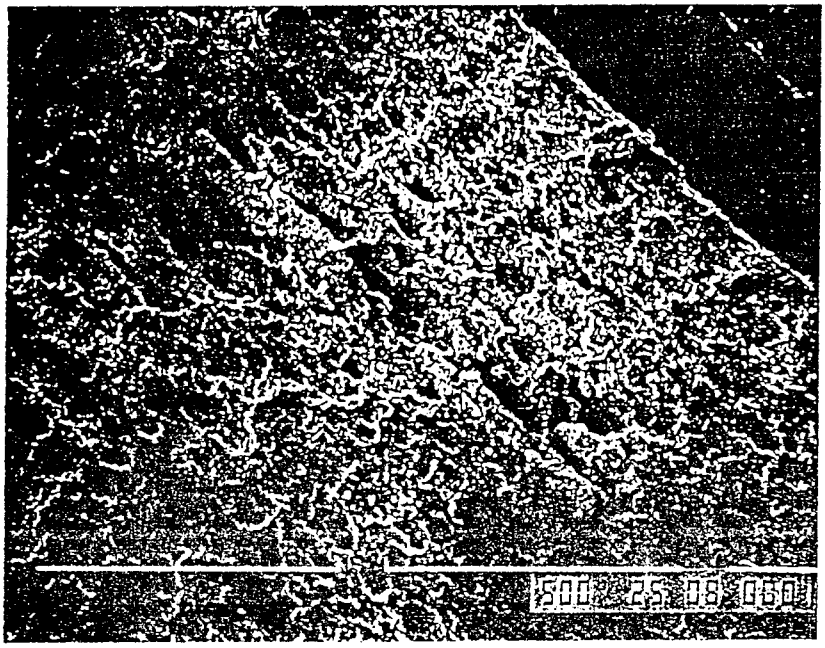

Figure 38. Scanning electron micrograph of Al 2024 coupon after 426.5 hours exposure to 0.1MH_2SO_4 at vertical edge. Pits in original 0.16cm thick coupon edge one revealed. Dimension shown = 500 microns.

Figure 39. Scanning electron micrograph of Al 2024 coupon after 426.5 hours exposure to 0.1M H_2SO_4 at vertical edge. Enlargement of pit revealed in center of Figure 38. Dimension shown = 50 microns.

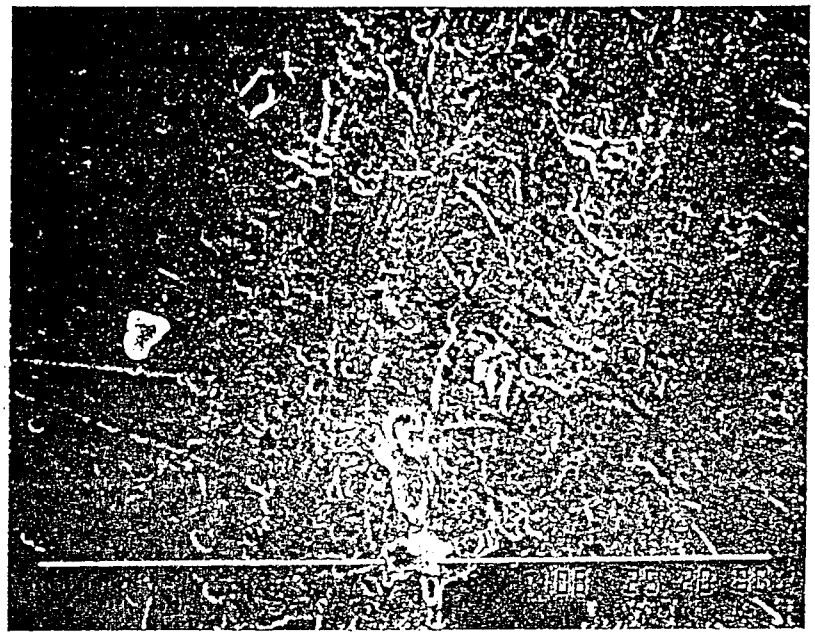

Figure 40. Scanning electron micrograph of Ti 15-3 coupon after 426.5 hours exposure to 0.1M H_2SO_4 at Al 2024/Ti 15-3 interface. Surface roughening located opposite pits shown in Figure 36. Dimension shown = 100 microns.

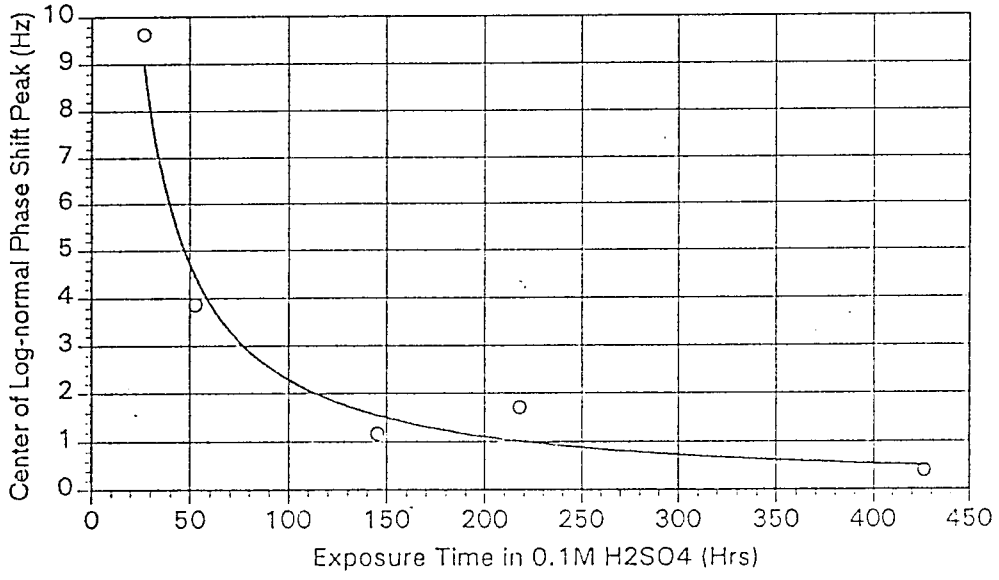

Figure 41. Position change of log-normal peak centroid as a function of exposure time in 0.1 M H_2SO_4 for Al 2024/Ti 15-3 interface.

A)

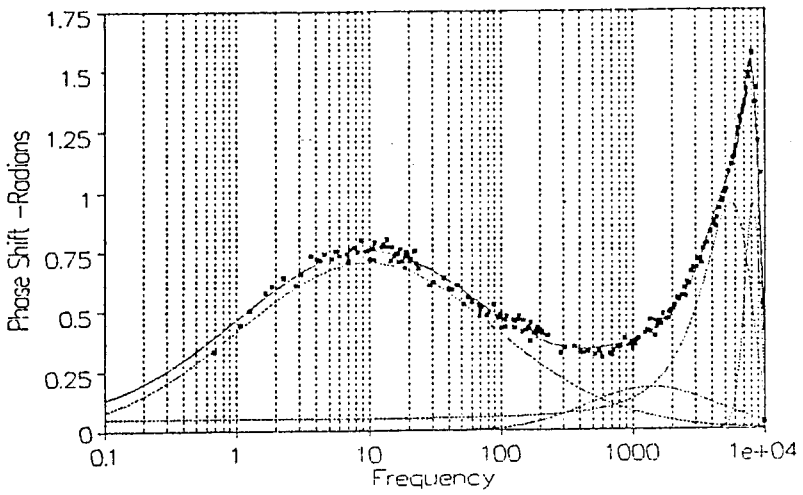

B)

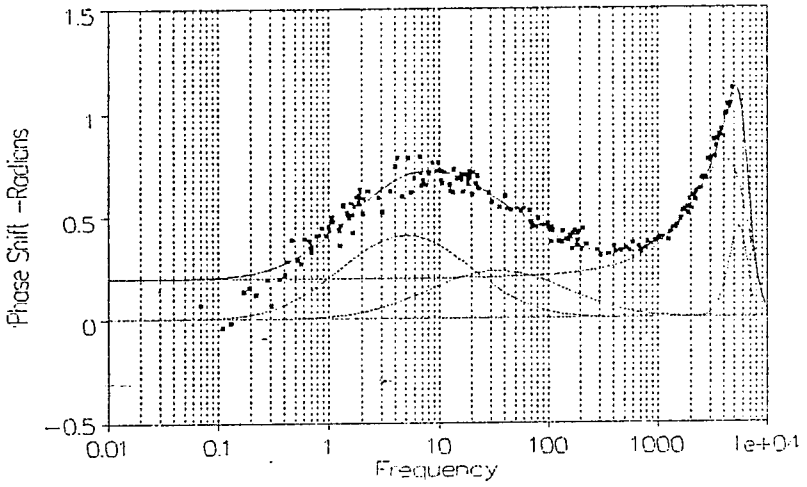

C)

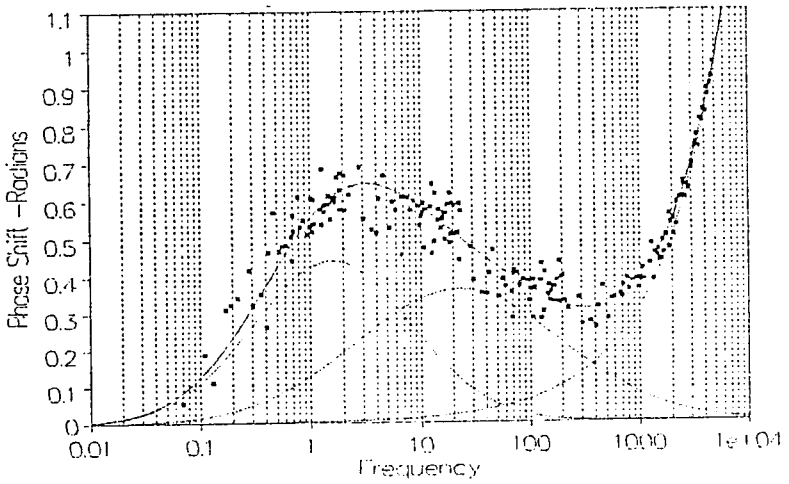

Figure 42 (A, B and C).
FFTEIS measured phase angle dependency on frequency for Al 2024/Ti 15-3 interface exposed to 0.1M HNO_3 after A) 27 hours, B) 53 hours, and C) 145.5 hours.

D)

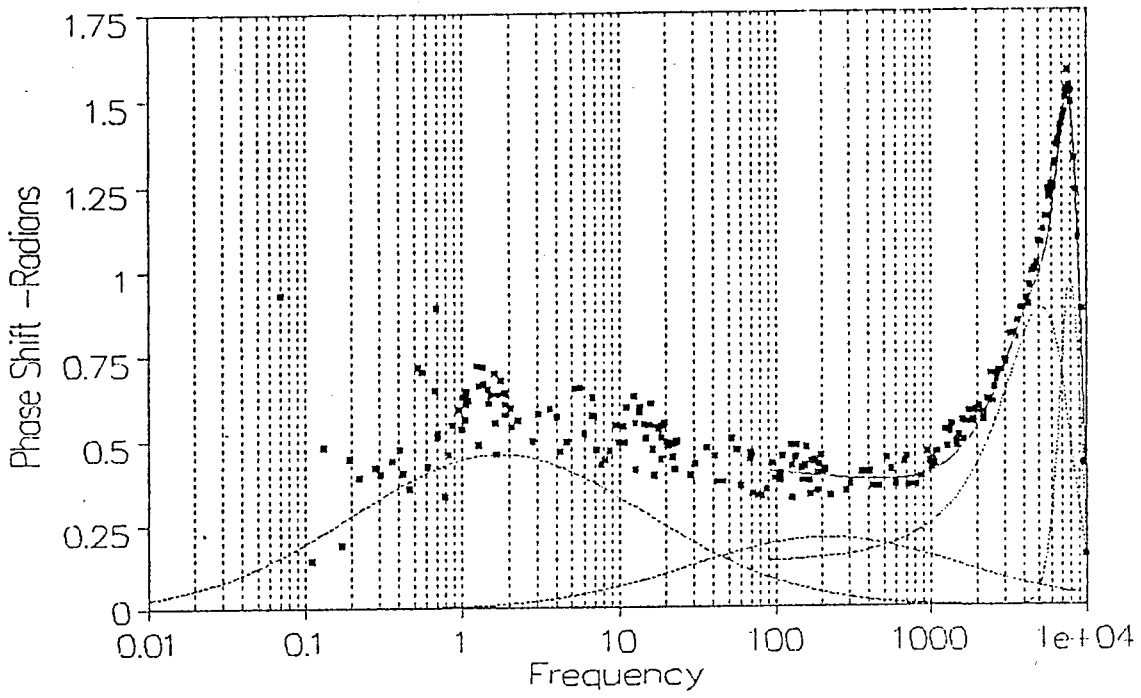

E)

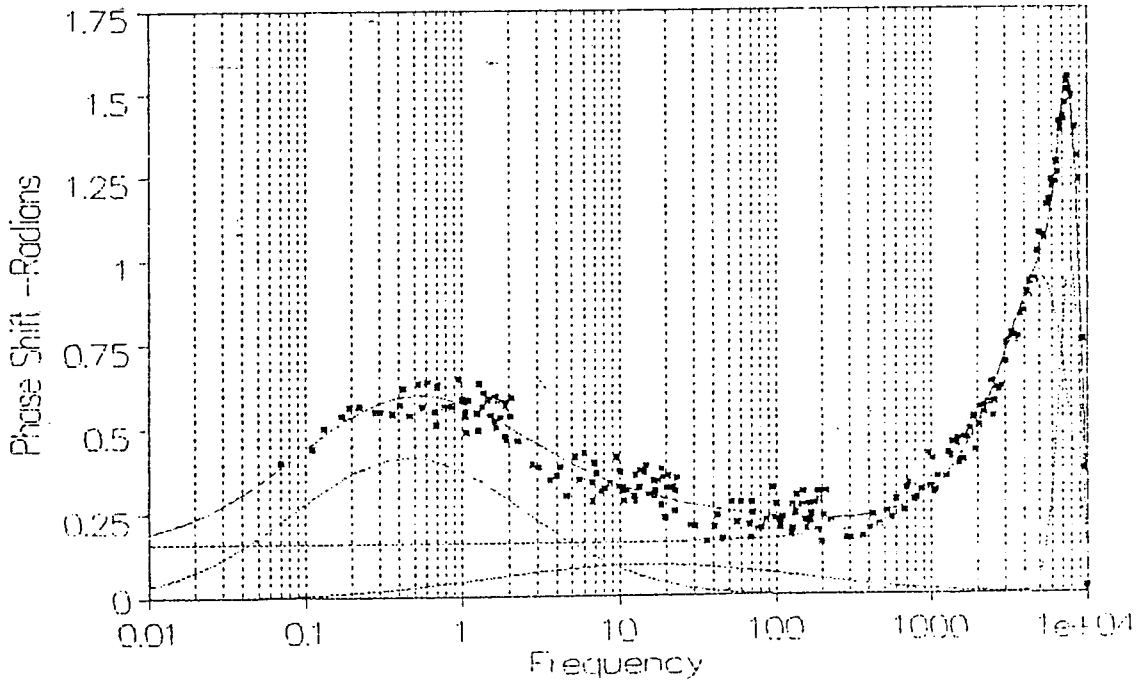

Figure 42 (D and E).
FFTEIS measured phase angle dependency on frequency for Al 20204/Ti 15-3 interface exposed to 0.1M H_2SO_4 after, D) 218 hours and E) 426.5 hours.

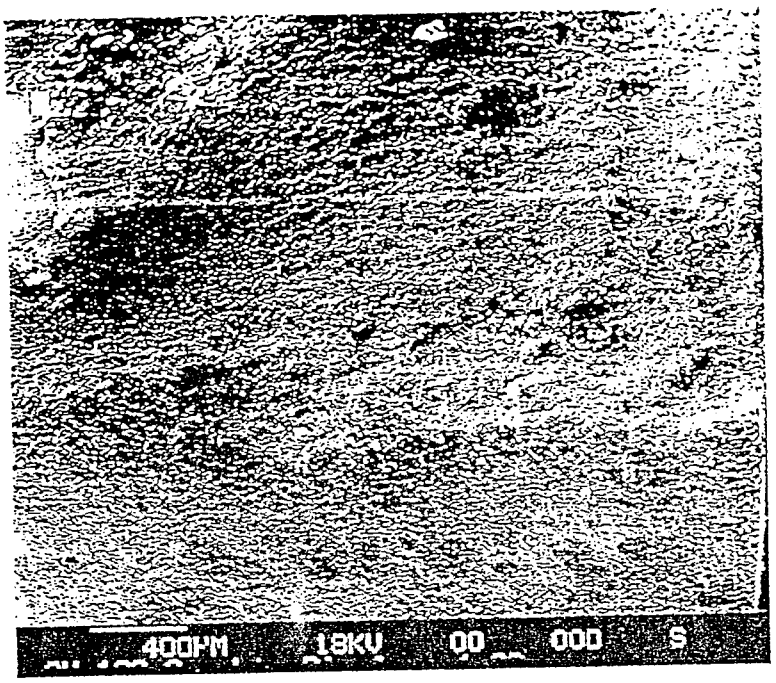

Figure 43. Scanning electron micrograph of Al 2024 coupon after 289.5 hours exposure to 0.1M H_2SO_4 at Ti 15-3/Al 2024 interface. Pits are 1600 microns wide and 300 microns deep. Dimension shown = 400 microns.

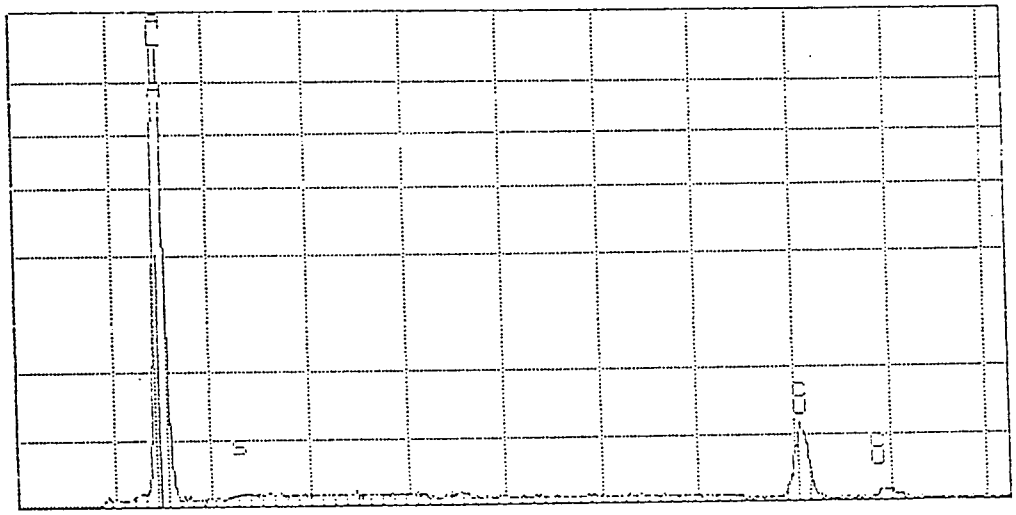

Figure 44. EDX spectrum of Al 2024 coupon composition prior to corrosion solution exposure.

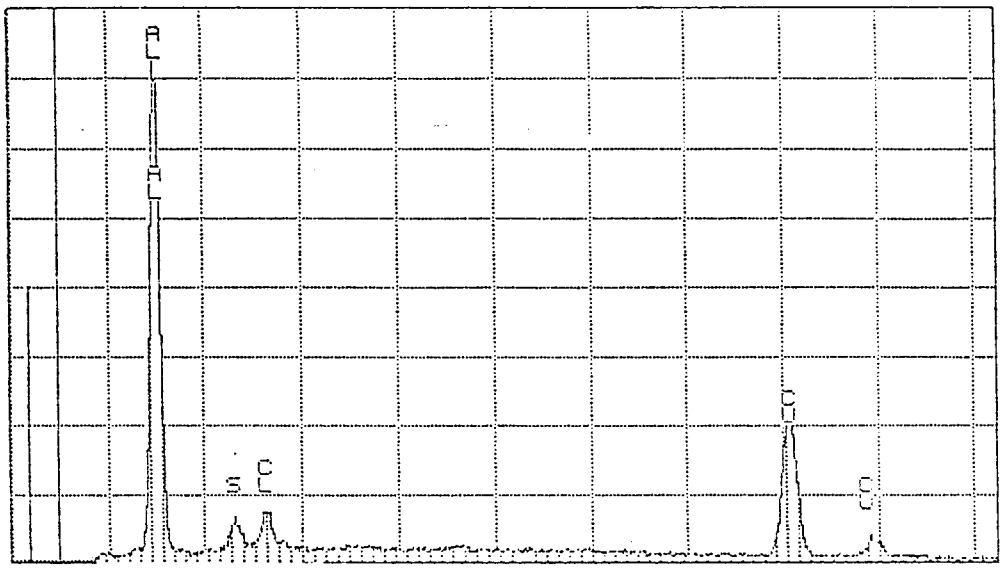

Figure 45. EDX spectrum of Al 2024 coupon composition after 289.5 hours exposure to 0.1M H_2SO_4 at interface corrosion pit shown in Figure 43.

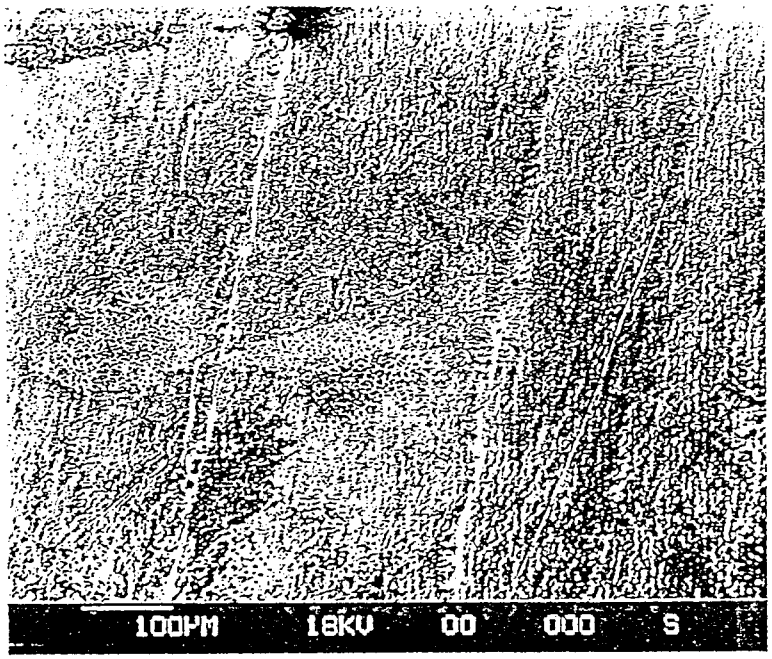

Figure 46. Scanning electron micrograph of Ti 15-3 coupon after 289.5 hours exposure to 0.1M H_2SO_4 at Ti 15-3/Al 2024 interface. Parallel lines of shallow pits are 25 microns wide and 20 microns deep. Dimension shown = 100 microns.

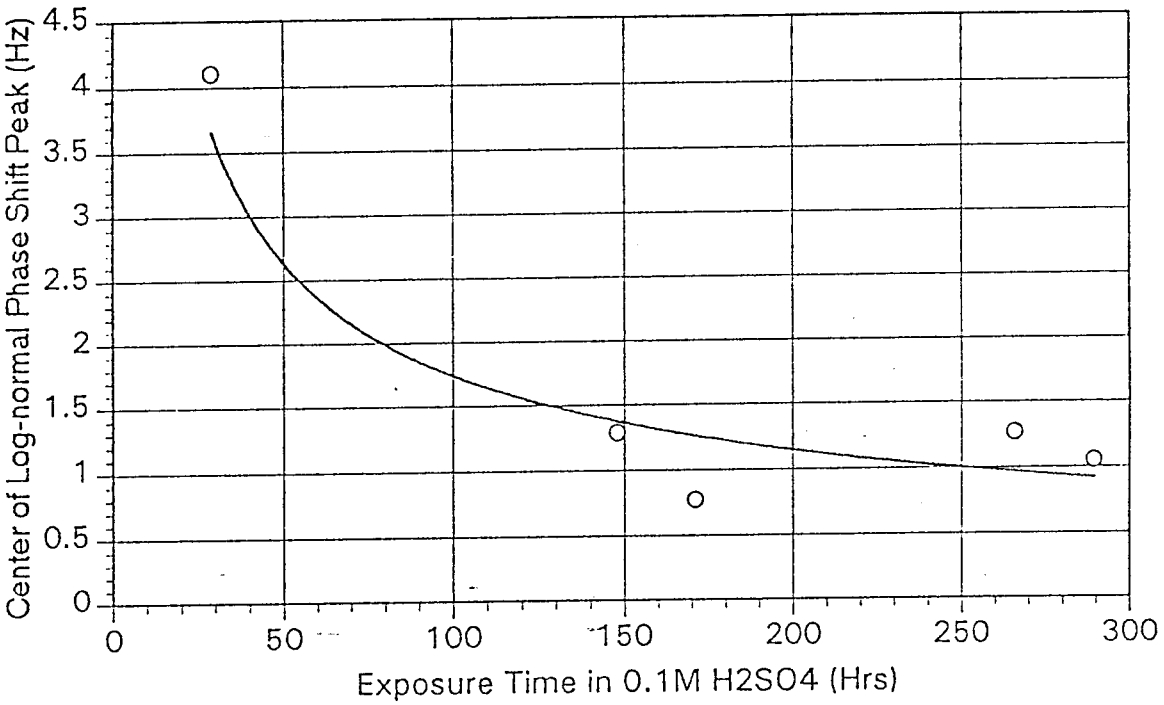

Figure 47. Position change of log-normal peak centroid as a function of exposure time in 0.1M H_2SO_4 for Ti 15-3/Al 2024.

A)

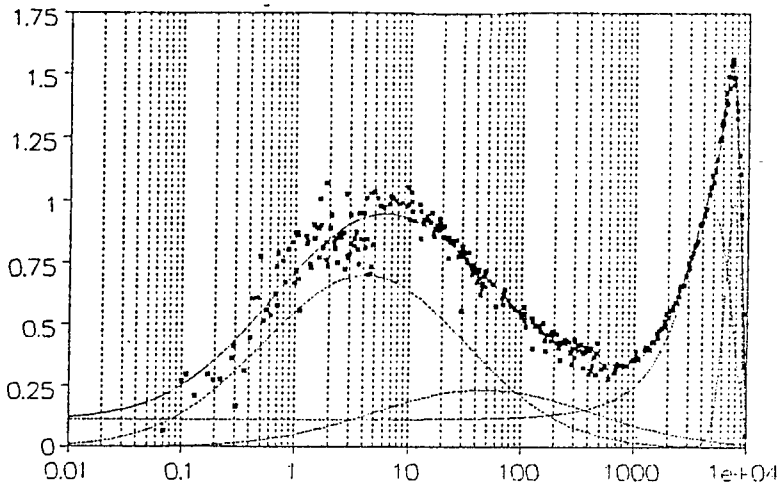

B)

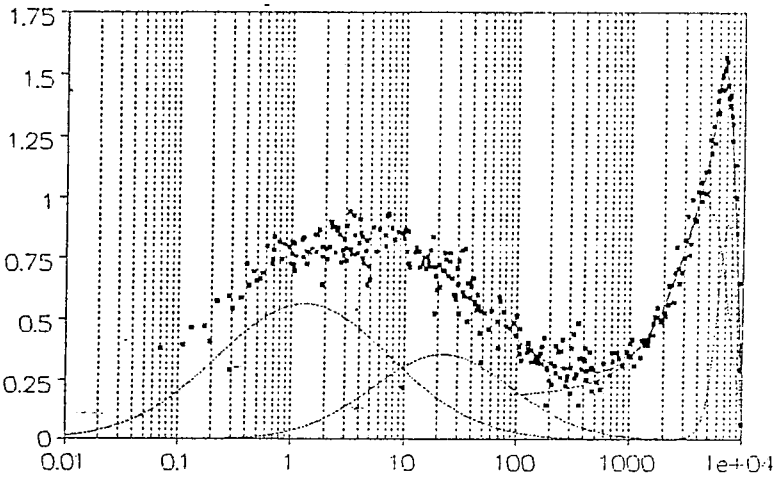

C)

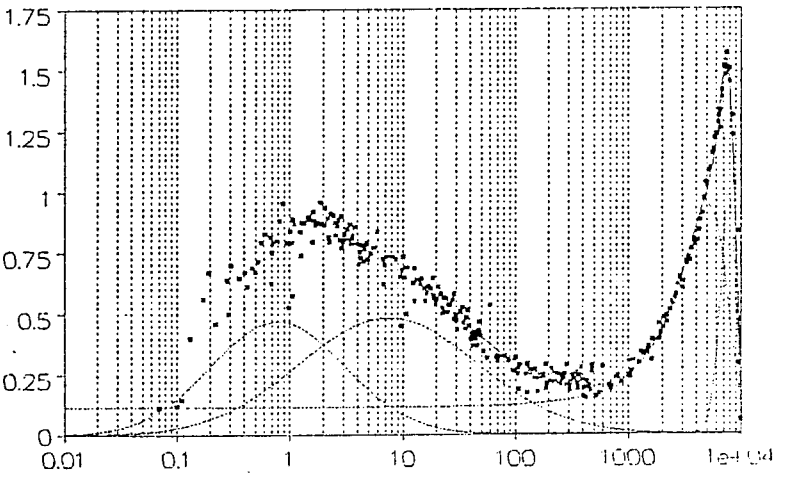

Figure 48 (A, B and C).
FFTEIS measured phase angle dependency on frequency for Ti 15-3/Al 2024 interface exposed to 0.1M HNO_3 after A) 29 hours, B) 148 hours, and C) 171 hours.

A)

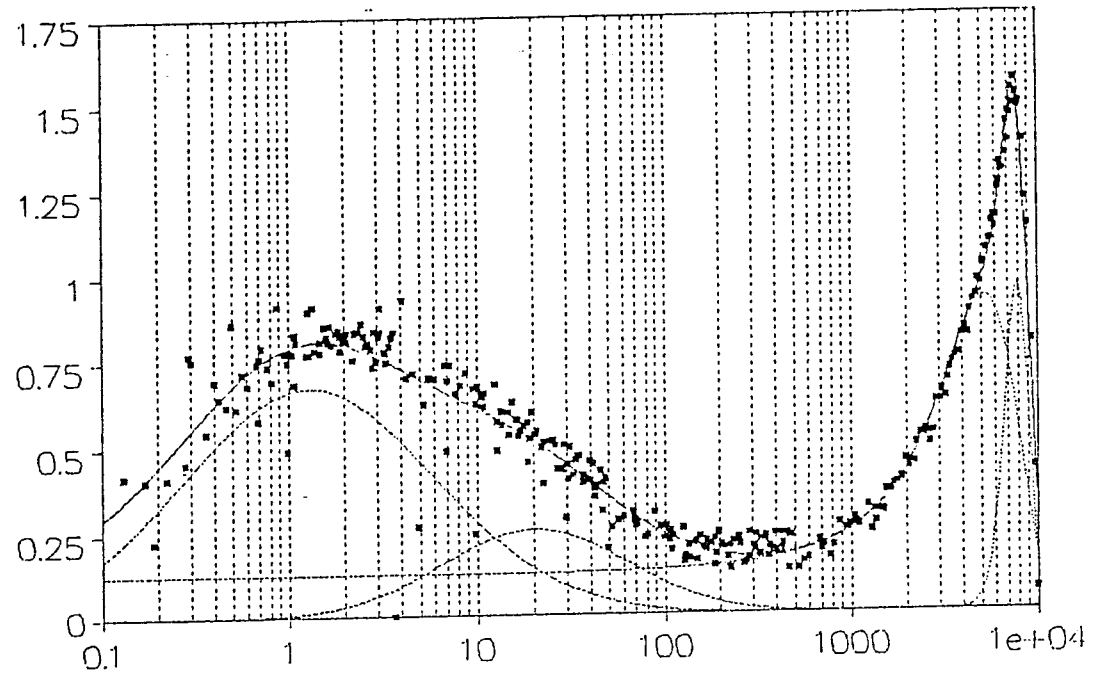

B)

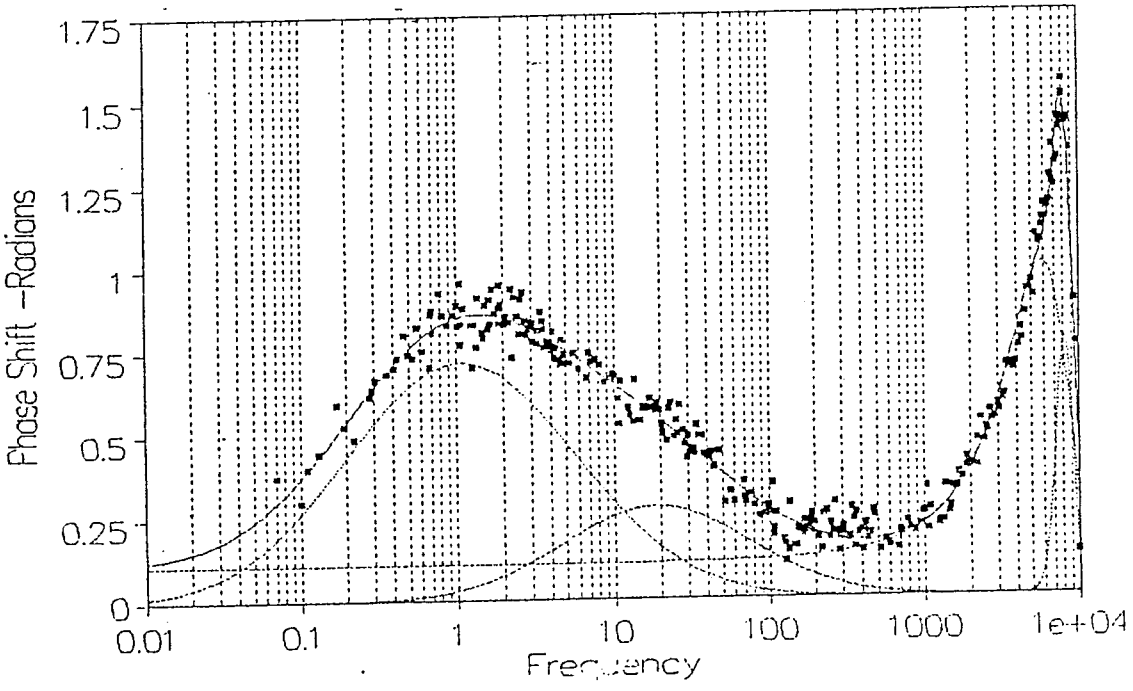

Figure 48 (D and E).

FFTEIS measured phase angle dependency on frequency for Ti 15-3/Al 2024 interface exposed to 0.1M H_2SO_4 after, D) 266 hours and E) 289.5 hours.

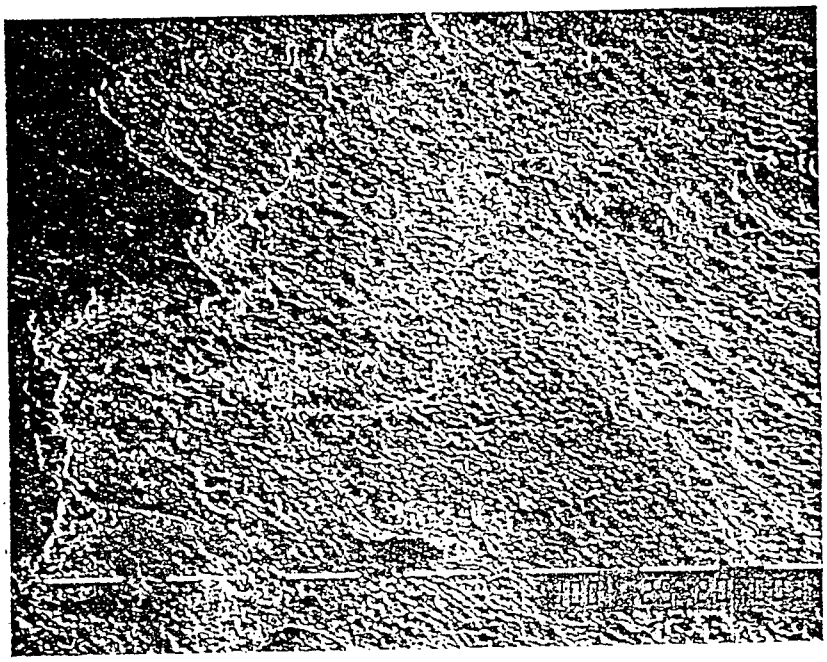

Figure 49. Scanning electron micrograph of Al 7075 coupon after 1412 hours exposure to 0.1M HNO_3 at Ti 15-3/Al 7075 interface. Two crevice corrosion plateaus are revealed with respective heights of 50 and 150 microns. Dimension shown = 100 microns.

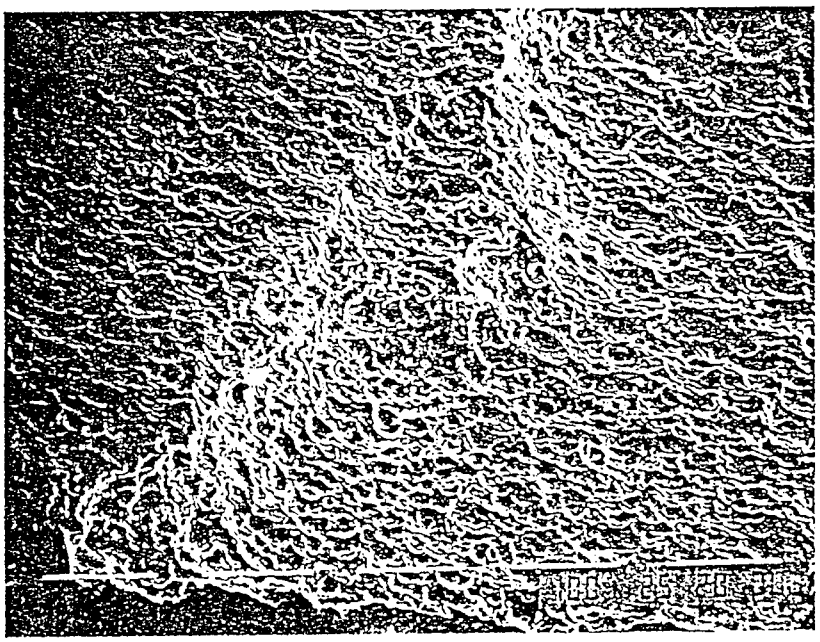

Figure 50. Scanning electron micrograph of Al 7075 coupon after 1412 hours exposure to 0.1M H_2SO_4 at Ti 15-3/Al 7075 interface. Enlargement of plateau shown at right side of Figure 49. Dimension shown = 100 microns.

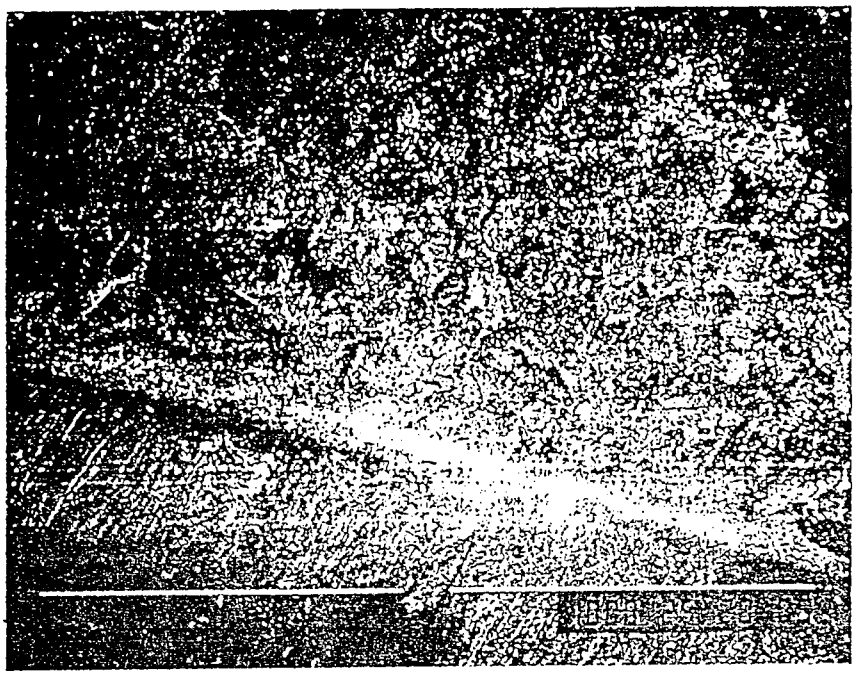

Figure 51. Scanning electron micrograph of Ti 15-3 coupon after 1412 hours exposure to 0.1M HNO_3 at Ti 15-3/Al 7075 interface. Area above diagonal line was inside crevice. Corrosion product is shown as bright. Dimension shown = 1000 microns.

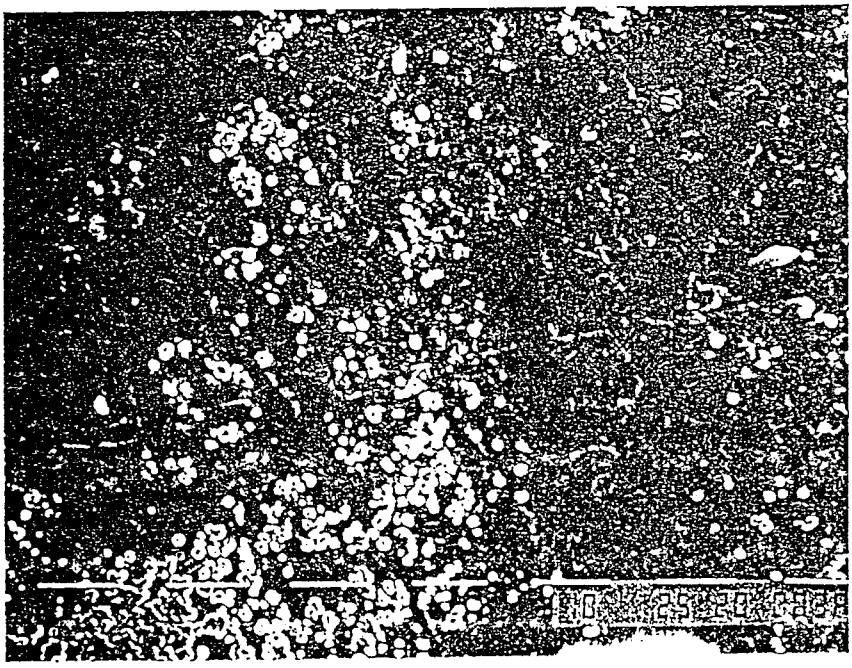

Figure 52. Scanning electron micrograph of Ti 15-3 coupon after 1412 hours exposure to 0.1M H_2SO_4 at Ti 15-3/Al 7075 interface. Texture at lower left is corrosion product elsewhere texture is surface roughening. Dimension shown = 10 microns.

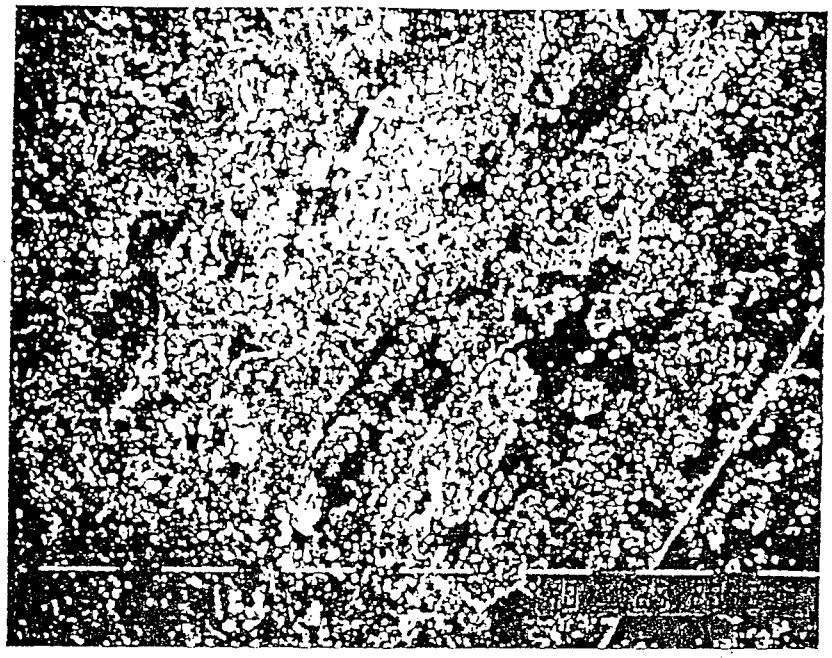

Figure 53. Scanning electron micrograph of Ti 15-3 coupon after 1412 hours exposure to 0.1M HNO_3 at Ti 15-3/Al 7075 interface. Bright material is corrosion product which visually appears copper colored. Dimension shown = 10 microns.

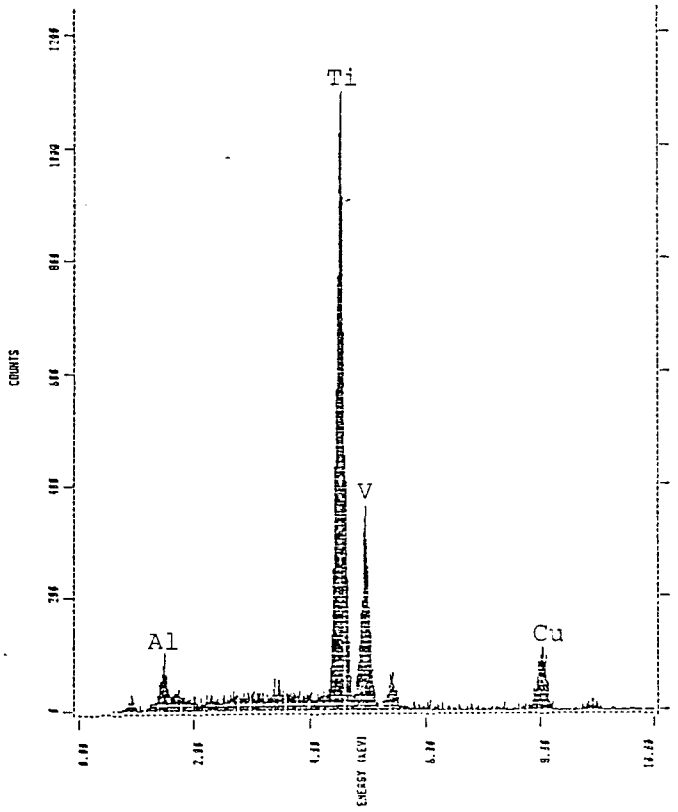

Figure 54. EDX spectrum of corrosion product on Ti 15-3 coupon after 1412 hours exposure to 0.1M HNO_3 at Ti 15-3/Al 7075 interface. SEM of corrosion product shown in Figure 53. Al and Cu peaks appear at 1.5 and 8.0 KeV respectively.

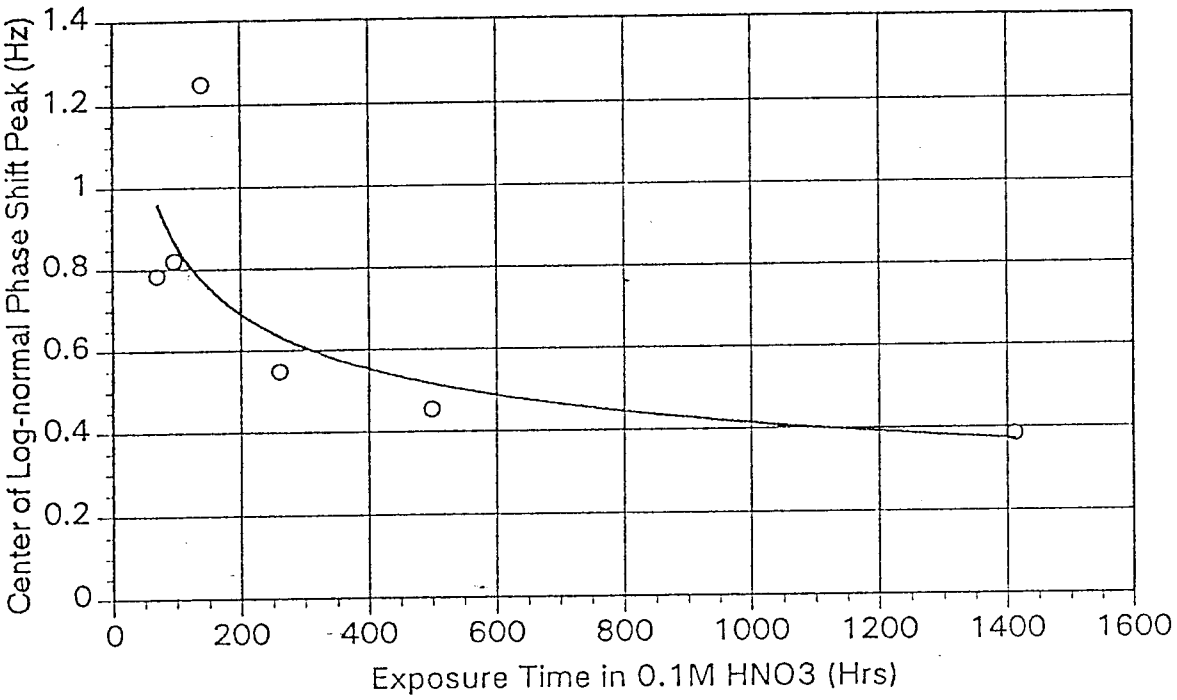

Figure 55. Position change of log-normal peak centroid as a function of exposure time in 0.1M HNO_3 for Ti 15-3/Al 7075 interface.

A)

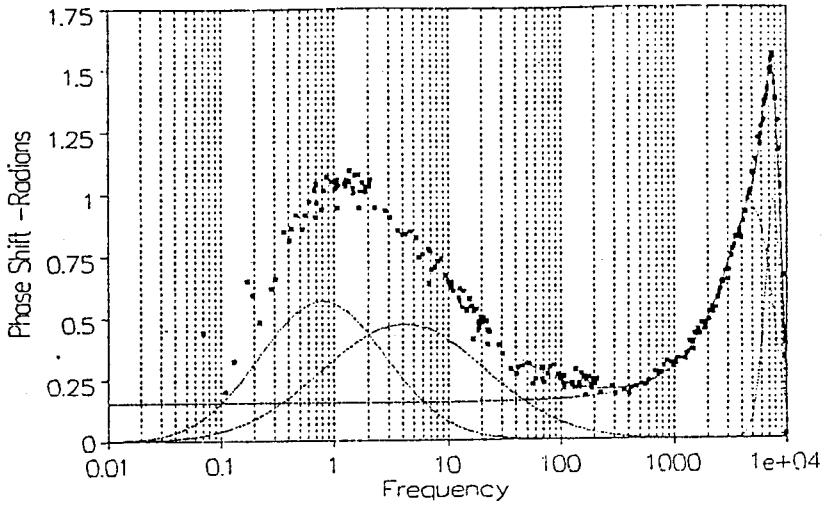

B)

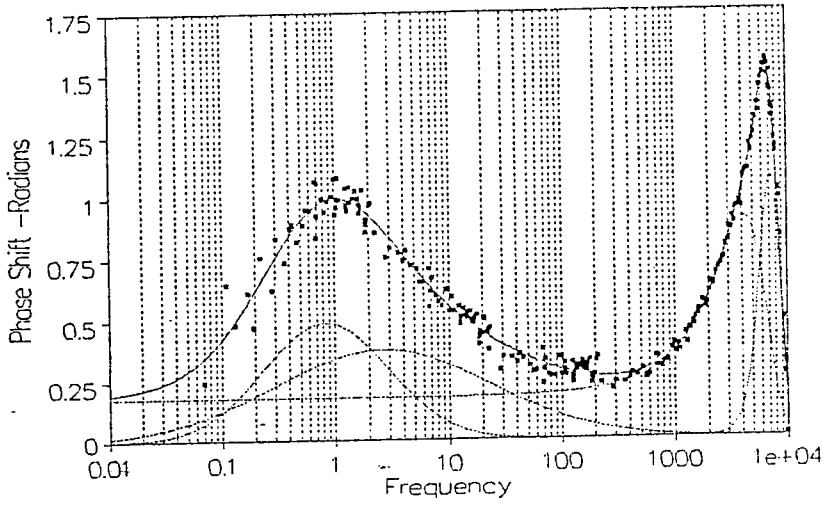

C)

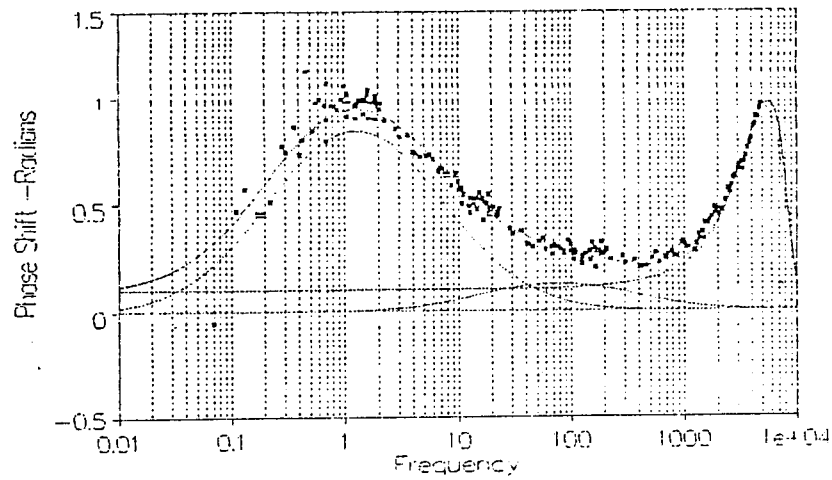

Figure 56 (A, B and C).
FFTEIS measured phase angle dependency on frequency for Ti 15-3/Al 7075 interface exposed to 0.1M HNO_3 after A) 70 hours, B) 97 hours, and C) 140 hours. Best log-normal curves shown over 0.1 to 1000 Hz range.

D)

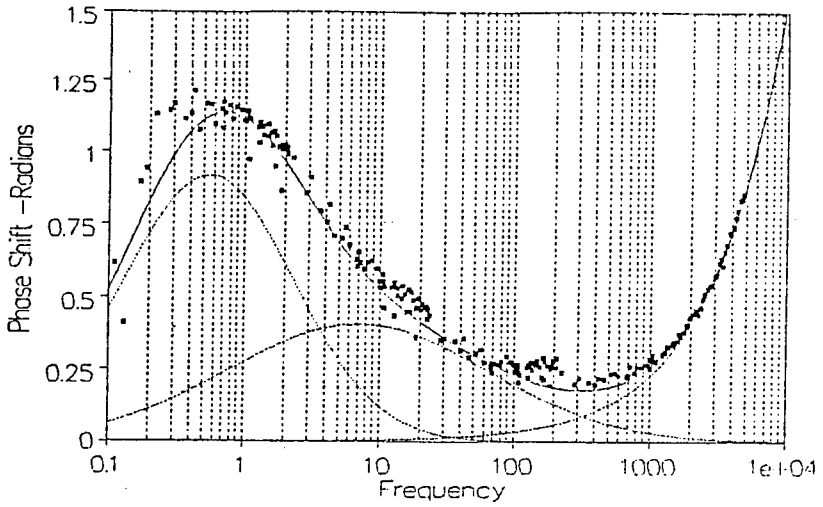

E)

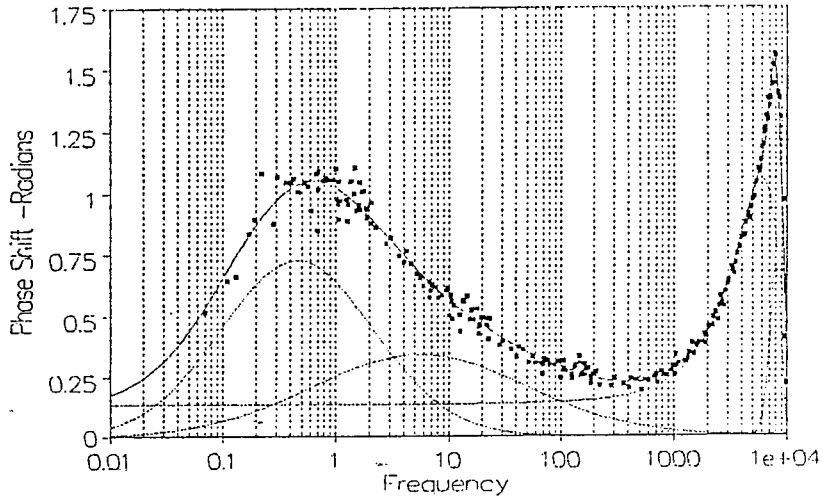

F)

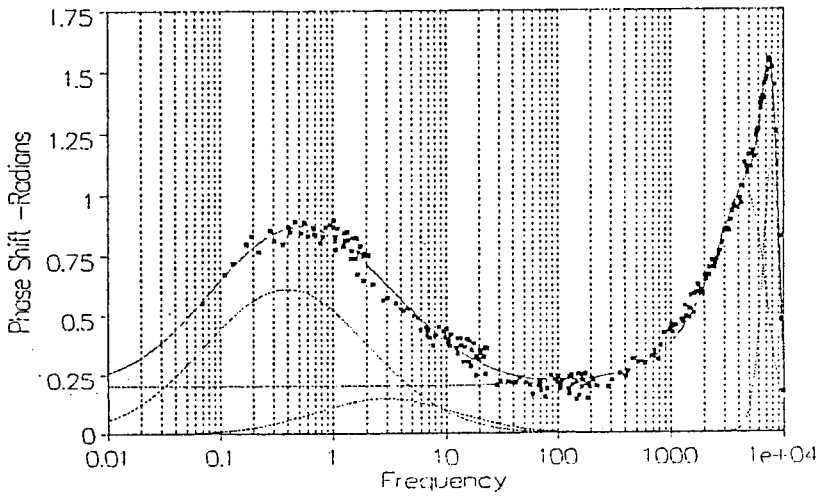

Figure 56 (D, E and F).
FFTEIS measured phase angle dependency on frequency for Ti 15-3/Al 7075 interface exposed to 0.1M HNO_3 after D) 261 hours, E) 500 hours, and F) 1412 hours. Best log-normal curves shown over 0.1 to 1000 Hz range.

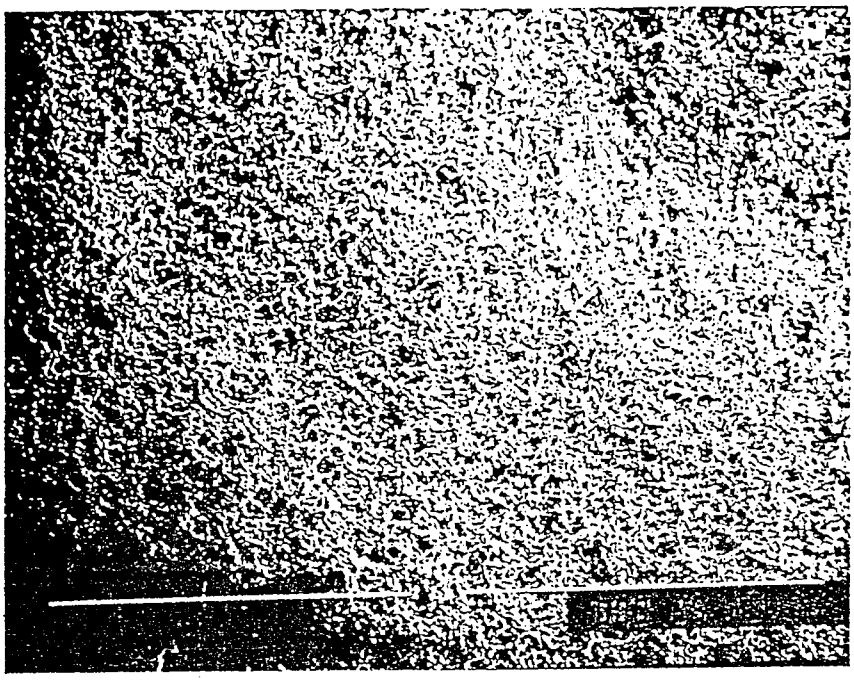

Figure 57. Scanning electron micrograph of Al 2024 coupon after 1358 hours exposure to 0.1M HNO_3 at Ti 15-3/Al 7075 interface. Interfacial pit 6mm wide and 1mm deep. Note surface roughening shown. Dimension shown = 1000 microns.

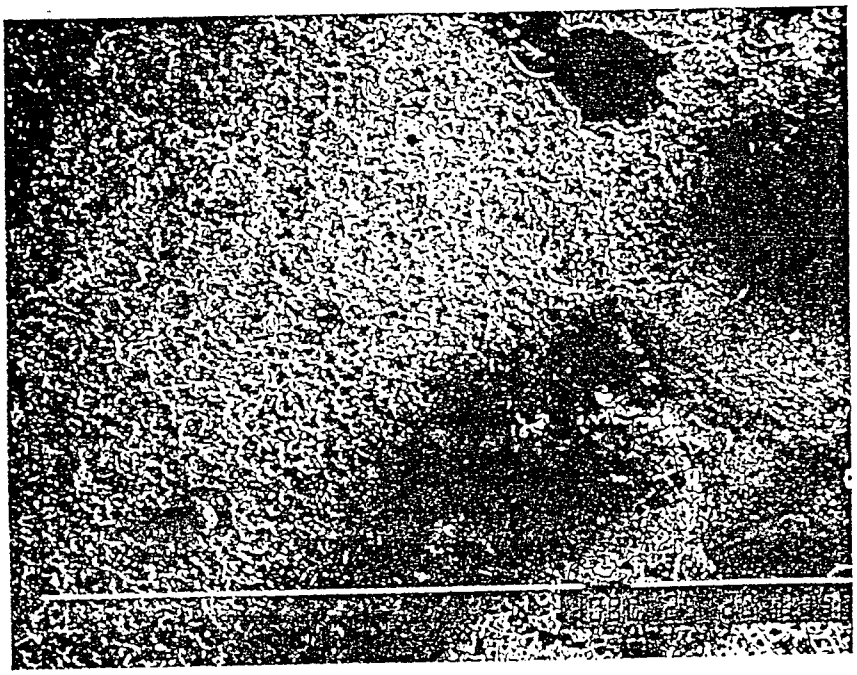

Figure 58. Scanning electron micrograph of Al 2024 coupon after 1358 hours exposure to 0.1M H_2SO_4 at Ti 15-3/Al 7075 interface. Corrosion products are shown in the lower right of wage. Dimension shown = 1000 microns.

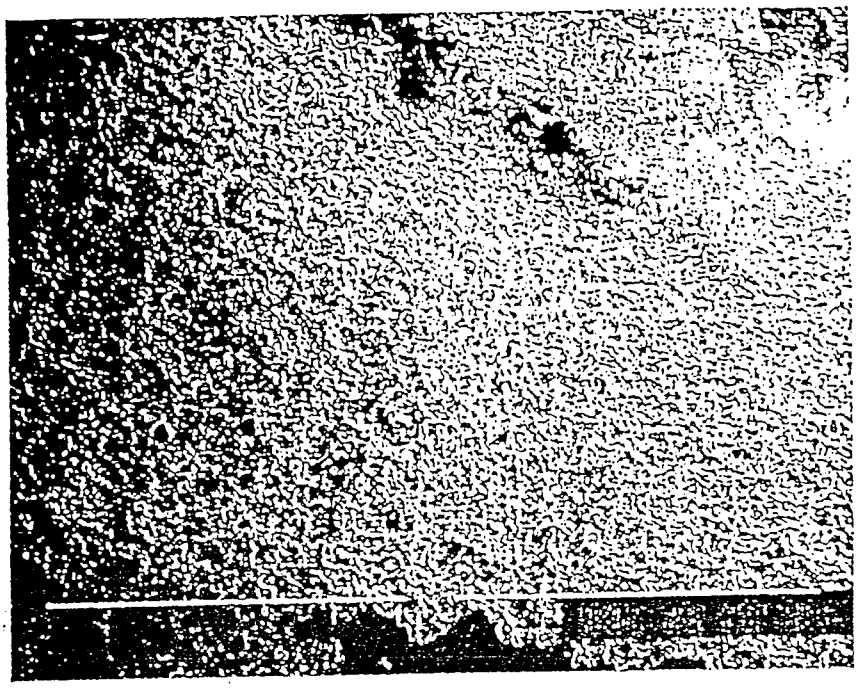

Figure 59. Scanning electron micrograph of Al 2024 coupon after 1358 hours exposure to 0.1M HNO_3 at Ti 15-3/Al 7075 interface. Crevice corrosion plateau shown in upper right of image. Dimension shown = 1000 microns.

Figure 60. Scanning electron micrograph of Ti 15-3 coupon after 1358 hours exposure to 0.1M H_2SO_4 at Ti 15-3/Al 7075 interface. Bright particulate was found to be Al and Cu corrosion product. Dimension shown = 1000 microns.

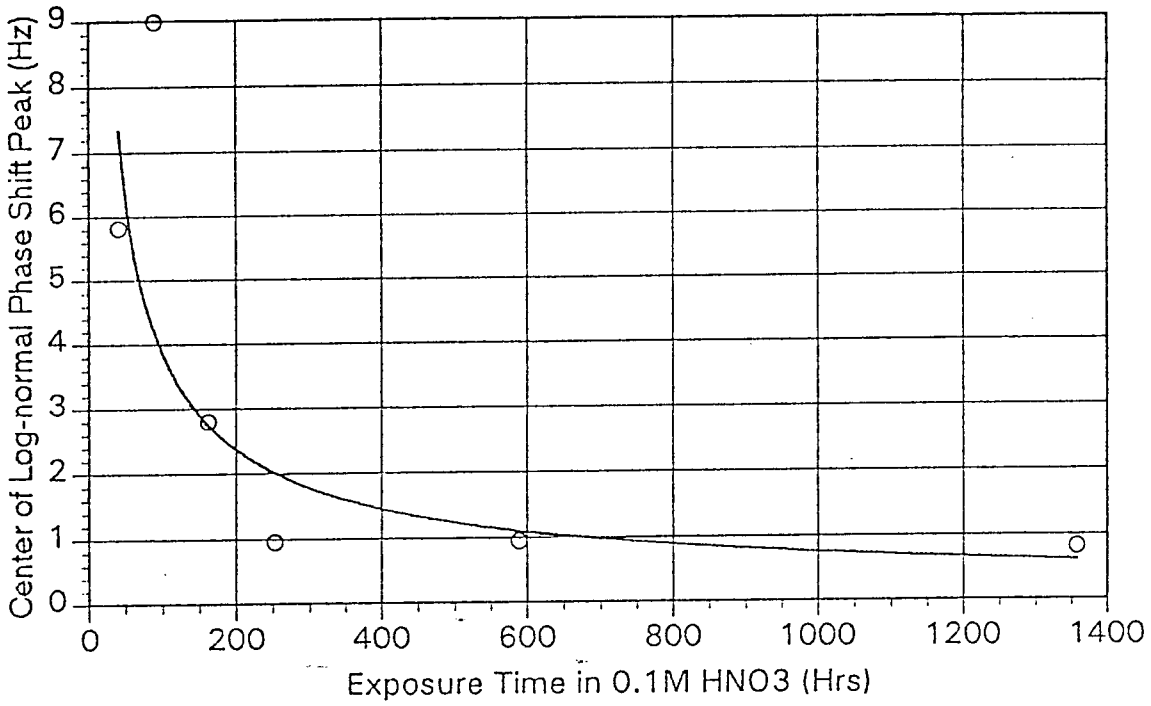

Figure 61. Position change of log-normal peak centroid as a function of exposure time in 0.1 $MHNO_3$ for Ti 15-3/Al 2024 interface.

A)

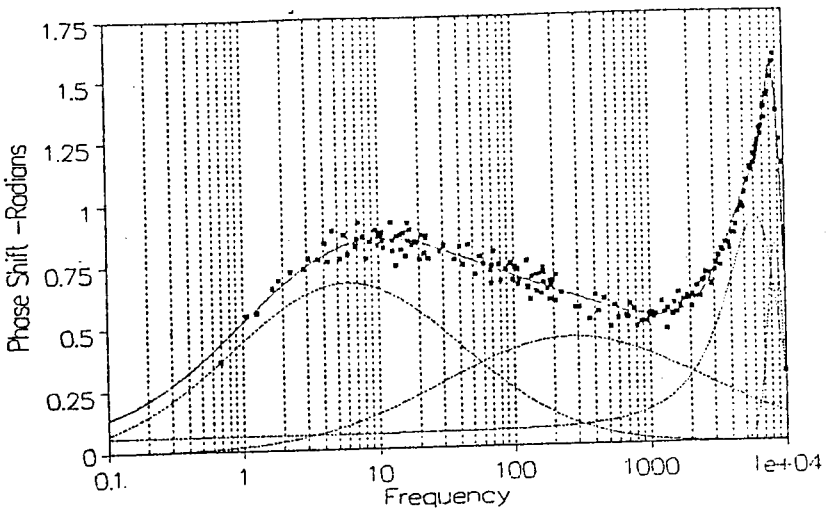

B)

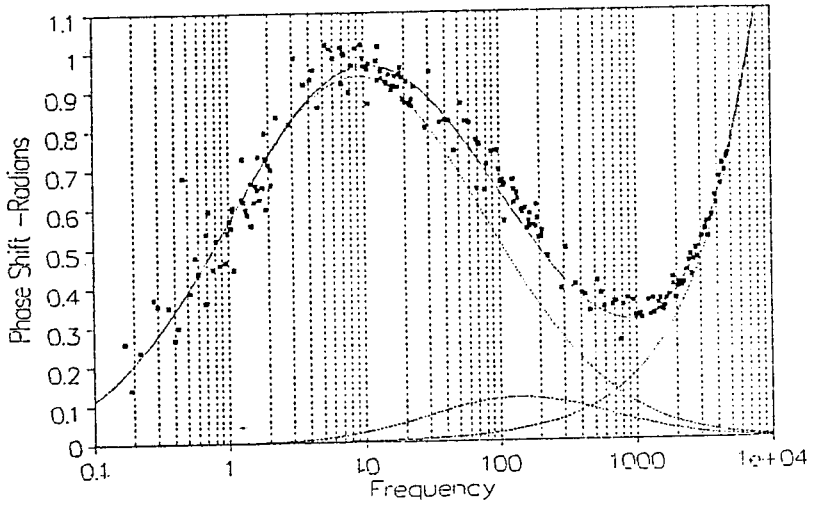

C)

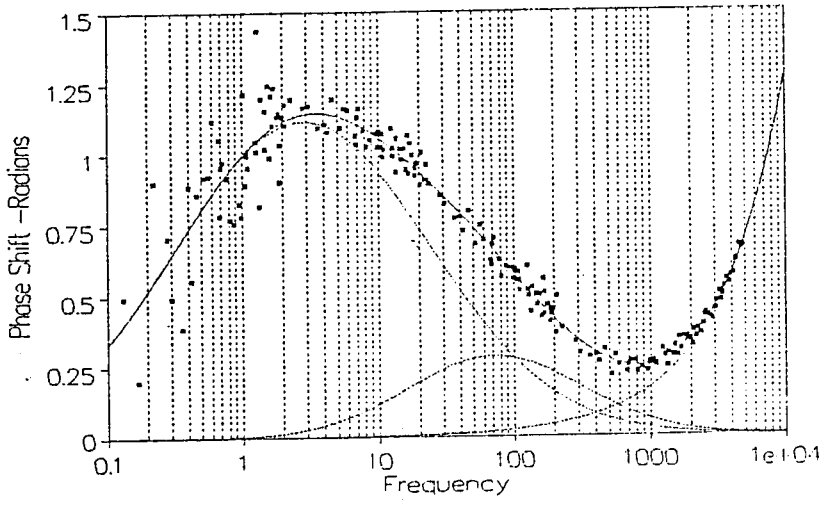

Figure 62 (A, B and C).
FFTEIS measured phase angle dependency of Ti 15-3/Al 7075 interface exposed to 0.1M HNO_3 after A) 40.5 hours, B) 90 hours, and C) 163 hours. Best log-normal curves shown over 0.1 to 1000 Hz range.

D)

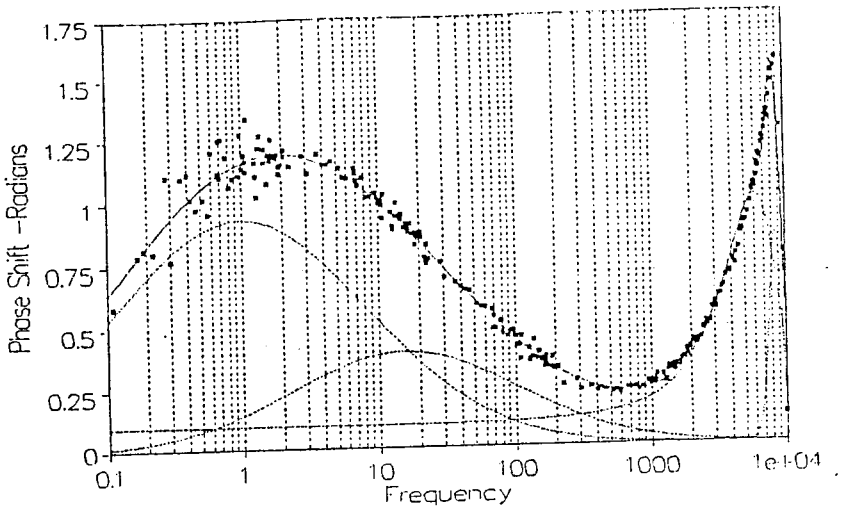

E)

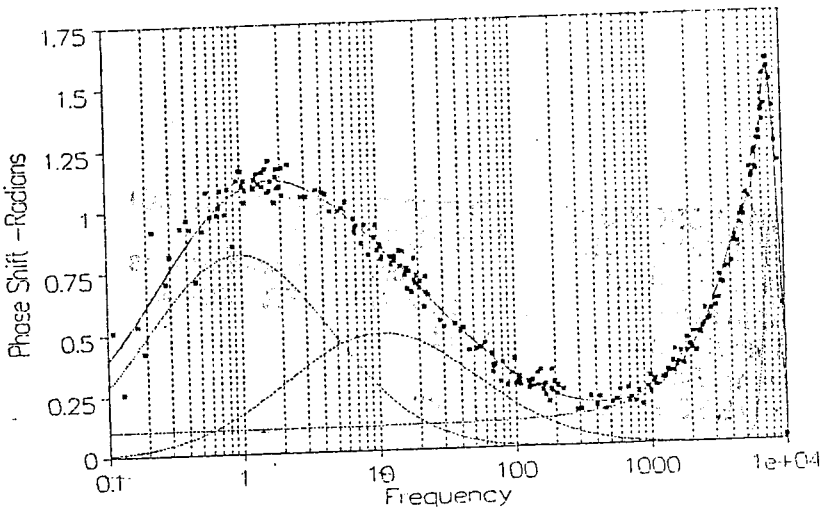

F)

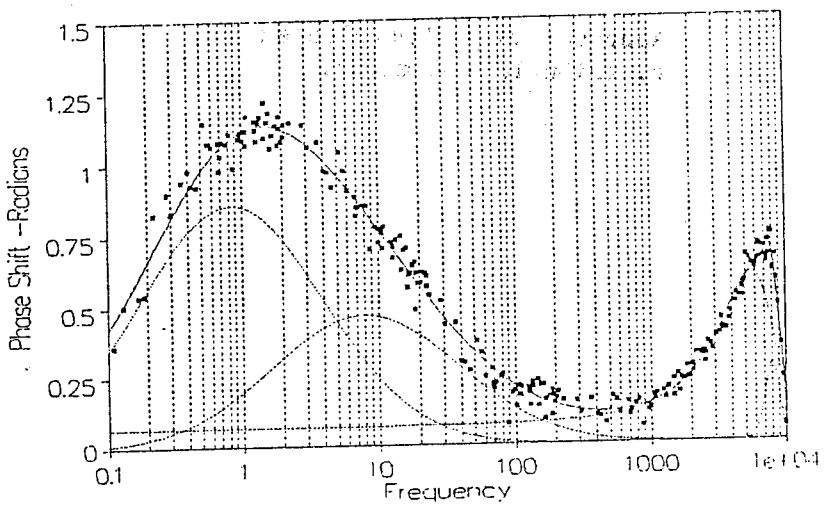

Figure 62 (D, E and F).
FFTEIS measured phase angle dependency of Ti 15-3/Al 7075 interface exposed to 0.1M HNO_3 after D) 253 hours, E) 589.5 hours, and F) 1358 hours. Best log-normal curves shown over 0.1 to 1000 Hz range.